Patient-Specific Metallic Implants for Personalised Medicines

A dissertation submitted to The University of Manchester for the degree of Master of Philosophy in the Faculty of Science and Engineering

2023

By

Rea Johl

10756882

Faculty of Science and Engineering

School of Natural Science,

Department of Materials,

The University of Manchester,

The Sir Henry Royce Institute

Contents

2

Final Word Count: 34005

LIST OF FIGURES

LIST OF TABLES

ABBREVIATIONS

AM - Additive manufacturing

ASTM - American Society for Testing and Materials

BMD - Bone mineral density

CAD - Computer-aided design

CAGR - Compound annual growth rate

CM - Conventional manufacturing

CT - Computed tomography

DED - Directed energy deposition

DXA - Dual-energy X-ray absorptiometry instrument

EBM - Electron beam melting

FAST - Field-assisted sintering technology

FDA - Food and drug administration

FEA - Finite element analysis

HAZ - Heat-affected zone

IEA - International energy agency

ISHKS - Indian Society of Hip and knee surgeries registry

ISO - International Organization for Standardization

L-PBF - Laser powder bed fusion

LCA - Life cycle assessment

LCI - Life cycle inventory

NSAID - Non-steroidal anti-inflammatory drugs

OARSI - Osteoarthritis research society international

SEC - Specific energy consumption

SLM - Selective laser melting

3DP - Three-dimensional printing

THA - Total hip arthroplasty

THR - Total hip replacement

TKA - Total knee replacements

UTS - Ultimate tensile strength

WHO - World health organization

WAAM - Wire arc additive manufacturing

ABSTRACT

The recent innovation in additive manufacturing technologies has made improvements to address personalised medicine. From this perspective, this dissertation discusses the relevance of metal 3D printing (3DP) for customised implant manufacturing, potentially meeting the unmet clinical needs for personalised treatments in developing Asian countries. Additionally, the dissertation includes a relevant review of literature on morphometric analysis based on gender and different ethnicities concerning the biomechanical aspects of the hip bone, and gait pattern essential for implant design. At the peak of the literature review, the environmental impact of metal manufacturing methods for orthopaedic implants is discussed. An effort has been made to identify existing challenges concerning scientific, technological and economic aspects that need to be addressed.

Finite element analysis (FEA) is one of the most versatile methods to scrutinise complex geometries and non-homogeneous material properties for biomechanical modelling. One of the prime advantages of FEA in my thesis is that FEA accommodates structural optimisation of femoral implant design by removing excess material through the incorporation of central hollowness and exercising weight distribution throughout the porous implant design. The impact of two femoral stem designs, solid implant and centrally hollow (internal hollowness), on the stiffness of the bone, is studied by conducting an FEA analysis. This FEA model also studied the critical role of subject weights and bone conditions in the two implant designs. The principal motivation to introduce central hollowness is to check for a reduction in implant stiffness and observe a stress/strain profile closer to natural bone. The results from this study are likely to achieve femoral stem designs for better physiological outcomes and improve the quality of patients undergoing THR. Despite the advanced growth of laser-powder bed fusion in recent years, major challenges include inconsistent part properties and porosity development. For a range of printing parameters that give maximum volumetric energy density, findings for microhardness, texture and anisotropy of 3D printed Ti6Al4V using one of the smallest LPBF printers (by build volume) on the market are revealed.

DECLARATION

No portion of the work referred to in this thesis has been submitted in support of an application for another degree or qualification from this or any other university or institute of learning.

COPYRIGHT STATEMENT

i.   The author of this thesis (including any appendices and/or schedules to this thesis) owns certain copyright or related rights in it (the "Copyright") and they have given the University of Manchester certain rights to use such Copyright, including for administrative purposes.

ii. Copies of this thesis, either in full or in extracts and whether in hard or electronic copy, may be made only in accordance with the Copyright, Designs and Patents Act 1988 (as amended) and regulations issued under it or, where appropriate, in accordance with licensing agreements which the University has from time to time. This page must form part of any such copies made.

iii. The ownership of certain Copyright, patents, designs, trademarks and other intellectual property (the "Intellectual Property") and any reproductions of copyright works in the thesis, for example, graphs and tables ("Reproductions"), which may be described in this thesis, may not be owned by the author and may be owned by third parties. Such Intellectual Property and Reproductions cannot and must not be made available for use without the prior written permission of the owner(s) of the relevant Intellectual Property and/or Reproductions.

iv. Further information on the conditions under which disclosure, publication and commercialisation of this thesis, the Copyright and any Intellectual Property and/or Reproductions described in it may take place is available in the University IP Policy (see http://documents.manchester.ac.uk/DocuInfo.aspx?DocID=24420), in any relevant Thesis restriction declarations deposited in the University Library, the University Library's regulations (see http://www.library.manchester.ac.uk/about/regulations/) and in the University's policy on Presentation of Theses.

ACKNOWLEDGEMENT

PREFACE

The author was previously employed as a Research Aide at the University of Kansas, USA (2018-2019). She was working on synthesizing DNA-based cryo gels for bone regenerative purposes. She has also developed a novel idea of synthesizing 50% more efficient cryo gel having superior mechanical stability, cytocompatibility and porosity with Interpenetrated Polymer Network (IPN). As a crystallization of her research findings, this project was published in ACS Macro Letters (1)

Her qualifications include a Bachelor of Engineering (BE) in Chemical Engineering from India. Also of note is her two years of research experience in nanomedicine and regenerative tissue engineering at Bio-INνENT Lab, Department of Chemical Engineering, India. Working on a project titled, "Nanoparticle-based prophylactic drug delivery to the corneal endothelium", necessitated the understanding of the concepts including drug delivery and the effects of hypothermia and cytokine stresses on the corneal endothelium. This was a challenging project which required thorough comprehension of cell signalling especially involving microtubules and p38 MAPK. The author led a team of three undergraduate students and successfully presented oral and poster presentations in highly competitive conferences/symposiums including NIT Rourkela (SChemCON 2017), Sankara Nethralaya, Chennai (SYNERGY 2018), "Best Paper Award" at IIT Guwahati (REFLUX 2018) after competing with MTech and PhD students from many prestigious IITs of India. As a result of her research findings, the project proposal also received a very competitive student grant of Rs.7500.00 from the Karnataka State Council for Science & Technology, India. The author has landed among the top three in her class with a CGPA of 8.83 on 10.0 (BE in Chemical Engineering).

1. INTRODUCTION

Human diseases and human healthcare systems have stimulated significant research activities in biomaterials science and engineering in the past few decades. Although biomaterials science is a relatively young field, it has significantly impacted human society. The biomedical sector was worth $130 billion last year and is estimated to grow at a high compound annual growth rate (CAGR) of 9.8% (2020-2027) worldwide, emphasising growth in the Asia-Pacific region such as India and China. The Indian orthopaedic and prosthetic device market is currently valued at $8.2 billion, equivalent to INR 58,042 crore and is growing at over 30% per year. The management of osteoarthritis lies in total hip replacement. In recent years, additive manufacturing techniques have risen as a solution to patient-specific implants and address the disadvantages of conventionally manufactured implants for patients across the globe (2).
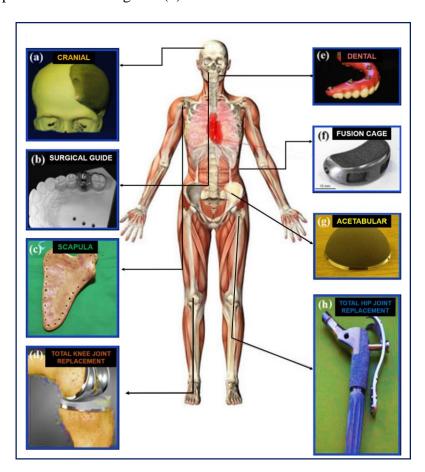
Fig. 1. Schematic illustration of examples of different anatomical parts of the human skeleton where 3D printed implants can be potentially used. In particular, 3D printed implants can be potentially used for a) cranial, b) surgical guide, c) scapula, d) total knee joint replacement, e) dental, f) fusion cage, g) acetabular, h) total hip joint replacement (3).

In the biomedical sector, additive manufacturing is estimated to reach $5.7 billion by 2027 at a CAGR of 29% in India, as per a report by IndustryARC Research (3D Printed Medical Devices Market By Type (Surgical Guides, Surgical Instruments, Prosthetics & Implants, Tissue Engineering Products), By Technology (Photopolymerization, Droplet Deposition (DD) Or Extrusion-Based Technologies, Laser Beam Melting, Electron Beam Melting (EBM), Three Dimensional Printing (3DP) Or Adhesion Bonding), By Geography - Global Opportunity Analysis & Industry Forecast, 2022-2027). A schematic illustration of the wide applications of additive manufacturing in biomedical applications is shown in **Fig. 1**. In the Indian market, almost 80-85% of orthopaedic demands are met through imports (4). The majority of these orthopaedic designs developed for the Western population are different from the anatomy and healthcare priorities of the Indian population. India offers cost-effective care in accredited hospitals with highly skilled doctors, and quality clinical outcomes and annually, over 0.2 million foreigners visit India for medical treatment from other Asian and African countries (as believed by the Federation of Indian Chambers of Commerce and Industry, IMS Health India). Significant demand for patient-specific medical implants therefore exists. Patient specificity enhances osseointegration, thereby increasing the survival rate of the implant.

This dissertation aims to address the unmet clinical needs of total hip arthroplasty (THA) in the Indian context, including the design of hip joints with a patient-specific biomechanical response (finite element analysis, FEA) to improve prosthesis success rates in India. Additive manufacturing (AM) provides the freedom of design concerning patient-specific anatomy attributes with an environmentally conscious processing route and has a shorter design-to-market cycle compared to conventional methods of manufacturing patient-specific metallic implants. Additionally, AM provides superior cytocompatibility due to high surface topography and reduced elastic modulus compared to conventionally manufactured Ti6Al4V, thereby preventing revision surgeries and promoting osseointegration (5–7).

1.1 Research aim and objectives:

a. To study the strain distribution pattern and biomechanical behaviour of two patient-specific femoral implant designs from CT scan data of Indian demography (Finite Element Analysis). To study the effect of stiffness on the bone with the two implant designs. We can define stiffness as the maximum bone strain within the bone strain to failure (25,000 μstrain) values.

    i. To check that there is no plastic yield in the femoral stem for two implant designs, i.e., solid implant and centrally hollow designed implant, by applying forces from the second phase of the walking gait cycle and generating von Mises stress contour under static conditions.

    ii. To study the influence of bone density (bone condition) on both designs implanted within the femur by analysing the maximum principal strain I (ε_1) and minimum principal strain III (ε_3) of the peri-prosthetic bone under static conditions.

    iii. To study the variation of subject weights on both designs implanted within the femur by analysing the maximum principal strain I (ε_1) and minimum principal strain III (ε_3) of the peri-prosthetic bone under static conditions.

b. To characterise SLM printed Ti6Al4V using an environmentally friendly 3d printer (Aconity Mini) in the market, compare its feasibility with other industrial 3d printers (in literature), and understand the anisotropy for 3d printing patient-specific load-bearing implants for orthopaedics. Aconity Mini has the smallest build volume in the 3d printing market and it is cost-effective and environment-friendly.

    i. **Microstructure -** To observe the microstructure of 3D Printed (SLM) Ti6Al4V coupons using Scanning Electron Microscopy (SEM).
    Rationale: Processing methods, processing parameters, and cooling rates determine the material's microstructure.

    ii. **Microhardness -** To investigate the effect of cooling rates on microhardness at different anatomical regions of SLM-printed Ti6Al4V coupons.
    Rationale: Different cooling rates affect the grain size, which therefore induces differences in the hardness of the material.

    iii. **Compression Properties -** To determine the effect of anisotropy (i.e., different build directions) on compression testing.
    Rationale: Microstructural anisotropy originates from the layer-by-layer based fabrication in the AM process, which introduces a unique thermal history at each

location within the part as each subsequent laser scan reheats the material. A relation between the anisotropic microstructure and compressive properties needs to be understood.

iv. **Texture Analysis –** to understand the effect of process parameters on the texture of 3d printed Ti6Al4V.

Rationale: Process parameters affect the solidification of the β grains, the β → α transformation and the texture evolution that occurs at each layer deposition. The crystallographic texture of 3d printed parts significantly influences the mechanical properties.

This dissertation discusses the relevance of metal 3D printing (3DP) for customised implant manufacturing, potentially meeting the unmet clinical needs for personalised treatments in developing Asian countries. Additionally, the dissertation includes a relevant review of literature on morphometric analysis based on gender and different ethnicities concerning the biomechanical aspects of the hip bone, and gait pattern essential for implant design. At the peak of the literature review, the environmental impact of metal manufacturing methods for orthopaedic implants is discussed. An effort has been made to identify existing challenges concerning scientific, technological and economic aspects that need to be addressed.

The impact of two femoral stem designs, solid implant and centrally hollow (internal hollowness), on the stiffness of the bone, is studied by conducting a Finite Element Analysis (FEA). The results from this study are likely to achieve femoral stem designs for better physiological outcomes and improve the quality of patients undergoing Total Hip Arthroplasty. For a range of printing parameters that give maximum volumetric energy density, the effect of anisotropy on microstructure, microhardness, and texture of 3D printed Ti6Al4V using one of the smallest LPBF printers (by build volume) in the market is studied.

2. LITERATURE REVIEW
2.1 Physiology of human bone

The musculoskeletal system collectively works towards co-coordinating body movement and providing structural stability (8). It is broadly categorised into the muscular system and skeletal systems. The musculoskeletal system comprises bones, ligaments, muscles, tendons, cartilage, joints and connective tissues (9).

The bones of the musculoskeletal system articulate to form joints. Based on their functionality, joints are classified into synarthrosis, amphiarthrosis and diarthrosis. Diarthrosis (synovial) or freely moveable joints are the main operational joints of the body.

Depending on the type of movement allowed, synovial joints are sub-classified into hinge joints, saddle joints, planar joints, pivot joints, condyloid joints, and ball and socket joints (10).

The hip joint is a true example of a ball and socket joint, an intricate anatomical structure that transmits forces from the ground up and from the head, neck, and trunk (11,12). At the hip joint, the ultimate contact forces are nearly thrice the body weight while walking and greater than seven times the body weight while stair-climbing (12–14). The hip joint withstands many exertion forces of the body daily, possibly the reason for being the second most commonly affected joint by osteoarthritis (12).

The bony configuration of the hip, well-built capsular-ligamentous structure, and strong muscles surrounding the hip joint provide support and stability to the hip. The hip joint withstands and transfers body weight during routine activities, sometimes more than body weight, such as running and stumbling. Such strenuous activities involve the tibiofemoral joint. These joints often develop musculoskeletal disorders. Hence, it is essential to understand the morbidity of the associated diseases and the principles of managing hip disorders (12,15).

2.1.1 Structure of the bone

Before mentioning more about the musculoskeletal system, it is essential to mention the bone's material-based constitution. It is relevant as the focus of this thesis lies in developing patient-specific implants based on synthetic biomaterials. Organic components and inorganic mineral crystals together form the natural bone (the main component of the skeletal system). Bone is a biomaterial whose organic substrate comprises type-I collagen (40% by volume), type-III and type-IV (collagen, fibrillin). In comparison, non-stoichiometric calcium hydroxyapatite (45% by volume) makes up for the inorganic component of the bone. The residual (15%) aqueous volume is either held up in the lacunocanalicular space region or is captured by collagen (16–18). Type-I collagen is the principal organic constituent of the bone. It has dimensions of 1.5 nm in diameter, and 300 nm in length, forming a triple helix. Other non-collagenous components are glycoproteins and proteoglycans (16,17,19). Hydroxyapatite, HA, is shaped as a plate measuring 50×25 nm in size ranging from 1.5nm to 4nm in thickness (20). Together, collagen molecules and HA crystals provide the strength, flexibility and toughness required for the functioning of the bone.

Fig. 2 shows the hierarchical structure of the bone, wherein each level of the hierarchy performs mechanical, chemical and biological functions. The hierarchical levels include

macroscale, microscale, sub-microscale, nanoscale and sub-nanoscale. The bone can further be classified as cortical bone and cancellous bone. The building block of cortical bone is osteons, and that of cancellous bone is a porous network of trabeculae. Cortical bone (compact bone) is a solid part allowing ~4% of its space for osteocytes, blood vessels, canaliculi, and erosion cavities. The cancellous bone (trabecular bone) is largely porous (50% - 90%) and filled with bone marrow (16,21). Aggregated type-I collagen and HA form the collagen fibril at the micron- and nano-scales. This reinforced collagen fibre is a universal building block for compact and trabecular bone.
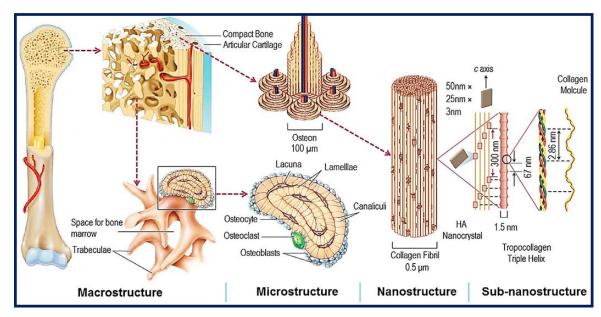
Fig. 2. Schematic illustration of the hierarchical structure of the natural bone, emphasising the distribution, shape, and size of the inorganic component (calcium hydroxyapatite in the collagenous matrix) (20,22).

2.1.2   Hip Anatomy

The cross-sectional view of the human hip joint is shown in **Fig. 3**. The femoral head, located in an anterior orientation, has articular cartilage lining along its surface except for a minor region in the centre called fovea capitus (23). The cup-shaped acetabulum is formed by the ilium, ischium and pubis in the lateral-anterior orientation. The lunate-shaped articular surface is filled with inferior acetabular fossa in the central region when viewed looking into the acetabulum. This fat-filled space contains a synovial-covered fat cushion (fibrofatty tissue), as well as the acetabular attachment of ligamentum teres. Fibro cartilaginous labrum is found overlying the perimeter of the acetabulum (24).
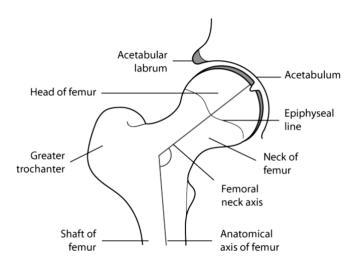
Fig. 3. Cross-sectional view of the human hip bone mentioning different anatomical terms of human hip physiology (11).

The triangular-shaped labrum arises from the bony rim of the acetabulum. The labrum is thickest posteriorly and decreases in size anteriorly (23–25). The multi-functional labrum is responsible for the containment of the femoral head by deepening the acetabulum during acetabulum formation and hip stabilisation (26,27). The ligamentum teres is covered with synovium and arises from the posteroinferior region of the true fossa of the acetabulum and finally inserts into the fovea capitis of the femoral head. It contains blood supply but does not contribute to hip joint stability. The fibres at the origin of the posteroinferior acetabulum blend in and are attached to the transverse ligament (11,28).
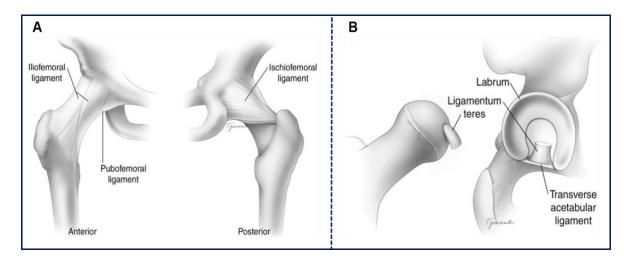
Fig. 4. Anatomical constraints of the hip. A. The anterior and posterior ligamentous constraints. B. Ligamentum teres arising from the transverse acetabular ligament. Anterior – positioned in the front. Posterior – positioned at the back. Labrum – fibrocartilage that keeps the hip joint in a fixed place. Ligamentum teres – a triangular band that helps hip stabilisation by enabling adduction, flexion and external rotation. Transverse acetabular ligament – strong load-bearing structure associated with the labrum (29).

The hip joint capsule is lined with synovium, inserted near the labrum base and shows a pink appearance at arthroscopy. The adjacent attachment of the capsule is along the osseous rim of the acetabulum (23,24). The capsule attaches distally at the base of trochanters (23). Three ligaments, namely, iliofemoral, ischiofemoral and pubofemoral, aid in reinforcing the capsule, as shown in **Fig. 4.** Another set of circular fibres called zona orbicularis appear at the femoral neck base, aligning with the joint capsule surface (30).

The greater trochanter acts as the primary site of attachment for powerful abductor tendons. The four facets of the greater trochanter with tendinous attachment and adjacent bursa are the anterior facet, lateral facet, superior posterior facet, and posterior facet. The anterior facet is situated on the anterolateral surface of the trochanter and has an oval appearance. The lateral facet has an inverted triangular shape and represents the palpable part under physical observation. The superior posterior facet accounts for most of the cranial part of the trochanter when viewed in an oblique transverse direction. The posterior facet is the posterior-most portion of the trochanter.

The trochanteric bursa is located posterior to the posterior facet, distal lateral to the gluteus medius tendon (lateral facet) and proximal to vastus lateralis insertion. The sub gluteus medius bursa is located deep down to the lateral of the gluteus medius tendon, covering the superior region of the lateral facet. The sub gluteus minimus bursa is located below the gluteus minimus tendon, medial and superior to its orientation in the anterior facet. The gluteus medius attachment is divided into three regions. The tendon attaches onto the lateral facet from posterior to anterior, the superior posterior facet and the anterior part of the tendon to gluteus minimus. The primary tendon of the gluteus minimus enters the anterior facet from its lateral and inferior aspects. The secondary tendon enters the ventral and superior portions of the capsule (31).

2.2 Musculoskeletal Disorders

The musculoskeletal system (locomotor system) in the human body works towards the body's movement and comprises bones, joints, muscles, tendons, cartilage, ligaments and connective tissues (8). Two major musculoskeletal disorders involving the hip joint are discussed below.

2.2.1 Osteoporosis

Osteoporosis is characterised by low bone mass and the deterioration of bone tissues causing increased risks of fracture. In India, approximately 230 million people are aged over 50 years in a population of 1.3 billion. According to clinical statistics, 20% of Indian women aged

over 50 years suffer from osteoporosis (32,33). With a female: male ratio of 3:1, over 1 million hip fractures incidence is estimated in 2050 (34). There are two types of osteoporosis, namely primary osteoporosis (with unknown cause) and secondary osteoporosis (with traceable cause) (31). Primary osteoporosis is furthermore classified as Type-I (post-menopausal, occurring between 50-70 years) and Type-II (age-related, <70 years old affecting both compact and cancellous bone), while secondary causes of osteoporosis are hypercortisolism, hyperthyroidism, hyperparathyroidism, alcohol abuse and immobilisation (35).

A Dual-energy X-ray absorptiometry instrument (DXA) is a commonly used technique to diagnose osteoporosis that measures bone mineral density (BMD). Diagnosis of osteoporosis is based on the T-score, which contains the BMD of femoral necks and lumbar vertebrae (36). BMD is clinically defined as a bone condition with a minimum of 2.5 standard deviations below the mean of the younger adult population. Currently, osteoporosis is prevalent in greater than 15% of the Asian population (>50 years old) (37). An ageing population and changing lifestyles contribute to the increasing prevalence of osteoporosis, and it has been recognised as a significant public health concern. The current treatment of osteoporosis inhibits bone resorption through several anti-osteoporosis drugs such as bisphosphonates (38).

Predominant first-line drugs (like bisphosphonates), anti-resorption drugs (like denosumab and calcitonin), bone breakdown process-reducing hormone therapies, oestrogen and raloxifene have been used as pharmacological treatments (39–41). In addition, non-pharmacological treatments such as calcium and vitamin D intake have also been used (42). However, these drug-based treatments cannot reverse the existing bone loss, and they also lead to serious side effects, including cancer and strokes (41).

2.2.2   Osteoarthritis

Osteoarthritis is a highly prevalent musculoskeletal disorder that affects nearly 300 million people around the world (43). Musculoskeletal disorders contribute to one of the most significant causes of pain and disability around the globe, prompting the WHO (World Health Organization), UN (United Nations) and nearly 19% of the countries in the world to create awareness about the disease burden and advanced treatment through research (44). Sometimes, joint stiffness or swelling after rigorous activities indicates the onset of osteoarthritis (45). A significant increase in the pain caused by this illness limits an individual's activity, interrupts sleep, causes fatigue, and consecutively reduces the quality of life (Osteoarthritis Research Society International, OARSI). Osteoarthritis significantly

affects the knee and hip joints more than any other joint. Radiographically confirmed symptomatic osteoarthritis is less commonly prevalent in the hip than the knee (46,47). Most clinical treatment guidelines on hip osteoarthritis have been extrapolated from the research results of knee and heterogenous populations of knee and hip osteoarthritis. This has limited the knowledge of specific characteristics of hip osteoarthritis, thereby restricting the implementation of effective hip osteoarthritis treatment (48–50).

Osteoarthritis is characterised by cartilage breakdown in joints (51). The deterioration of cartilage, leads to the rubbing of the bones of the joint against each other, causing pain and stiffness and leading to the impaired movement (51). Osteoarthritis is the third-largest musculoskeletal disorder after back and neck pain, accounting for 7.1% of the musculoskeletal burden. Primary and secondary osteoarthritis are the two types of such disease states.

Primary osteoarthritis is a chronic degenerative disorder resulting from genetic factors. Secondary osteoarthritis is caused by ageing, physical floor-level activities such as kneeling, and extensive squatting, and medical conditions like diabetes and obesity (45,52). These conditions are mainly prevalent in India, and thus osteoarthritis is a significant cause of concern for the elderly population.

Some of the causes of hip osteoarthritis include primary inflammatory arthritides, several metabolic diseases, and anatomical deformities (53). However, various risk factors are associated with this complex inter-network between cellular, mechanical, and biomechanical aspects causing osteoarthritis. They are broadly classified into demographics (age, gender, genetics), anatomic factors (joint shape, loads and alignment), lifestyle factors (obesity, metabolism, diet, occupation), some other possible associations such as muscle weakness, smoking, injury/surgery, bone mass and density, rigorous physical activity and finally pre-radiographic lesions such as synovitis, bone marrow, cartilage, meniscal abnormalities (39). The current care-of treatment for osteoarthritis heavily relies on temporary pharmacological medications such as paracetamol, Non-steroidal anti-inflammatory drugs (NSAIDs), corticosteroid injections, tramadol (54), and viscosupplementation (45). They aid in pain control and enhance functionality, but it is essential to highlight that they are not a cure for osteoarthritis.

A critical review of the clinical data showed a wide range of osteoarthritis prevalence in India among the elderly (17-60.6%) (55). The elderly population of India (above 60 years) is set to increase by 19% in 2050, making the economically dependent older women (greater than 80% of the aged population) vulnerable (56). The economic burden of osteoarthritis

involves direct costs (travel and surgery cost, cost of assistive devices, physical and pharmacotherapy costs, cost of management of side effects, consultation charges, investigation charges), indirect costs (loss of productivity, premature mortality, absenteeism, cost of coping) and lastly intangible costs (pain, depression, reduced quality of life) makes it challenging to implement clinical recommendations (44,57). Surgical treatments are a practical option for the clinical and economic burden and the risk involved (45,58).

There is increasing evidence that different phenotypes of osteoarthritis reflect different mechanisms of the disease (59). A phenotype is defined as a collection of distinct disease attributes representing dissimilarities in the patients related to definite outcomes of interest. The World Health Organization (WHO) defines a risk factor as any attribute, characteristic or exposure of the individual that accelerates the development of a disease (39). Some of the individual-level risk factors related to osteoarthritis progression are sociodemographic characteristics (age, gender, race) (60), genetics, obesity (high body mass index) (61), metabolic syndrome, vitamins and diet (62–65). Recent advances in illuminating the genetic framework of osteoarthritis report association with developmental pathways (43) Skeletal developmental genes are linked to joint (tissue) attributes before the onset of osteoarthritis such as cartilage thickness or joint shape, following different joint loading (66). Fibrosis and fibro-cartilage formation in the joint is a primary contributor to deteriorative changes in osteoarthritis (67). Based on patient-specific genetic makeup, individual reaction to joint trauma/damage is different, thus establishing the risk of osteoarthritis onset based on mechanical overload or trauma specific to each patient, thereby explaining the osteoarthritis diversity from patient to patient. Current pharmacological medications for osteoarthritis include acetaminophen, non-steroidal anti-inflammatory drugs, corticosteroids, etc (52). The current pharmacological treatments cannot prevent, halt or reverse the progression of osteoarthritis. This leads us to the discussion of managing and treating musculoskeletal disorders.

2.3 Clinical perspective and surgical management

Pharmacological and non-pharmacological therapies relieve the symptoms and aid in the management of osteoarthritis (68). However, when no alternative treatments/therapies are possible, total hip arthroplasty (surgical option) is the last resort. Total hip arthroplasty (THA) is an orthopaedic procedure recommended for patients having degenerative hip joint diseases such as osteoarthritis, avascular necrosis, rheumatoid arthritis, and trauma (69,70). In India, osteoarthritis is a general indication of THA (71).

The demand for THA is significantly increasing due to the ageing population, sedentary lifestyle, booming economy, and medical tourism. To add to the ease of accessibility for patients across the cross-section of society, the Indian government introduced the price capping of medical devices in September 2018 (72). As per the Indian Society of Hip and Knee Surgeries Registry (ISHKS) reports, a total of 10,407 hip replacements and 129,371 knee replacements have been performed by 150 surgeons till March 2017 (71). From 2017 to 2021, the number of procedures (primary + revision) increased to 20,288 and 232,919 for total hip and total knee replacements (TKA) respectively, as believed by the ISHKS registry.

Even though most patients return to normal level activity (lower level compared to before surgery), revision surgery may still be needed. One out of ten operations requires revision surgery (73). The main reasons for the failure of conventionally manufactured implants are implant instability, prosthetic joint infection, fracture/dislocation, wound complication, misalignment, stiffness, wear and tear, osteolysis, the concentration of metallic ions at the implant site, implant loosening, carcinogenesis, and revision surgery (70,74). Revision surgery is a serious procedure involving complications, especially for the elderly including death (75)Kuiper et al (73) reported that prosthetic stem loosening was the major reason for revision surgery, accounting for 64% of the cases in Norway. The most commonly reported cause of prosthetic loosening is stress shielding (76). Due to a mismatch in the stiffness of the cortical bone and prosthesis under loading conditions, the prosthesis shields the bone and absorbs a substantial amount of stress (77). Subsequently, the cortical bone is subjected to less stress, leading to stress shielding (78). As per previous studies, surrounding bone has lesser mass after prosthesis removal during revision surgery (79). As a consequence, prosthesis loosening can still occur after revision surgery. This procedure of replacing the prosthesis due to stress shielding highlights the need of removing/minimise stress shielding.

An increase in the ageing population, highly skilled surgeons, medical tourism, and expanding healthcare access and quality are major growth drivers of THA in India, as illustrated in **Fig. 5**. ISHKS registry has collected data of 34,478 TKAs and 3604 THAs, contributed by 42 surgeons across India **(see table 1).** From Table 1, some critical observations include that osteoarthritis contributes to 10% of THA cases in India. Whereas, osteoarthritis accounts for 97% of TKA cases. Patients over 52 years, majorly men, with a body mass index of around 25.8, underwent THA.

Table 1. Clinical data on Total Knee and Total Hip Arthroplasty of the Indian Population (71).

	Total Knee Arthroplasty	Total Hip Arthroplasty
Number of clinical cases	34478	3604
The average age of patients (in years)	64.4	52
Male: Female ratio	25:75	60:40
Body Mass Index (kg/m2)	29.1	25.8
Most Common Indication	OA (97%), RA (2.2%)	AVN (49%), OA (10%)

OA: Osteoarthritis, RA: rheumatoid arthritis, AVN: Osteonecrosis

The clinical data summarized in Table 1 emphasises that age, body mass index and gender play a significant role in total hip joint replacement. The national joint registry estimates a projected hip replacement survival rate of 89.4%, 70.2% and 57.9% at 15, 20 and 25 years (80).
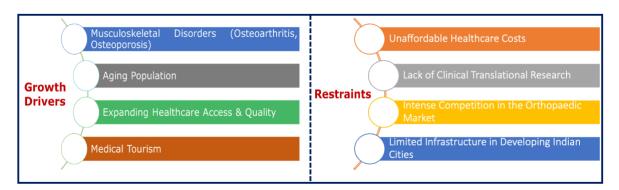
Fig. 5. Growth drivers and restraints of the orthopaedic market for musculoskeletal treatment.

Increasing demand for one of the most cost-effective orthopaedic procedures also brings along some complications (81). Modern implant design and improved surgical treatments ideally result in the improved long-term survival of hip joint replacements. However, unaffordable healthcare costs in developing cities largely restrict the growth of the Indian orthopaedic market. Especially, the spread of this procedure towards developing cities/towns of India with limited infrastructure and surgical expertise adds to the burden (82).

2.4 Biomechanics and morphometric analysis of the hip bone

The need for patient-specific implants can be better rationalised if we briefly discuss the anatomical features of the osseous system. This is explained below in the context of orthopaedic applications, particularly, total hip joint replacement. The subject of biomechanics is typically defined as applying the fundamentals of mechanics to the biological system. Following the preceding discussion in section 2.1.2, one would realise that the proximal femur experiences a remarkable functional impact on posture and gait. The interrelation between the shaft of the femur and the proximal femur is a fascinating research study (83–85). Radiography and CT scan data are the most common methods to analyse hip joint morphology. Morphometric evaluation of the proximal femur is essential in the management of hip disorders such as osteoarthritis. The hip joint is subjected to high interindividual anatomical variability, and there exists a disparity in the morphometric dimensions of the Indians as compared to the Western population (83).

2.4.1 Hip kinematics and kinetics

Hip joint kinetics and kinematics are dissimilar between healthy individuals and those with hip OA (86,87). The hip motion has its freedom in frontal, sagittal and transverse plans due to the ball and socket joint structure. This shape configuration generates stress magnitude and distribution. Maintaining stability while allowing mobility is a challenge to develop a prosthetic implant. The sagittal plane allows a wide range of motion, an average of 100° in flexion. In the frontal plane, the abduction range is 10° to 45° and an adduction range of 10° to 30°. The internal rotation can range from 30°-60° whereas the hip joint can externally rotate between 60°to 90°. However, these values are interindividual depending on the patient's geometry. Such values of hip motion involved in daily life are important to an orthopaedic surgeon (88). Gait is a pattern of limb movements during motion. Clinical measurements show that the hip joint has a maximum flexion of around 35° to 45° during the late swing phase of the gait. During this phase, the limb moves ahead for a heel strike. These motions are a vital investigation as they directly impact load-bearing implants, e.g., the hip implant under dynamic conditions (89,90).

Hip joint reaction forces are the forces that are generated due to the reaction of the forces acting on them. These forces need to be balanced with the moment arms of the body weight and abductor tension to maintain a levelled pelvis. The hip joint muscles contribute to the locomotion in different planes according to the hip position. Gluteus medius and gluteus minimus are the primary hip abductors during flexion and rotation and account for maximum compressive forces generated between the acetabulum and femoral head during the single

limb stance phase (91,92). The hip contact forces combine internal muscle contraction and ground reaction forces to body weight (88). Patients with hip osteoarthritis have decreased hip adduction, external rotation angles and pelvic obliquity (93–96). Correspondingly, the patients adopt an alternative gait pattern to increase mediolateral stability, thereby minimising stress on hip abductors (97–99). Furthermore, hip loading orientation is found to be medial in the transverse plane and vertical in the frontal and sagittal plane due to adopted hip kinetics and kinematics. As a result, the contact configuration between the acetabulum and femoral head is disturbed, thereby unloading a region of high osteoarthritis prevalence, i.e., the anterosuperior region of the femoral head (100).

According to Wolff's transformation law, the proximal femoral bone has compression and tensile trajectories by bending stresses acting upon the femur, influencing the bone structure (101). In vivo measurements in patients with hip prostheses show that force yielded during walking has a magnitude of 1.6 to 4.3 times the body weight and 1.5 to 5.5 times the body weight during climbing stairs (14,102–104).

Anatomical variation has many parameters associated with it, and gender is one of them, as shown in **Fig. 6A**. The sex-specific anatomical variation demands stress on hip contact forces on the major muscle group, i.e., hip abductors (105,106). According to the literature, healthy women walk with larger hip flexion and adduction moments, anterior pelvic tilt, internal rotation angles and minimised sagittal plane excursion as compared to healthy men (86,87,107–109).

The pelvis in females is broader than in males, and the acetabulum is situated deeper. Sphericity of the femoral head is essential in preventing osteoarthritis development. On the femoral side, a smaller femoral head diameter, greater femoral anteversion, thinner femoral shaft, smaller femoral offset, and lesser femoral neck-shaft angle compared to men. This means that women have higher hip forces than men. Moreover, after menopause, the bone mineral density decreases in women, elevating the risk of periprosthetic bone fracture (110–114).
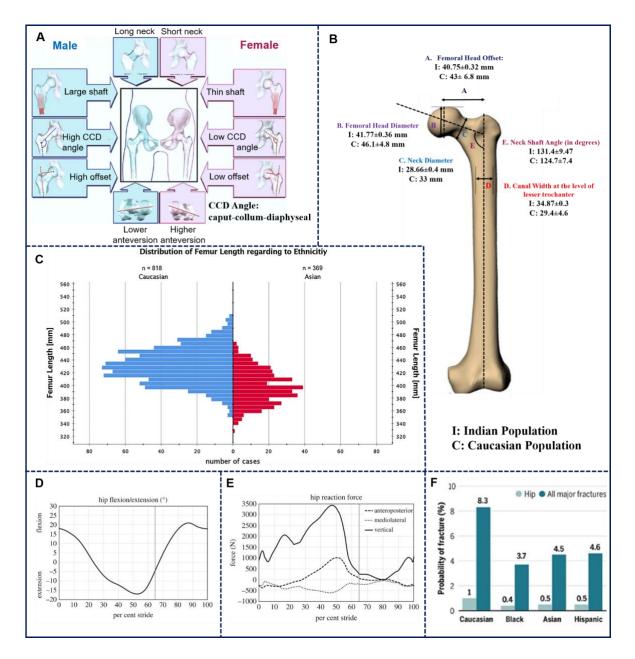
Fig. 6. Biomechanics and morphometry analysis of the hip bone showcasing interindividual differences in the hip anatomy. A. Gender-based differences in hip anatomy. B. Pictorial representation of the significant difference in the proximal femoral parameters of the Indian and Caucasian populations (88,115,116). C. Distribution of femur length in Indian and Caucasian populations (117). D. Extent of hip flexion and extension in a single stride. E. Hip joint reaction forces expressed in the global coordinate system (118). F. Probability of hip fractures in different ethnicities (119).

As mentioned earlier, age, gender and demography play an essential role in the clinical outcomes of the implants for musculoskeletal reconstruction. To illustrate the variations in the proximal femoral hip joint, a summary of the different femoral stem-related parameters is represented in **Fig. 6B.**

A comparison is made between the Caucasian and Indian populations concerning different femoral stem parameters. Based on the reported differences, as summarised in Table 2, there are differences in some parameters; the most striking difference is femoral head diameter, which varies around 46mm for Caucasian subjects as against 41.8mm for an Indian population. Further, canal width at the lesser trochanter is comparatively less for Caucasians (29mm) than the Indian population (35mm). Essential morphometric parameters to be considered during implant design are the neck-shaft angle (angle between the long axis of the femoral stem and long-axis femoral head). The neck shaft angle varied significantly between the two subject populations, i.e., 131° for Indians and 124° for Caucasians. The climate adaption theory can explain such ethnical variation, which states that a narrower pelvis is observed in lower latitudes to save heat and energy(88).

Table 2. Summary of the comparative morphometric analysis of the proximal femoral hip joint, as reported in different studies, Rubin et al. (120), Noble et al. (121), Siwach et al. (83), Sendhoorani et al. (122)

Morphometric Parameter	Rubin et al. (Swiss)	Noble et al. (Caucasian)	Siwach et al. (Indian)	Sendhoorani et al. (South Indian)
Femoral head offset (mm)	47±7.2	43±6.8	38±5.52	40.75±0.32
Femoral head diameter (mm)	43.4±2.6	46.1±4.8	43.53±3.4	41.77±0.36
Neck diameter (mm)	-	-	29.5±3.19	28.66±0.4
Canal width at the level of lesser trochanter (mm)	27.9±3.6	29.4±4.6	23.8±3.2	34.87±0.3
Neck shaft angle (°)	122.9±7.6	124.7±7.4	123.5±4.34	131.4±9.47

Table 2 represents a summary of the differences in characteristic geometrical features of the femur in different studies. According to studies by Siwach et al. and Sendhoorani et al., morphometric differences of the femoral hip joint exists between south Indians and the overall Indian population, indicating intra-regional diversification (83,122).

The probability of hip fractures among different ethnicities such as Black, Asians, Caucasians and Hispanics is shown in **Fig. 6F**. The Black, Asians and Hispanics were equally prone to hip fractures, whereas the Caucasians were highly prone based on the incidence of conditions concerning socioeconomic factors like lifestyle, activities, and genetics. Differences in hip morphology between individuals affect hip joint contact stress distribution as well as the gait cycle (123).

The distribution of femur lengths in the Caucasians and Asians is shown as a visualisation in **Fig. 6C**. Many Caucasian subjects had a femur length of 430 mm, whereas a femur length of 400mm was persistent among the Indian subjects. In the sagittal plane, the hip takes a forward stance in flexion of about 17° and into an extension of 17°, shown in **Fig. 6D**. The hip joint forces are the forces generated on the hip bone due to the application of loads. The hip reaction forces in a healthy person aged 36 years with a body mass of 74.3 kg and a walking speed of 1.15 m/s generated a vertical force of 3500N (**Fig. 6E**). Such information on hip kinematics and kinetics is essential in designing a femoral stem implant and advancement of enhanced rehabilitation strategies. Therefore, a combination of anatomical and geometrical parameters defines a hip's functional capacity.

2.5 Clinical treatment option: patient-specific implant

Recapitulating, osteoarthritis and osteoporosis are often marked by reduced bone mass and structural degradation of the bone tissue, promoting morbidity and risk of fracture in the hip, predominantly trabecular bone. With recent advances in medical imaging and computer programming, 2D axial images can be processed into reformatted views (coronal and sagittal) and 3D virtual models that depict a patient's anatomy (124). An orthopaedic surgeon may define 'patient-specific' as the distinctive bone geometry and density obtained using the patient's medical images. Patient-specificity is crucial as it can optimise the treatment of each individual by anticipating the outcomes of surgical interventions.

2.5.1   Femoral implant survivorship and clinical outcomes

Cementless femoral stems are expanding for use in THR fixation as they provide long-term survivorship with most stem designs (125). The majority of uncemented femoral stem designs are classified most commonly based on shape, amount of bone contact, fixation strategy from proximal to the distal femur and location of proximal loading (126)

Flat-wedge and dual-wedge femoral stems are popular for primary, cementless THA (127) Higher proportion of complex periprosthetic femur fractures occurred in patients with flat-wedge stems (128). Moreover, 30-month follow-up reported higher reoperations, stem

loosening and dislocation in flat-wedge compared to dual-wedge stems. The design of a flat wedge is related to these findings. Flat-wedge stem is thin and flat anteroposteriorly but wide and tapered mediolaterally, suggesting less cortical contact in both anteroposterior and mediolateral planes.

Cylindrical and tapered stems are extensively used stem designs for revision THA (129). Cylindrical femoral stem design provides close compression between the distal femoral cavity and implant, which helps in creating the environment for secondary bone growth. However, some studies have reported acute postoperative thigh pain, stress-shielding associated with cylindrical stems (130). Whereas, tapered stem design has been stated to minimise bone resorption incidence and attain bone regeneration in the proximal femur. Cumulative survivorship (8 years) for tapered and cylindrical design was 96.69% and 94.43% respectively. Postoperative complications recorded were higher by 8.4% for cylindrical stem design than tapered stem design and included intraoperative fractures, mild thigh pain, periprosthetic fractures, hip dislocation, and osteolysis (129,131).

The shape of the implant is a critical factor to regulate the degree of stress shielding (129). A tapered stem can be wedged to reduce implant stiffness compared to a cylindrical stem. Material is an equally important factor for reducing stress shielding. Ti6Al4V has bulk properties closely aligned to the human bone than most other metallic options i.e., low elastic modulus and biocompatibility, which makes it a popular choice for load-bearing orthopaedic implants (132).

Short stems have significantly risen as a choice for implant design to address implant failure issues, minimise stress shielding and aim to preserve the bone of the proximal femur (133–137). Due to its bone-preserving characteristic, short stems are usually recommended for young and active THA patients having sufficient bone quality (138). According to recent studies, short stems are also appropriate for elderly patients as they provide rigid fixation (139). The incidence of intraoperative periprosthetic fracture is reduced using a short stem due to less broaching; lowering blood loss, blood transfusion rates and operative time as a result (140–142).

The theory of calcar-guided short stem in THA, as classified by Khanuja et al., aims to sustain proximal bone stock for a prolonged time (136). This modern generation short stem design reconstructs the patient's anatomy by the guidance of the calcar of the femoral neck (143). The latest research findings have demonstrated that a patient's anatomy can be reconstructed for a large range of morphological parameters and offset, restoring the stem length (144–146). A study by Yan et al. reported the bone remodelling rate for calcar-guided

short stems is lower than conventional stems such as Zimmer Biomet, USA and Aesculap, Germany (147). Whereas, bone density measurements by Hochreiter et al. showed increased bone mineral density in lateral and distal-medial regions, demonstrating lateral loading (148). Therefore, stress shielding and periprosthetic bone loss are limited using this stem design.

Several national joint registries indicate that calcar-guided short stems show encouraging results for early-stage implant survivorship (149–151). The survival rate for five years is found to be 97.02% for elderly patients and 98.81% for young patients (152). Short and mid-term clinical results currently reported excellent implant survival, although, long-term clinical outcomes remain scarce (153–155).

2.6 Biomechanical analysis of the hip bone

The biomechanical conditions at peri-prosthetic bone remarkably affect extended osseointegration during the normal functioning of the implant. The patient's bone condition plays a critical role in the biomechanical analysis of peri-prosthetic bone. Differences in bone conditions result in varying biomechanical responses at the peri-prosthetic bone (156).

Finite element analysis (FEA) is one of the most versatile methods to scrutinise complex geometries and non-homogeneous material properties for biomechanical modelling. One of the prime advantages of FEA is that it accommodates structural optimisation of femoral implant design and exercises weight distribution throughout the implant design. FEA is an important tool for biomechanical analysis of stresses and strains in peri-prosthetic bone, and their communication within the biological system to predict appropriate prosthetic solutions, which are otherwise challenging to solve analytically (157–161).

Biomechanical studies reported in the literature have ignored the interindividual differences in muscle forces and hip joint morphology (162,163). Anderson et al. studied morphological differences in individuals and reported that they have a significant impact on contact stress distribution in the hip joint (164). Several biomechanical studies using different stem designs have been performed to minimize the stress-shielding effect by reducing femoral stem stiffness, i.e., lowering the elastic modulus of the implant (165–167). Other solutions to eliminate femoral stem stiffness include a selection of fundamental materials, and modifying internal structure, shape and geometry (168–176).

Incorporation of internal hollowness to introduce isoelasticity within femoral stems whilst preserving external morphology has been modelled for three decades (177,178). Internal hollowness was optimized by Gross and Abel, however, their studies used oversimplified

stem geometry and loading (179) Chatterjee et al. studied the impact of different bone conditions and subject weight on the biomechanical environment for the femoral stem (161).

2.7 Laser-assisted manufacturing of metallic implants

The rapid development of AM for orthopaedic implants is related to unique aspects such as the design of freedom, design to manufacturing capability with mass customization, and decreased lead time from design to supply chain (180). Additive manufacturing (AM) or 3D Printing (3DP) provides high geometrical flexibility for implant fabrication, ideal for patient-specific orthopaedic implants. Contrary to conventional implant manufacturing, AM increases implant performance, offers higher accuracy at a lower cost, manufactures implants in less time with better specifications, and produces parts with improved dimensional stability and near-net shapes (181,182). According to the ASTM International Standard, "ASTM F42 – Additive Manufacturing", 3DP is classified into seven processes: Vat Polymerisation, Binder Jetting, Material Jetting, Material Extrusion, Powder Bed Fusion, Sheet Lamination Directed Energy Deposition (183).

2.7.1 Selective Laser Melting

Selective laser melting (SLM), also known as laser-powder bed fusion (L-PBF), is a 3D printing technique with extensive customisation for orthopaedic applications. SLM comprises a powder delivery system in which the metal powder feedstock/reservoir is loaded and a build plate where the 3D printed part is built layer-by-layer. A high power-density laser guided by a computer-aided design (CAD) model selectively melts and fuses metal powder completely, forming a near-net shape printed part. The laser is generally a single-mode continuous wave solid-state fibre, functioning at 1075 nm wavelength. The process takes place inside a build chamber under an inert gas (argon) environment with the uninterrupted gas flow (184).

A recoater/wiper blade spreads the metal powder feedstock from the powder dispenser platform to the build platform, as shown in **Fig. 7A**. The powder dispenser and build platforms are mounted on a piston where the latter goes down a distance equivalent to the thickness of the slice/layer to be melted. This process is recurrent layer-by-layer until the final part is 3D printed.

Despite SLM's advantages, various challenges are associated with this technology. Firstly, SLM-manufactured components suffer from microstructural defects such as porosity and balling, significantly impacting the part's fatigue performance (185). Secondly, high cooling rates and temperature gradients present during the process give rise to residual stresses,

which contribute to crack growth behaviour (185). Several 3D printing parameters, including laser beam power, laser scan speed/velocity, layer thickness and hatch spacing, affect the microstructure of the printed part, as shown in **Fig. 7B.**
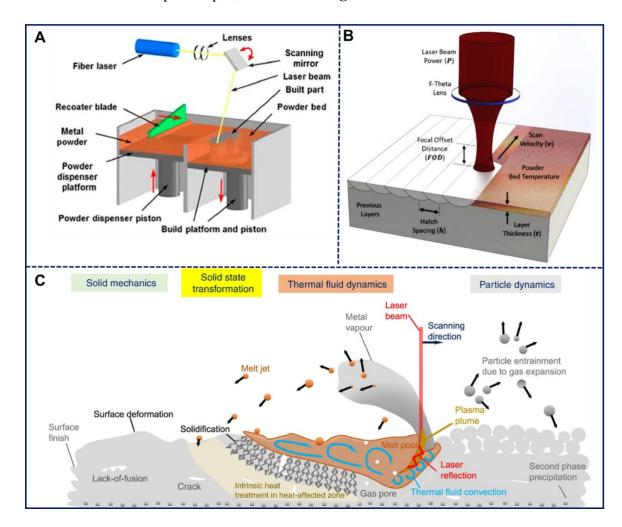
Fig. 7. Selective Laser Melting (SLM) process. A. Schematic of working principle of SLM, B. Illustration of printing parameter for SLM process, C. Physical effects and related physics taking place during SLM process (186–188).

These parameters control the cooling rates and, in turn, affect the part's mechanical properties. Additionally, optimising these parameters can manage the defects and challenges of this technique (189).

With a focus on understanding the origin of microstructural defects in printed parts, it is essential to leverage the knowledge of physical and chemical phenomena involved across different lengths and time scales, as shown in **Fig. 7C** (187). For instance, all four states of matter, i.e., solid, liquid, gas and plasma, interact at the laser-metal interface (190). Moreover, recurrent rapid thermal cycles generate thermal gradients, producing physical, chemical and mechanical metastable states that influence process stability and quality of the as-built part (191).

The high photon/electron energy by the laser beam is transformed into thermal energy by absorption that irradiates the powder bed during heating (192). The powder bed provides deep penetration as a result of numerous reflections at the powder particle surface as opposed to opaque continuous material (192,193). The absorbed thermal energy is dispensed based on the relative density and reflectivity of the top powder layers of the powder bed. Heat convection occurs among metal powder and shielding gas during the SLM process, and heat conduction further distributes the absorbed thermal energy to the material, resulting in reduced temperature peaks at the surface.

After preheating the base plate, the build temperature is elevated for melting, while sinter necks connect the single powder particles, thereby reducing the thermal gradient during manufacturing. Consequently, the sintered powder particles serve as support structures for subsequent manufacturing, resulting in elevated thermal conductivity. While processing, the metal powder melts, forming a melt pool. Thermal fluid (melt pool) convection is determined by external forces such as surface tension, gravity, buoyancy, Marangoni effects or evaporation pressure (194). Marangoni forces raise the heat transport by inducing fluid motion further from the temperature apex in the melt pool centre (195,196). The material evaporates due to raised melt pool temperature, leading to recoil pressures inducing fluid motion. The recoil pressures cause the keyhole defect, forming a vapour capillary (197). Solidification of material takes place after melting and consolidation. The material shrinks during solidification, leading to process-induced stress that minimises during subsequent layer processing, also called residual stress (198). The residual stresses inside the part give rise to distortions and cracks (198,199). A particular microstructure evolves depending on the thermal gradient and cooling rates (200). In the final step, a new powder layer is applied whose characteristics depend on the previous layer's surface and powder properties. A highly dense part is ultimately desired, a function of powder flowability.

Clearly, the laser-metal interaction is complicated in SLM, and the level of metal powder sensitivity to the laser action is ambiguous. Consequently, reused and sieved powder is often a risk affecting the repeatability of the mechanical properties, assembling expensive waste. Moreover, the price of metal powder is very high (i.e., ~£600/kg of Ti6Al4V), and only up to 50% of total powder feedstock is contained in the dispenser to build a part. As a matter of fact, metal powder costs could be doubled without a smart recycling strategy (201–203).

2.7.2 Dimensionless numbers

Dimensionless numbers can capture the process parameter relationship on microstructure, properties and defects. Dimensionless numbers reduce the overall process variables and

provide insight into an influential group of variables. **Table 3** summarises the prime dimensionless numbers for laser-based AM and can be applied to other heat sources as well (204).

Table 3. Dimensionless numbers for the laser-based AM.

Dimensionless Number	Formula*	Definition	References
Marangoni number	$$M_a = \frac{d\sigma}{dT}\frac{dT}{dx}\frac{L^2}{\eta\alpha}$$ where σ is the surface tension, dT/dx is the temperature gradient, α is the thermal diffusivity, L is the characteristic length, and η is the viscosity of the melt pool.	The ratio of surface tension force to viscous force	(205,206)
Peclet number	$$P_e = \frac{U L}{\alpha}$$ where U is the characteristic velocity, α is the thermal diffusivity of the alloy, and L is the characteristic length.	The relative strength of convective heat transfer to conductive heat transfer in the system	(207)
Fourier number	$$F_o = \frac{\alpha\tau}{L^2}$$ where α is the thermal diffusivity, τ is the characteristic time scale, and L is the characteristic length	The relative value of heat dissipation and rate of heat storage	(208)
Non-dimensional heat input	$$Q = \frac{P / V}{P_r / V_r}$$ where P is the laser power, V is the scanning speed, P_r is the reference laser power, and V_r is the reference scanning speed	The energy required per unit length of the material to deposit successive layers	(204)

*Characteristic length denotes either layer thickness, melt pool width/depth, laser spot size; characteristic velocity denotes the maximum velocity of melted metal; characteristic time denotes melt pool length divided by scan speed.

Dimensionless numbers can be used to gain broad understanding of the structures and properties of AM parts. High Marangoni number results in large melt pools due to strong circulation of molten metal in the liquid pool (209). At the same time, lower Marangoni number leads to poor interlayer bonding and therefore high porosity (210). Peclet number (Pe) indicates the significance of convective heat transfer above conductive heat transfer. If Pe>1, convective heat transfer is better facilitated. A high Fourier number suggests faster heat dissipation which results in a higher G/R ratio (G, temperature gradient and R, solidification rate) and fine microstructure upon solidification (210). A high non-dimensional heat input produces large grain size and low hardness, as a result of slow cooling (210). Dimensionless numbers is also used to mitigate defects such as porosity, dimensional inaccuracy and lack of fusion. A high non-dimensional heat output has lesser voids whereas high Fourier number results in distortion (210).

2.7.3 Inherent defects

Defects can arise during the printing process of the material. Known causes of defects help in taking adequate measures to minimise/remove them. Some of the common defects encountered in laser-based AM systems are discussed in the following sub-sections.

2.7.3.1 Porosity

Porosity is a common defect in AM (211–213). Porosity adversely affects the mechanical properties of the L-PBF manufactured materials (214). Three main methods in which porosity occurs are described. One is the formation of spherical voids inside the deposit due to the operation of AM process in keyhole mode (215). Two, gas entrapped inside powder particles during the powder atomisation process (216). Shielding gas can also be entrapped inside the melt pool. Third, inadequate penetration of melt pool on the substrate/build platform or previously deposited layer (217,218). Based on the above descriptions, porosity can be of two major types: Interlayer and intralayer porosity. Interlayer porosity occurs due to insufficient input energy to fuse metal particles, leading to the formation of un-melted regions. These pores are large and non-uniform in shape, possibly due to rapid solidification cooling rates. Intralayer porosities are caused by gas entrapment. They appear in random areas having low solidification cooling rates, as shown in **Fig. 8B** (219–221).

Therefore, it is necessary to control metal powder particles' shape and size and maintain adequate processing parameters during laser deposition (216). Increasing laser power leads to a larger melt pool size, thus increasing penetration depth and reducing porosity (222).

Commonly used techniques to measure porosity are Archimedes' principle, optical microscopy, and X-ray computed tomography.

2.7.3.2 Chemical composition changes and loss of alloying elements

The solute particles are redistributed during the addition of several layers. A difference in chemical composition at the substrate-deposit interface occurs. Redistribution gives rise to solute segregation and heterogeneous microstructure. The quantity of solute segregation is proportional to solidification cooling rates (223,224).

An alloy system sometimes can have a difference in the volatility of its elements. Preferential vaporisation of the alloying elements during DED can occur at high melt pool temperature, causing overall chemical composition changes in the alloy (217). Chemical composition change can be predicted by accurate estimation of temperature distributions and melt pool geometry. Process variables that affect chemical composition change are laser scan speed, laser power, powder feed rate, and laser spot size. Thus, controlling these process variables can minimise the loss of alloying elements.
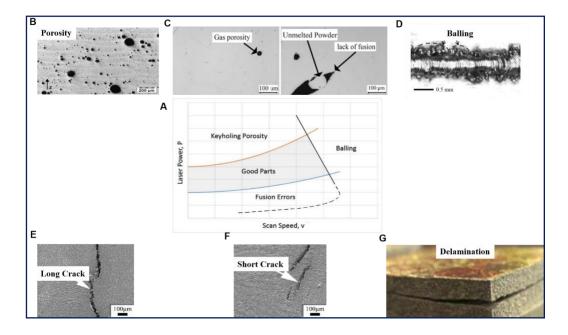
Fig. 8. Different process-induced defects in metallic components primarily determine the quality of 3D printing parts. These defects result mainly from using the appropriate laser power and scan speed, as shown in A. B. The experimental observation of porosity, C. Lack of fusion, D. Balling, E. Long cracks, F. Short cracks, G. Delamination of large components (225).

The typical morphology of different processing-induced defects are shown in the context of laser-based powder fusion processes. In **Fig. 8A**, the appearance of fusion errors, balling,

keyholing, and porosity is a function of laser power and scan speed. It is important to emphasize that one must use the range of laser power and scan speed to obtain defect-free metallic parts; such combinations vary from metal to metal. The typical pore sizes range from 50 to 200 microns shown in **Fig. 8B**. There are also unmelted powders retained in laser 3DP parts with signatures of lack of fusion, shown in **Fig. 8C**. Another critical defect is often reported in 3DP metallic parts is balling, **Fig. 8D**. Depending on how closely various defects exist in microstructure, it is possible that these defects coalesce together, or can be joined together to form a long or short crack in printed structure. Under extreme conditions, these cracks can lead to delamination of the entire printed parts **Fig. 8G**. Based on these observations, it is essential to emphasise that one has to optimise parameters in laser-based PBF processes to obtain defect-free components in different metallic systems.

2.7.3.3 Surface roughness

Surface roughness on AM-manufactured parts results from co-dependent input parameters such as part and design parameters (part orientation, feature geometry), process selection, process parameters (laser power, scan speed, layer height, profile paths), material (powder morphology, particle size distribution), post-processing, finishing. Resulting output parameters such as unmelted particles, lack of fusion between layers, shown in **Fig. 8C**, and partial fusion of powder particles affect part performance (226). Optimising these input parameters can control the part performance. To conclude, decreasing layer thickness and scan speed, increasing laser power, and selecting small-sized solid particles help in reducing surface roughness.

2.7.3.4 Cracking

The temperature of the previously deposited layer is lower than the depositing layer. Thus, the solidifying deposit contracts more because of thermal contraction and solidification shrinkage. Due to this phenomenon, internal stress is generated at the solidifying deposit layer. Solidification cracking is observed at grain boundaries when the generated tensile stress is greater than the strength of the metal (227). Liquation cracking is observed in partially fused regions of the build(228). Cracking can spread along the deposit layers, equal to the layer thickness, shown in **Fig. 8E, and Fig. 8F**(229). Delamination is caused by residual stresses at two consecutive layer-interface, exceeding the yield strength of the alloy, shown in **Fig. 8G** (230).

2.8   Life cycle assessment and carbon footprint of metal manufacturing methods

Several review papers have focused on process science and microstructure development, particularly microstructure-property correlation (226). However, very few reviews have emphasised the application of 3D printing for translational research on biomaterial implants and related advantages in global sustainability over conventional manufacturing of metals. Aspects concerning the global sustainability of 3D printing include the environmental impact of 3D printing for medical applications. The industrial sector adds 29% to the total energy consumption and 42% (12.3 Gt CO_2) to the global warming potential (CO_2 emission), as reported by International Energy Agency (IEA) in 2018 (231). 3D Printing has sustainable advantages over conventional metal manufacturing methods, including material waste reduction, material recycling, design optimisation and producing lightweight components (232). Primary concerns of environmental impact include energy efficiency, material utilisation, life cycle assessment (LCA), global warming potential and pollution (233). Eco-friendly manufacturing, such as 3D printing and the FAST processes, has been considered an effective strategy to reduce carbon emissions toward global sustainability (234).

Life Cycle Assessment (LCA) is a primary method to evaluate the environmental impacts of the metal manufacturing process. It allows the quantification of raw material and energy resources along the product's life cycle phases (235). LCA assesses all the steps involved in product life, including process energy, material consumption, carbon emissions, and wastes (234).

2.8.1   The energy efficiency of metal manufacturing methods

The total energy consumption of metal manufacturing involves the primary energy from the energy source and secondary energy for the manufacturing/powder metallurgy process (236). Metal 3D printing consumes only 30-50% of the energy of conventional manufacturing (CM) of metals (234).

The energy consumption of a given AM process depends on the material's heat capacity, build volume, layer thickness, process speed, and powder density (233,234). Among the various 3D printing methods, Laser Powder Bed Fusion (L-PBF) is the least eco-friendly process. It is worth considering that the energy consumed in mining and primary production for wire-based raw material is more extensive than powder-based raw material. However, the printing energy consumed for wire-based AM is lower than that consumed in powder bed fusion processes (234). Energy efficiency (MJ/Kg) is the energy consumed per mass of material deposited and depends on the capacity utilisation of the process (237). Total primary
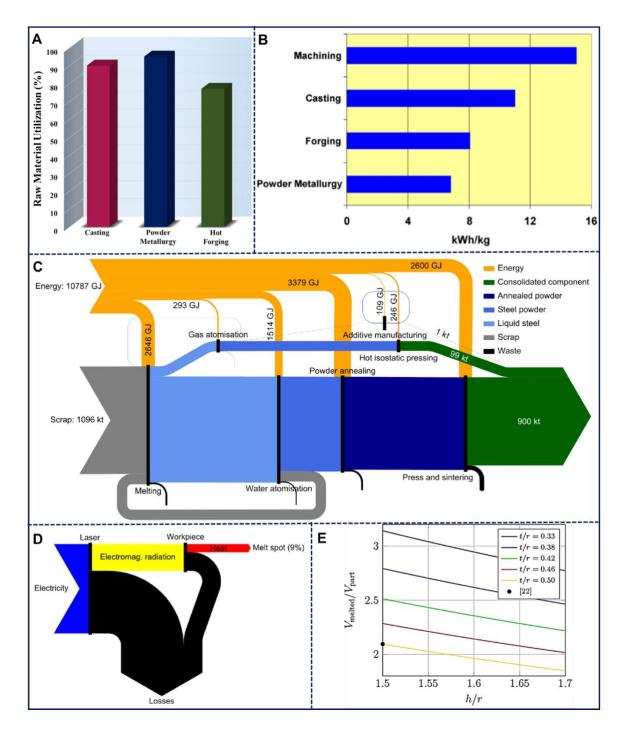
Fig. 9. Total energy consumption of metal manufacturing methods involves energy from source and manufacturing. A. Raw material utilisation (%) for various metal manufacturing methods, B. Energy consumption per kilogram for different net-shape manufacturing processes, C. Sankey diagram showing the flow of material where the proportion of the mass of material is similar, D. Energy flow through a laser beam for additive manufacturing explaining lower energy efficiency, E. Plot showing the volume of material melted per part in selective laser melting process as a function of hatch spacing, h, layer thickness, t, and melt pool radius, r (238–240).

energy supply (TPES) that indicates the sustainable implications of energy are diminishable by 2.54-9.30 EJ over a complete life cycle (241). The energy savings are primarily contributed by reduced resource production and energy use, given that AM uses lesser material than its conventional counterparts (242,243).

Fig. 9A shows the percentage of raw material utilised in powder metallurgy (which includes the FAST process) versus conventional metal manufacturing methods. Powder metallurgy tops with a 95% raw material utilisation rate correlating to lower energy demand per part (239). Average energy emission/expenditure in the manufacturing sector is not well reported in the literature, and most articles report the energy expenditure made by the calculations based on parts manufactured. An integrated overview of the energy consumed per unit mass for several net-shape manufacturing processes is shown in **Fig. 9B**. From the figure, powder metallurgy includes 2 kWh/kg of energy consumed for powder production and uses twice as less energy compared to machining and slightly above one-tenth compared to casting (240). A Sankey diagram, including the energy and material flow for the steel production chain, is shown in **Fig. 9C.** This diagram maps the contribution of energy consumed by several metal manufacturing methods. Support material/structure used in additive manufacturing includes material losses much wider than total production. Metal melting consumes the same amount of energy as powder press and sintering (conventional powder metallurgical process).

In contrast, the FAST process consumes about one-fifth of the energy consumed by conventional powder metallurgical processes such as hot isostatic pressing, hot press sintering, and pressureless sintering (238,244). Currently, the FAST process consumes lesser energy and material losses as it requires powder with large particles. The amount of gas needed to produce large particles is lesser than smaller particles. Metal AM is yet to be optimised as it is still in the early stages with only 1.3% energy efficiency, as explained in **Fig. 9D**. The laser energy source for powder bed fusion processes has only 9% of the energy actually reaching the workpiece. The ratio of the volume of material melted to the volume of the final part produced using metal AM is shown in **Fig. 9E**. The ratio depends on the printing parameters, but nearly twice the volume of the final part produced is melted. Such ratios as a function of printing parameters can be the catalyst for improving material and energy efficiency (238).

2.8.2 Economic assessment of metal manufacturing methods

Additive manufacturing has significant advantages in producing patient-specific implants with cost reduction. In contrast, conventional manufacturing remains inexpensive for the large-volume production of medical implants (245). The production time taken for

prostheses and implants by AM is lesser than that of conventional methods (milling and forging); therefore, increased productivity ultimately diminishes the product cost (246,247). The primary AM production costs are material costs, build rate, machine costs, and utilisation rates, whereas the secondary costs are pre-processing and post-processing products (248,249). The build chamber size and build speed of the 3D printer greatly influence the production costs and are expected to rise by 2030 (250). Overall, the improved quality and decreased cost will give rise to part candidates.

2.8.3 Global warming potential of metal manufacturing methods

Manufacturing attributes to 98% of direct CO_2 emissions from the industrial sector (251). Material production occupies 21% of global energy demand and contributes to 20% of global CO_2 emissions (252).

The International Energy Agency has reported that direct greenhouse gas (GHG) emissions have increased by 70% from 1990 to 2014 in the industrial sector (253). Simultaneously, the economic output escalated quicker than its GHG emissions, which led to a 5% dip in the direct GHG/unit of economic output, as shown in **Fig. 10A**. To achieve the set target in 2050, the next step is decarbonising the industrial sector. The primary energy consumption and CO_2 emissions at every stage of the life cycle for manufacturing metals make the Life Cycle Inventory (LCI). From the viewpoint of the environment, material savings are feasible using AM over conventional manufacturing (242). Ti6Al4V is the most popular alloy for load-bearing implants. The CO_2 emission of the several AM processes for 1 Kg of titanium part for aerospace is plotted against conventional (CNC machining) counterparts in **Fig. 10B**. It can be deduced that AM allows approximately 400% - 800% lesser CO_2 emission than traditional methods such as CNC machining due to minimal material usage for fabrication. Among several AM techniques, wire-based AM emits an enormous amount of CO_2 during manufacturing (254).
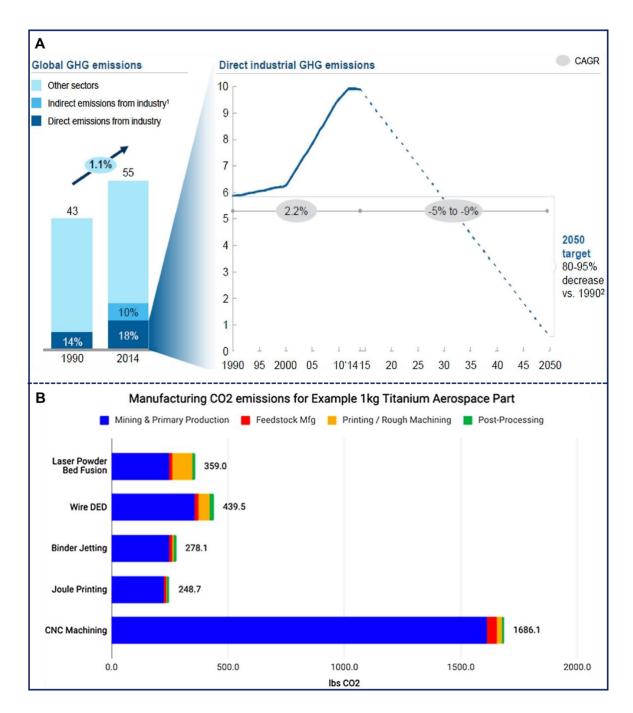
Fig. 10. Environmental impact of industrial and manufacturing sectors that include direct and indirect gas emissions. A. Global Green House Gas (GHG) emission outline of the industrial sector from 1990 to 2014, implying that direct and indirect emissions will need a steep drop to achieve set targets at the end of 2050. CAGR: Compound Annual Growth Rate, B. Carbon dioxide emission (CO_2) per kg of titanium using conventional and additive manufacturing (254,255).

Several studies have compared the environmental impacts of AM and CM methods (243,256–263). Published literature shows no data on the LCI, primary energy consumption and CO_2 emissions at each stage of the Ti6Al4V hip implant life cycle. Ronan et al. have compared the EBM process (AM) with milling (CM) for an operative Ti6Al4V knee implant,

as shown in **Fig. 11.** The life cycle is divided into four discrete stages, i.e., raw material extraction and preparation, metal workpiece production, part manufacturing and post-processing, and part recycling (264). All values are expressed in kilogram (kg) and per part basis, where AM values indicate the energy required to add 1 kg of material and CM values indicate the energy needed to subtract 1 kg of material. The background process and input energy implicate the electricity produced and materials required in knee implant manufacturing, as shown in **Fig. 11A**.

Raw material extraction and preparation, the first two steps of Ti alloy powder/workpiece production, and Ti recycling are the same for AM and CM methods. As the production and recycling of Ti alloys are cost and energy-extensive, raw material waste is a remarkable shortcoming in conventional manufacturing methods. The rutile mining process to produce 1 kg of Ti has specific energy consumption (SEC) of 29.8 MJ/kg, shown in **Fig. 11B.** Kroll's process is most exclusively used for obtaining Ti from $TiCl_4$. The specific energy consumption (SEC) for the Kroll process is 445.74 MJ/kg. Approximately 28.19 kg CO_2/ kg Ti is associated with CO_2 emissions for Ti production in the Kroll process (265). The CO_2 emitted per kg of Ti produced is 28.19, as shown in **Fig. 11C**. Whereas the associated CO_2 emissions for the vacuum arc melting alloying process (to form Ti6Al4V by joining Ti, Al and V) is 1.11 kg CO_2, for Ti6Al4V powder is 5.13 kg CO_2, and 1.15 kg CO_2 is produced for Ti6Al4V workpiece. The EBM (AM) process, including the post-processing operations, is shown in **Fig. 11D**.

For a Ti6Al4V component with the weight and geometry of a knee implant, 9.7 kg CO_2/kg of Ti6Al4V is emitted for a PEC of 176.35 MJ/kg (264). Commonly used post-processing techniques for EBM include milling and grinding, and a value of 4.43 kg CO_2 and 3.82 kg CO_2 per kg of Ti6Al4V is calculated as CO_2 output for a PEC of 149.85 MJ/kg. Comparing the PEC and CO_2 output for CM, considering the same mass and geometry of a knee implant, only 0.72 kg CO_2/kg of Ti6Al4V is emitted as opposed to 9.7 kg CO_2/kg in AM as illustrated in **Fig. 11E**. Finally, the LCI for end-life recycling of knee implant remains the same whether for AM or CM, and the approximate CO_2 output is 5.2 kg CO_2/kg Ti recycled, shown in **Fig. 11F**.
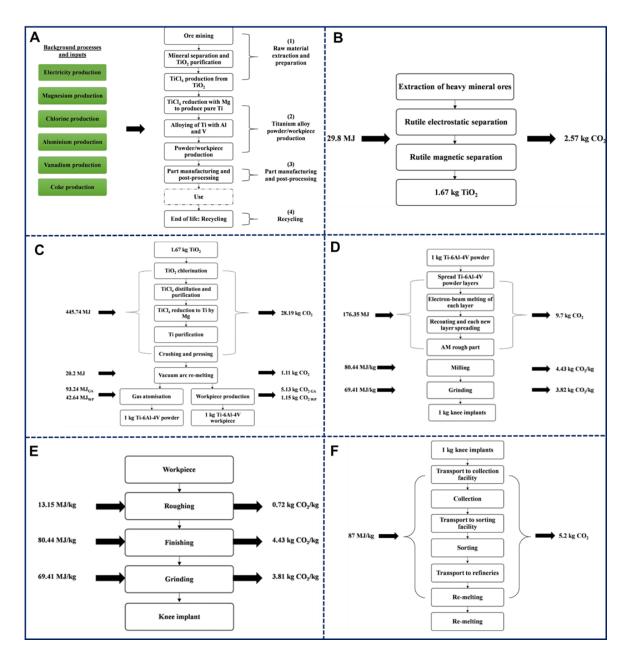
Fig. 11. Life cycle inventory, primary energy consumption and CO_2 outputs at each stage of Ti6Al4V knee implant using additive and conventional manufacturing. A. Background process, inputs, process flow and life cycle stages for manufacturing Ti6Al4V knee implant, B. Primary energy consumption (PEC) and CO_2 output for rutile mining process, C. PEC and CO_2 output for Ti powder alloy/workpiece production, D. PEC and CO_2 output for AM process, E. PEC and CO_2 output for CM process, F. PEC and CO_2 output per kg of Ti6Al4V knee implant recycling (264).

Solely considering the manufacturing process, AM consumes double the PEC of CM; however, only 22.6% of the material required for CM is needed for AM. For the knee implant discussed in **Fig. 11**, 84.6% of Ti6Al4V material is wasted using CM that needs to be translated into a reusable form, whereas only 35% of material is wasted in AM. Ti6Al4V has the highest embodied energy, with a value of 475.54 MJ/kg. Therefore, CO_2 emissions

per part for manufacturing using AM and CM are 11.47 kg and 45.24 kg CO_2, respectively. However, considering only the manufacturing stage, including post-processing, AM is 2.07 times higher than CM (264). Therefore, better material utilisation enables less GHG emissions in AM, making it an environmentally-friendly choice.
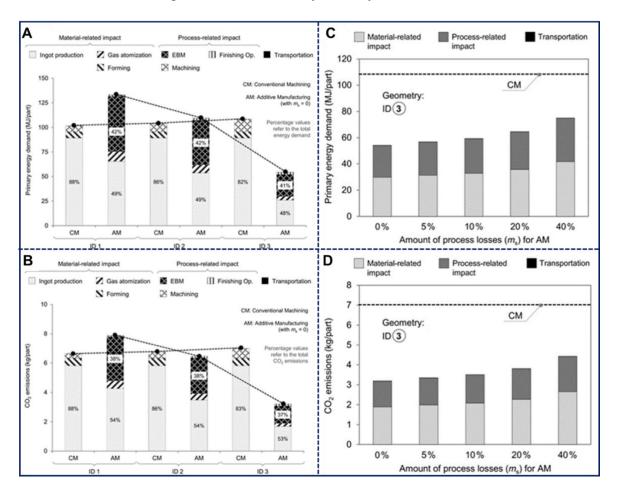
Fig. 12. Variations of energy demands and CO_2 emissions in additive manufacturing (EBM) and conventional manufacturing. A. Shares of the primary energy demand for three differently shaped components using AM and CM, B. CO_2 emissions for different components using AM and CM, C. Variations in the energy demand as a function of process losses for AM and CM, D. Variations in CO_2 emissions related to the amount of process losses (%) using AM and CM. *Note:* The impact of transportation is negligible. CO_2 = carbon dioxide; EBM = electron beam melting; kg = kilograms; MJ = megajoules (243).

The life cycle analysis for PEC and CO_2, along with variations in energy demand for three different case studies (referred to as ID 1, ID 2 and ID 3), are plotted in **Fig. 12**. Overall, it is fair to say that material-related impact significantly influences the environment and energy. The choice of the manufacturing method depends on the component's complexity, as distinctly seen in **Fig. 12A and Fig. 12B** for ID 1 and ID 3 (thin-walled component). The PEC and CO_2 emissions as a function of process loss are plotted in **Fig. 12C and Fig. 12D**.

As the value of process loss varies from 0% to 40%, the energy demand and CO2 emissions increase accordingly. Higher values of process losses over 100% are required for a given component to make CM preferable over AM, as shown in **Fig. 12C and Fig. 12D**.

2.9 Microstructure development in Ti6Al4V

Ti6Al4V is an α + β alloy containing 6 wt% Aluminium and 4 wt% Vanadium. The microstructural evolution of Ti6Al4V depends on its thermomechanical behaviour as a function of the manufacturing process. The microstructure or phases, i.e., alpha (α), beta (β) or alpha + beta (α+β), determine the physical and mechanical properties of Ti6Al4V. At room temperature, Ti6Al4V microstructure at equilibrium exists as alpha phase (hexagonal close-packed, hcp) and retained beta phase (body-centred cubic, bcc) (266).

2.9.1 Ti6Al4V phase diagram

Titanium and its alloys acquire their properties from pure titanium's allotropic modifications at 881°C from the low-temperature hcp (alpha) phase to the high-temperature bcc (beta) phase, as shown in **Fig. 13A** (267)**.** The capability to influence these properties depends on the beta transus temperature of the alloy, the physical and mechanical behaviours of the phases (267). Therefore, various microstructural combinations can occur based on the alloying of these two phases, which have different physical and mechanical behaviours. The two-phase α + β alloys, such as Ti6Al4V, provide a variety of combinations of strength, toughness and high-temperature properties. While single-phase α alloys offer corrosion resistance of titanium, β alloys provide low modulus and biocompatibility with fatigue strength and adequate toughness for biomedical applications (267).

Allotropic phase transformations in titanium and titanium alloys give rise to a crystallographic relationship between the parent β phase and daughter α phase. According to Burger's orientation relationship (BOR):

$\{0001\}\alpha \,||\, \{011\}\beta$ and $<11\bar{2}0> \alpha \,||\, <111> \beta$ (268).

Each orientation of α gives six β variants during heating. β → α transformation results in 12 distinct α variants from a single parent β grain. Therefore, one α orientation provides 72 different orientations during solution treatment. However, all 72 orientations do not have equal probability, and β → α transformation occurs with variant selection (269–275). Diffusion and shear mechanisms are two commonly accepted phase transformation mechanisms in titanium alloys.
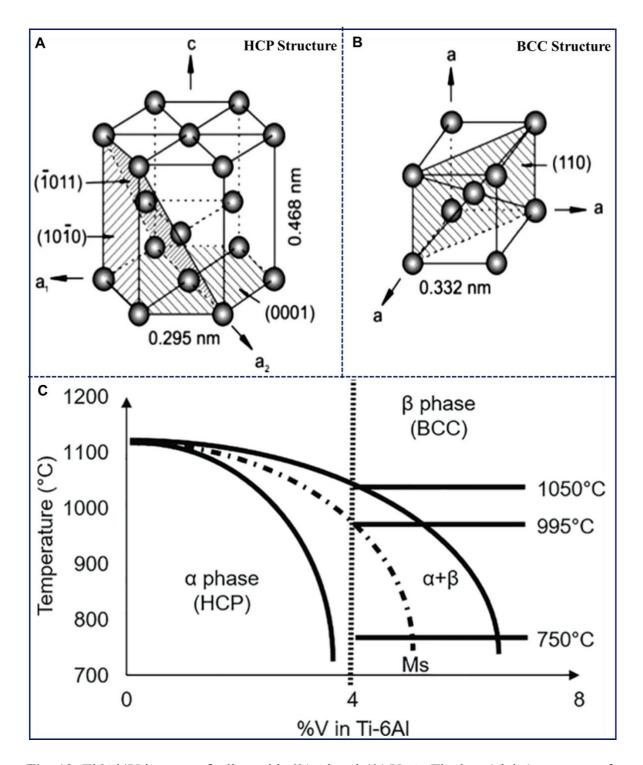
Fig. 13. Ti6Al4V is an α + β alloy with 6% Al and 4% V. A. The hcp (alpha) structure of titanium, B. bcc (beta) structure of titanium, C. Equilibrium Phase diagram of Ti6Al4V (267,276).

The α + β microstructure is classified into several types depending on the prior heat treatment and cooling rates (277). For slower cooling, above the β transus temperature in Ti6Al4V (995± 20°C), the β phase usually transforms into primary globular α by diffusion mechanism and into martensite α' phase for higher cooling rates using the shear mechanism. The nucleation rate of α is enhanced upon increasing the cooling rates, leading to the formation

of α platelets/laths in prior β grains. The cooling rates and prior beta grain size determine the width and length of α laths. Slow cooling through the beta transus temperature leads to Widsmanstaten plates of α by nucleation and growth.

The Widsmanstaten α can have different morphologies based on cooling rates. Slow cooling rates favour the formation of similar α platelets aligned in colonies stacked upon one another. In comparison, faster cooling rates result in basketweave microstructure, represented by the random arrangement of coarse grains with a substantial amount of α phase at the centre and relatively smaller amounts of β phase at the grain boundary (278). Basketweave structures have a more uniform distribution of the 12 variants that appear at low transformation temperatures due to fast cooling. Upon rapid cooling/quenching, the β phase completely transforms into martensite α. Martensite exists as hcp (α') or orthorhombic crystal structure (α''), depending upon the amount of beta stabilisers.

At moderately fast cooling rates, grain boundaries α is prominent, increasing in thickness and amount with decreasing cooling rates (279). Since grain boundary α can form a Burgers relationship with any of the neighbouring β grain, a choice of 24 variants is available, of which one or two dominate in a given grain boundary. If adjacent β grain boundaries share a common {110} plane, the preferred variant always has its basal plane parallel to this common β {110}. Otherwise, the preferred variant will be that which has its close common close-packed direction, $<1\bar{1}1>β // <11\bar{2}0>α$, lying closest to the boundary plane. **Fig. 13B** is a schematic illustration of the equilibrium phase diagram of Ti6Al4V.

2.9.2 Initial microstructure of additively manufactured Ti6Al4V

According to several studies (277,280–282), the microstructure evolution of Ti6Al4V mainly depends on the cooling rate when beta transforms to alpha along with the transus temperature. The typical microstructure in different AM processes such as L-PBF, DED WAAM and EBM are discussed in this section. Typically, during the DED process, the deposited layer has two distinct morphologies in Ti6Al4V due to heterogeneous nucleation, i.e., fine equiaxed beta grains and large columnar grains, as shown in **Fig. 14H and Fig. 14I** (283). The equiaxed beta grains are more prominent near the surface region and columnar grains near the melt pool bottom region. A deep melt pool having a low mass deposition rate leads to epitaxial growth of large, columnar prior β grains.
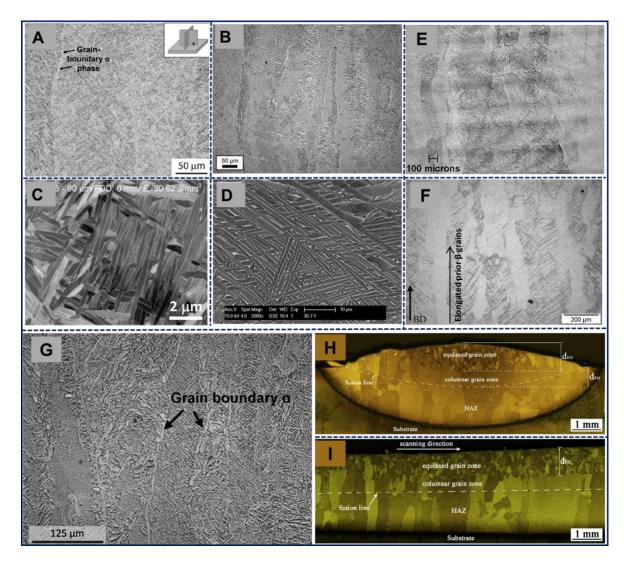
Fig. 14. Microstructure of Ti6Al4V produced by different AM methods as a function of different cooling rates. A. Fine lamellar Widmanstatten structure by Directed Energy Deposition (DED) process, B. Both colony and Widmanstatten morphology observed using Electron Beam Melting (EBM), C. Lamellar α + β structure shown using Laser Powder Bed Fusion (L-PBF), D. Wire Arc Additive Manufacturing shows the contrast between α – phase lamellae (dark grey) and β matrix (white), E. Morphology of prior-β grain in Ti6Al4V formed using DED, F. Selective Laser Melting (SLM), G. EBM, H. Transverse section of solidified grain morphologies in DED sample of Ti alloy, I. Longitudinal section of solidified grain morphologies in a DED sample of Ti alloy (283–289). **Note:** depth of the equiaxed grain layer, d_{EG}, penetration melting depth, d_{PM}, and the heat affected zone, HAZ.

In contrast, a high mass deposition rate brings about insufficient melting of the powder and favours the growth of fine, equiaxed prior-β grains. However, there is no grain growth along the region of the fusion line or in the whole heat-affected zone (HAZ) due to the exceptional thermodynamic stability of the coarse prior-β grains. The as-deposited microstructure of DED shows epitaxial growth of columnar β grains via re-melting and re-solidification

process. The thermal gradient in the printed part is generated by convective heat transfer upward into the process gas and conductive heat transfer directed downward through the cooled substrate (290,291). The prior-β grains in the printed part are aligned along the build direction whose boundaries are surrounded by grain boundary α phase, as shown in **Fig. 14A**. The size of α colony is determined by the size of prior β grains developing locally (279).

An optical micrograph of typical EBM Ti6Al4V microstructure is seen in **figure 14B,** whose build direction is directed outside the page. The as-printed microstructure of the EBM sample consists of columnar prior-β grains defined by grain boundary α inside the prior-β grains. A transformed α + β microstructure with the colony and Widmanstatten structure is also observed. It is apparent that prior β grains grow epitaxially through the build layers of the part printed. The lamellar α + β and α-Widmanstatten colonies give poor tensile properties. The microstructure of as-printed Ti6Al4V using SLM (L-PBF) is shown in **Fig. 14C**. *In situ* decomposition of α' martensite transforms into ultra-fine lamellar α + β microstructure (286). The microstructure of the as-built SLM shows a needle-shaped - phase bounded by β-phase interlayers in an elongated β grain (292). Uni-directional, fine α-phase is due to high cooling rates and crystallisation, similar to several studies (200,293,294). The transformation materialises due to progressive thermal cycles along depositions of build layers due to fast cooling rates depicting limited ductility yet high yield strength. Therefore, layer thickness, energy density and laser beam diameter must be controlled accordingly. The α lamellae (dark grey) and β matrix (white) contrast is shown in **Fig. 14D**.

Bands of the layers deposited by the DED process in Ti6Al4V are shown in **Fig. 14E** (295). The layer bands are seen in the AM process due to coarsening of the microstructure in the re-melted regions of preceding layers. Vertical, columnar prior-β grains grow along the build direction, leading to epitaxial growth and directional solidification in SLM, as shown in **Fig. 14F** (296). The microstructure of EBM-printed Ti6Al4V is lamellar, with fine α platelets aligned in various directions, as shown in **Fig. 14G** (288). Some α colonies, i.e., parallel α platelets of the same variant of Burgers relationship are observed. Yet, most α platelets are individual, indicating a relatively faster cooling rate during β → α transformation.

The microstructural distributions along the build direction of WAAM-processed Ti6Al4V having different magnifications are shown in **Fig. 15A, Fig. 15B, Fig. 15C, Fig. 15D, Fig. 15E and Fig 15F**. Under the effect of varying solidification rates, the top region of Ti6Al4V has a basketweave microstructure with acicular α and martensite in the β matrix, as shown in **Fig. 15A**. The lamellar α with basketweave microstructure was produced in the middle

region, as shown in **Fig. 15B**. Widmanstatten microstructure is generated in the bottom region, as shown in **Fig. 15C**. The α phase lamellae have different sizes distributed in the three regions, as shown in **Fig. 15D, Fig. 15E and Fig. 15F**. The width of α plates is broadest in the middle region. The reason for coarse lamellae in the middle region is due to repeated reheating during the WAAM process. Incomplete thermal histories in the top region compared to the previous layers and completed thermal histories due to faster cooling rates in the bottom region results in finer lamellae (297,298).
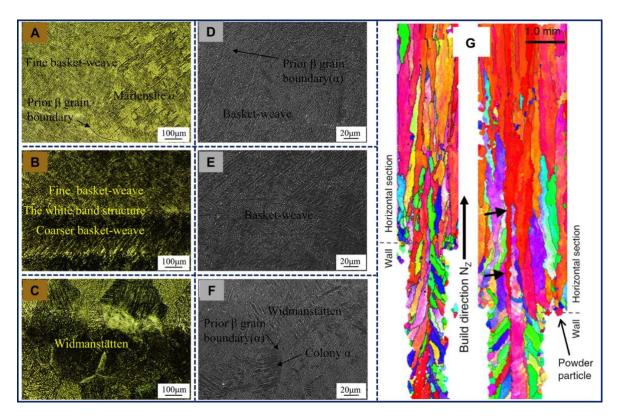
Fig. 15. Microstructural distributions along the build direction in AM process. A. The top region of Wire Arc Additive Manufacturing (WAAM) having low magnification, B. High magnification, C. Middle region of WAAM processed TiAl4V having low magnification, D. High magnification, E. Bottom region (near the substrate) of WAAM processed Ti6Al4V having low magnification, F. High magnification, G. Grain orientation aligned along the build direction in Ti6Al4V processed using SLM (299,300).

The direction of beta grain growth closely aligns <001> build direction in SLM processes with fast scan speed, as shown in **Fig. 15G**. The SLM process creates a smaller melt pool due to a lower laser diameter than WAAM, increasing the cooling rate. Therefore, the SLM process, which has a higher cooling rate than WAAM, thus gives refined beta grains and martensite alpha. Additionally, columnar grains do not align uniformly and grow through the build layers. The microstructure of SLM samples has shorter beta grains with acicular martensite compared to coarse columnar beta grains in WAAM samples.

Columnar β-grain is found to dominate in the microstructures of all AM-manufactured Ti6Al4V (266). The preferential growth direction of β grain is <001>, which has a bcc lattice structure. The <001>$_β$ is parallel to the build direction, and the direction of overall heat flow is said to be perpendicular to the substrate. However, in reality, there is a slight tilt in <001>$_β$ axis, which indicates the complexity in the thermal behaviour of AM process.

2.9.3 Initial microstructure of conventionally manufactured Ti6Al4V

The microstructures of as-cast Ti6Al4V are shown in **Fig. 16A, Fig. 16B and Fig. 16C**, having different magnifications (301). Optical images show the bright α-phase forming Widmanstatten microstructure in the regions between thin and dark β-phase. As seen in **Fig. 16A**, the α-phase is formed along the prior-β grain boundaries. Lamellar structures of α and colonies of lath-β are situated within prior-β grains.

The backscattered SEM image of as-cast Ti6Al4V in **Fig. 16B** shows the contrast in the dark α-phase and bright β-phase at a higher magnification. The grains of as-cast Ti6Al4V are equiaxed, and coarse α/β lamellar colonies are orientated in different directions with transformed β, as shown in **Fig. 16C** (302).

Ti6al4V microstructure manufactured by the wrought process has small, equiaxed grains with blocky plates of α/β phase, as shown in **Fig. 16D**. The initial microstructure of wrought-produced Ti6Al4V is a basketweave pattern that marks the absence of β grain boundaries and α colonies. At the same time, a fine α/β lamellar structure is a characteristic of this microstructure. Ti6Al4V processed by powder metallurgy has a lamellar microstructure. Short, massive α-phase lamellae inside the β-phase matrix is the characteristic microstructure of this process.
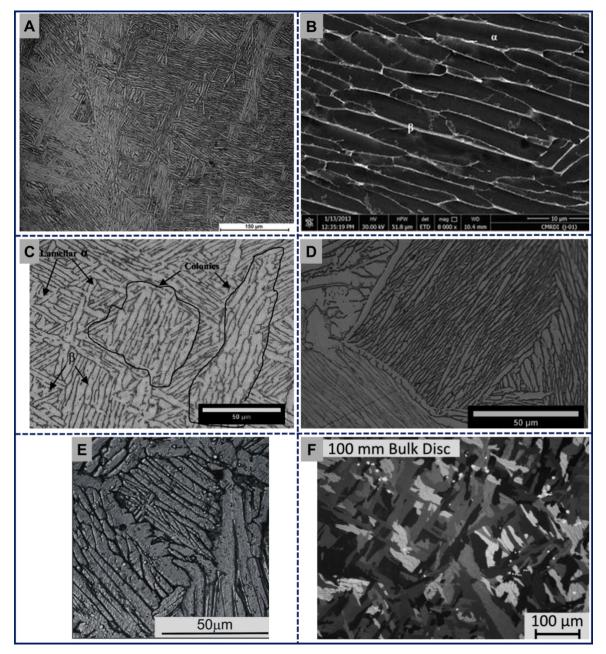
Fig. 16. Microstructure of Ti6Al4V from conventionally manufacturing and FAST process. A. As-cast microstructure of Ti6Al4V (lower magnification), B. Microstructure of as-cast Ti6Al4V (higher magnification), C. Optical images of as-cast Ti6Al4V, D. Optical images of wrought Ti6Al4V, E. Microstructure of Ti6Al4V obtained by powder metallurgical process, F. Microstructure of Ti6Al4V as FAST processed (301–304).

The whole β-phase matrix is surrounded by α-phase precipitations at the primary β grain boundaries, as shown in **Fig. 16E** (304). A typical FAST-processed microstructure for a 100 mm Ti6Al4V disc diameter is shown in **Fig. 16F** (303). Slow cooling rates above β-transus show prior β-grains having α laths in Widmanstatten/colony microstructure with some α-phase also present on grain boundaries.

2.9.4 Microstructure-property correlation

One of the central themes in material science is the microstructure-property correlation. This particular aspect in the case of powder bed fusion processes is of significant importance to material scientists. In order to support the statement, **Fig. 17** illustrates the microstructure development in the SLM process. For reference, **Fig. 17A** shows the working process of the SLM process where different process parameters of importance are also marked. The microstructure developed during the SLM process is uniquely characterised by large columnar grains that grow from the base plate. The columnar grains provide anisotropic properties in SLM printed parts.
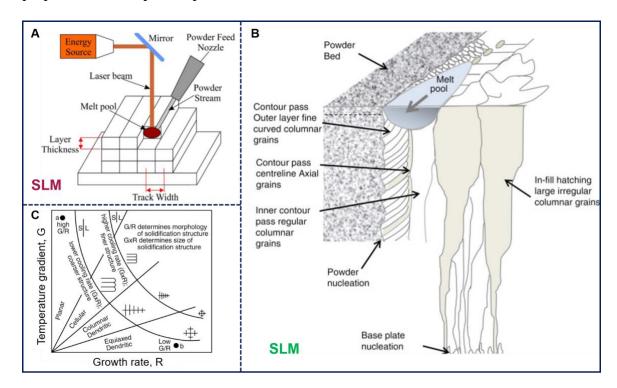
Fig. 17. Laser material interaction involves in situ melting and solidification of metal powders in the melt pool. A. Schematic of working principle in SLM process, and development of different microstructures as a function of temperature gradient and growth rate experienced during solidification process involved in SLM based processing of metallic parts (C), B. Schematic illustration of the distinct microstructures of solidified metals in SLM process where microstructures are characterised by large anisotropic columnar grains, growing from base plate towards the surface of metallic parts and equiaxed grains on the solidified surface (225,305).

Fig. 17B also shows that equiaxed grains are generally formed on the top surface of the materials with different grain morphology like contour-passed centre line axial grains are also observed in SLM printed parts. As far as the fundamentals of the solidification processes

are involved, two key parameters are of significant importance, i.e., temperature gradient G, growth rate, R. Different combinations of G and R are achievable by tailoring the SLM process parameters, which include laser power, laser heat input, and laser scan speed.

Fig. 17C shows that planar solidification front breaks down to cellular, columnar dendritic structure or equiaxed dendritic structure due to the variation of G/R ratio during laser melting and solidification in the SLM route. It is essential to emphasize that both morphology and microstructural length scale are dependants on G/R and G×R parameters. Lower cooling rate or, in other words, low scan speed generates coarser microstructure due to the predominant G×R. In contrast, finer columnar structure develops during high scan speed, i.e., higher value of G×R. Such an understanding of microstructure development is key to establishing a microstructure-property correlation in a laser-based powder-based fusion. Thus, increasing scan speed, powder feed rate, and decreasing laser power reduce G. The G/R ratio is essential, indicating the nucleation rate. If the G/R ratio is greater than one, the nucleation rate is low and vice versa. Therefore, the transition from columnar to equiaxed can be engineered accordingly to meet the requirements(306).

2.9.5   Mechanical properties
2.9.5.1   Tensile strength

The tensile strength of AM parts is dependent on the process parameters and microstructure. Ti6Al4V processed by the laser based AM process had higher tensile strength than wrought alloy with lower ductility, probably due to inherent internal defects and fine microstructure(307). Another study demonstrated increased yield strength and ultimate tensile strength (UTS) with a 0.0124% increase in oxygen and decreased α lath width of the DED part (284). Post-processing treatments like hot isostatic pressing and heat treatments improve ductility with minimal tensile strength (307).

2.9.5.2   Hardness

Microhardness changes along the build direction due to microstructure alteration. It is higher in the first few layers and relatively lowers in the subsequent layers away from the build. This is observed due to higher heat accumulated in the central layers of the deposit (308). Increasing substrate thickness, substrate temperature, and interlayer dwell time was reported to increase the hardness(219). Post-processing treatments like heat treatment or ageing increase hardness rather than varying process parameters (309).

2.9.5.3 Fatigue

Fatigue determines the structural integrity of the AM parts and is governed by microstructure and defects(310). Few groups (311–313) have reviewed the fatigue properties of 3DP parts. Fatigue initiators are fatigue crack growth, fatigue inception sites (pores), and unmelted powder particles (314)(315). These factors are responsible for reducing fatigue life.

Fatigue crack growth generally occurs on a plane, with the crack moving towards the tensile force direction. The crack growth rate was dependant on the location and varied along with distinct directions (316). However, there is still a lack of constancy in the fatigue behaviour. Nevertheless, the behavioural fatigue data is crucial in understanding the fracture tolerance of materials. A need for accurate predictions of fatigue characteristics exists.

2.9.5.4 Residual stress

Residual stresses are generated due to the excessive thermal gradients between the laser source and the neighbouring material of laser based AM. These stresses can potentially distort the AM parts due to cracking. According to previous literature, residual stresses are tensile on the surface and compressive in the centre. Similarly, these stresses are higher between dissimilar materials (317) and at the build-deposit interface. Calculation of residual stress using non-destructive equipment such as X-ray diffraction and neutron diffraction(223) are popular on the macroscale. Consecutively, preheating the material feedstock or post-processing treatments can relieve the residual stresses (318).

2.10 Challenges

As mentioned in the preceding section, additive manufacturing (AM) technology provides the freedom to design patient-specific complex structures. AM technology holds a promising future in fabricating biocompatible implants with desired properties. This section summarizes the key challenges in the AM field concerning different aspects.

2.10.1 Design-complexity and printability challenges

AM based processes give the freedom to control the external and internal architecture of any implant, using CT scan data of the patient. Despite the fact that a range of implant architectures is FDA approved, many of these architectural designs are not yet widely used for patient treatment. Moreover, defining the internal morphology of implants is not yet individually optimised for personalised musculoskeletal treatment. For example, the pore size and shape are not yet standardised for metallic implants to ensure enhanced bone

growth. Such design aspects need to consider the spatial distribution of pores to mimic the complex porous environment of the cancellous bone.

In this context, topological design approaches are to be adapted in future. Topological optimisation and computational lattice designs can be translated to manufacturing a product using 3DP (319–321). Many such design-based structures are required for spinal replacement(115). Patient-specific spinal implants provide mechanical support, void space for bone graft, minimise the surgical time, thereby reducing future complex reconstruction, long-term stability, and enhanced recovery (322),(323). Hip joint implants manufactured using AM techniques can be customised, concerning the shape of bone defects, thereby reducing stress shielding (324). Additionally, porous designs using 3DP promotes bone ingrowth, which contributes to biological fixation (325). Highly porous knee implants imitate the mechanical strength of cancellous bone, thus reducing stress shielding (326). 3D printed and customised implants can provide better knee joint stability, tissue balance and retention function of the knee joint. From such perspectives, AM allows to manufacture better-designed implants for musculoskeletal reconstruction and promoting implant stability (327).

Another challenge is that the implants with patient-specific sizes, like femoral stems, may not be manufactured in SLM/DED route. Scaling coupon samples to large complex components such as porous femoral stem implants in AM are challenging due to limited machine build volume and geometrical limitations. Additionally, size-dependent process parameters, laser scanning strategies, and build substrate vary according to AM process and implant design. Furthermore, batch size and manufacturing throughput concerning process speed and productivity are other scale-up limitations. Distortion, cracking, and residual stresses that are not always apparent in coupon samples can pose thermomechanical complexities in scale-up. In such context, the short stem with reduced dimensions having clinically acceptable dimensional tolerances can be manufactured using Directed Energy Deposition, DED (an AM process) techniques and further tested clinically. However, DED has limitations on resolution and surface finish, requiring further post-processing and surface modification methods.

2.10.2 Process- microstructure-property-related challenges

In the AM of implants, process-microstructure-property and performance of 3D printed parts are not yet extensively investigated due to variations in the printing process, processing parameters and diversity in the alloys. Sustained research and development are necessary to build a knowledge base protocol for biomedically relevant metallic alloys.

Rapid cooling rates in high-temperature AM processes contribute to complex microstructure development in 3DP parts compared to metals from conventional manufacturing methods. An in-depth understanding of the microstructure evolution can help achieve a combination of properties, such as high strength and ductility. A fundamental understanding of microstructural evolution in terms of local temperature gradient, G, and solidification growth rate, R, parameters in AM processes, is essential to understand the mechanical performance of the printed parts. The local temperature gradient, G, and solidification growth rate, R, play an essential role in the resulting mechanical properties and microstructure development. The G/R ratio depends on the metal alloy, AM technique and process conditions such as linear heat input. The wide range of G/R ratios remains a challenge in understanding the solidification structure evolution for printed metals. The influence of anisotropy on product performance under complex loading for textured microstructures produced by the SLM process is not yet understood (328). Surface roughness is directly dependent on cell adherence, and therefore, the guidelines on the correlation between printing parameters to achieve biologically relevant surface roughness are necessary.

In the conext of microstructural development, the typical morphology of different processing induced defects are discussed in this dissertation, in the context of laser-based AM processes. All these defects also limit the strength properties. Based on these observations, it is essential to emphasize that one must use the range of laser power and scan speed to obtain defect-free metallic parts and such combinations vary from metal to metal.

Inherent defects ranging from atomic to macro scales in AM parts affect the printability of the components. In order to avoid such defects, a deep understanding of the mechanisms of nucleation and defect growth profile is necessary. The role of defects affecting fracture and fatigue also remains to be explored for many metallic 3D printed parts. The performance limiting tests for Ti and its alloys are not fully developed, and thus, clinical application of these metal alloys is not fully realised. In reality, the role of porous architecture on mechanical performance using Micro-CT analysis to analyse the morphological changes of a 3D printed implant is not reported in many published reports and needs more attention. Overall, the influence of different design and process parameters on elastic modulus and strength of implantable 3D printed metals need to be investigated for musculoskeletal applications.

2.10.3 Economic challenges

Machine time and post-processing are dominant contributors to the cost of a 3D printed part. Technologically advanced upgrades, high capital, operational costs, safety practice, and

process training often limit the adaption of metal 3D printing for affordable healthcare. The artificial intelligence-based approaches, like machine learning or deep learning, related approaches can be adopted to establish process-microstructure metallic alloys. The adaptation of such approaches may require a significant amount of data, either available in published literature or to be generated in a carefully, planned set of future experiments. Once such models are established, the prediction of primary parameters for large-scale manufacturing can be realised. This can potentially reduce manufacturing costs, as many trial experiments can be avoided.

The market value and growth of 3DP are in their initial stages in the global manufacturing economy. The Food and Drugs Administration (FDA) standards for approving the testing methods (ASTM F 2971, ASTM F 3122, ISO 17296-3), implant designs (ISO 17296-4, ISO/ASTM 52915, ISO/ASTM DIS, 20195 DRAFT), and processing protocols (ISO 17296-2) are slow due to the lack of ability of different AM techniques to manufacture biocompatible, defect-free components that are structurally reliable. Potentially printable alloys have not been clinically tested or are not yet available as a feed material for 3D printing (329).

2.10.4 Biocompatibility related challenges

The biocompatibility of a porous implant material depends on the size and shape of the pores. Since AM is suitable for fabricating patient-specific implants, their clinical application can be better probed by the biocompatibility assessment with living system components (cell, blood, etc.) for musculoskeletal applications. The current literature on in *vivo* studies is available only for limited animal models. To study the biomechanical compatibility of the implant in the human body, cell culture studies under dynamic conditions, as well as dynamic loading response of 3D printed metallic alloys in the physiologically relevant environment, needs to be extensively investigated in future.

2.11 Research Gap

Additive manufacturing provides the freedom to design patient-specific complex structures. This technology holds a promising future in fabricating biocompatible orthopaedic implants with desired properties.

- The lack of a comprehensive database based on the properties of the human bone for different age groups, genders, and demography limits the effective treatment of osteoarthritis. Patent, licensing, trademark and copyright permissions should be well integrated and made more accessible for digitalising products, ideas and frameworks.

61

- Transferring CAD file into 3DP parts often result in certain defects and inaccuracies that were not expected in the CAD design.

- The process-microstructure-property-performance relationship is not yet fully explored due to discrepancies in the printing processes, and multiple process variables. Process optimisation using multiple process variables is a tedious job in experimental studies, causing uncertainty in results.

- Anisotropic behaviour causes differences in microstructure in each 3D printed layer, resulting in different mechanical behaviour in vertical and horizontal directions. Moreover, the void formation between consecutive layers introduces additional porosity and delamination, reducing the material's mechanical performance.

- The environmental impact of the metal feedstock production stage is not well reported for quantitatively comparing different metal manufacturing methods. Life cycle inventory models are rarely discussed for different AM or are currently nonexistent. It is essential as this could provide detail on single-source metrics for appropriate applications. The environmental effects of the post-processing of AM parts to achieve the required geometry and surface topography are often neglected. Powder recycling strategies and recycling end-life manufactured products should be well implemented to reduce the environmental effects of metal manufacturing methods.

- Most articles focus on energy consumed at the manufacturing stage. However, the overall environmental impact assessment should include resource consumption, direct and indirect process emissions, supply chain consequences and waste disposal emissions.

- Manufacturing efficiency in terms of printing time and power consumption should be implemented through part orientation and intelligent product design. Vertical build orientation in AM results in lesser material utilised low cumulative energy demand and low cost per part compared to horizontal and 45° build (235). For example, having a minimal surface area of the support structure in AM and geometric nesting of the product.

- A paradigm shift in design, education and training in digital manufacturing is required to improve the supply chain. If integrated with data science and artificial intelligence, life cycle analysis can target patient specificity and enhance the overall efficiency from feedstock to the supply chain.

3   MATERIALS AND METHODS

This section is divided into two sub-sections involving finite element analysis of two femoral implant designs to understand biomechanical behaviour in peri-prosthetic implant and characterization of AM-manufactured Ti6Al4V using an environmental-friendly 3D printer to understand anisotropy.

3.1   Finite element analysis

The patient's computed tomography (CT) scan data [Siemens (Emotion) (Munich, Germany)] is obtained (ethical approval rights from Sri Sathya Sai Institute for Higher Medical Sciences) in digital imaging and communications in medicine (DICOM) format (120 KV, acquisition matrix: 512×512, number of slices: 809, pixel size: 0.894531 mm, slice thickness: 1.25 mm, Gantry tilt: 0 deg). The patient's femoral stem is modelled based on the CT scan data and is 3D reconstructed using MIMICS (Materialise NV, Leuven, Belgium) software. MIMICS allows reconstructing the medical image data by fragmenting the femoral anatomy. Material properties of the femoral bone were extracted from the voxelwise X-ray attenuation in Hounsfield Units (HU). The range of bone densities was selected based on the 100 cases of scanned data from Chatterjee et al. (161). The patient's femoral model was developed from the CT scan of the patient using the patient's bone density, as discussed in section 3.1.3. Implant dimensions were deduced by eliminating the intra-femoral low-density region using a lower threshold value of 450 Hu (0.623 g/cm^3). Finite Element Modelling was carried out by ANSYS 21 (ANSYS, Inc., Canonsburg, PA). Bonded contact was assumed at the bone-implant interface.

3.1.1   Modelling of the femoral stem

The implant model of Chatterjee et al. (161), designed using CATIA (Dassault Systems, France), similar to "VerSysVR Hip System Fiber Metal Taper" (Zimmer, Warsaw, IN), was used in the analysis. The incorporation of central/internal hollowness within femoral stems to introduce isoelasticity, while maintaining normal external morphology, has shown satisfactory simulation and clinical results for three decades (79,330). Optimization of central hollowness in the femoral stem was studied by Gross and Abel (331). Central hollowness is defined by walls on all four sides and a roof on the top; this design mimics the trabecular and cortical bone and promotes osseointegration. As shown in **Fig. 18A**, the roof thickness of the centrally hollow implant design, 'a' is 4mm, and the material thickness around the cavity 'b' is considered the percentage of anterior-posterior measurement of the proximal-lateral aspect of the femoral implant 'd', (b is taken as 15% of 'd'). Two implant designs, i.e., solid/fully

dense and centrally hollow, were scaled to the patient's anatomy and virtually implanted in the femoral bone cavity (**Fig. 18B**). The centrally hollow design has its dimensions as explained by the thickness of the roof and surrounding four walls, illustrated in **Fig. 18A**.

3.1.2 Construction of FEA models

The FE model was constructed similar to the design of Chatterjee et al. (332). The natural femur (not-implanted) and implanted femur were modelled. The virtual implantation of the implant at the patient's femoral bone is carried out at the Workbench Interface of ANSYS 21. The femoral implant model is superimposed on the natural femur model by scaling as per the patient's anatomy. Virtual osteotomy of the femoral head was carried out, and virtual implantation was performed using Boolean operation (**Fig. 18B**). A mesh independence study was conducted using finer elements ranging from 1.2 mm to 4mm at the proximal region and coarser elements from 2mm to 5mm away from the proximal region. The von Mises stress and maximum principal bone strain I in periprosthetic bone were conducted for different mesh sizes. The final mesh size was chosen when the deviation was less than 1%. Both the models were meshed with a fine mesh size of 1.8mm at the implant-bone interface and 2.7mm away from the bone-implant contact region (**Fig. 18B**). Fine values of element size are essential to obtain more reliable results at the bone-implant interface (owing to its importance in osseointegration). Ten-noded tetrahedron shape was used for meshing as they give accurate results for complex 3D geometry, such as the femoral bone. The final mesh size produced 0.17×10^6 elements in the implant models and 0.1×10^7 elements in the natural femur. Bonded contact was assumed at the bone-implant interface.

In this study, three main assumptions of the model are as follows:

a) According to FE studies conducted earlier, the bone and implant material are isotropic, homogenous and linearly elastic (332–334).

b) Fixed support is considered at the distal end of the femoral bone (**Fig. 18C**).

c) No muscle forces are included in our computational study.

The material properties of the bone, such as Young's modulus (E, MPa), and bone density (ρ, g/cm^3), are assigned element-wise based on Hu (Hounsfield Unit) values as per **Equation 1.** The cortical bone and bone cavity are the two reference points in our study (332,333,335).
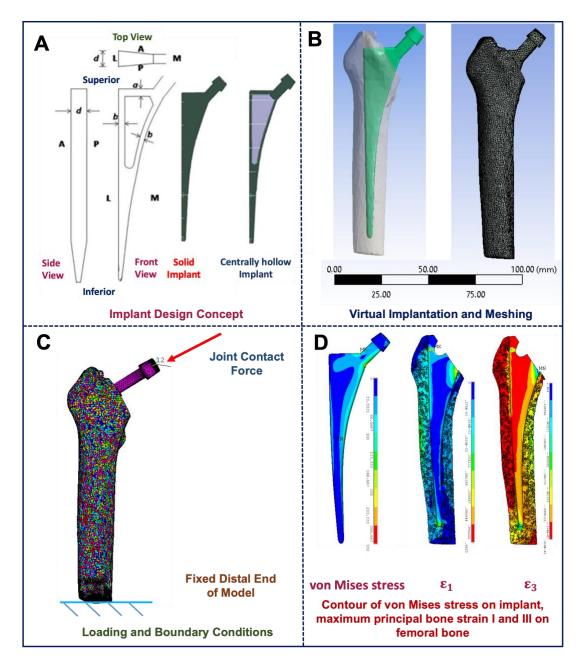
Fig. 18. Schematic illustration of the process involved in FEA analysis of the implanted femur model. A. Diagrammatic representation of the novel design concept showcasing the incorporation of central hollowness in the femoral stem similar to Chatterjee et al. (336). A- anterior, P- posterior, L- lateral, and M- medial. The implant design of a solid and centrally hollow are also shown (161). B. Representational image of virtual implantation of the implant at the patient's femoral bone at ANSYS Workbench is shown. C. The FE model with hip joint loading and fixed boundary conditions are mimicked from the physiological status in a much-simplified form (337). The site of hip joint load application is also shown. The magnitudes of the hip joint load for different body weights in x,y,z directions are tabulated (**Table 4**). D. The contour plots of the distribution of the von Mises stress on the femoral implant, the maximum principal bone strain (ε_1) and maximum principal bone strain (ε_3) of the peri-prosthetic bone.

$$\rho = 0.2389 + (0.0008531) \times \text{Hu}$$

$$E = 6850 \times \rho^{1.49} \tag{1}$$

The implant material is considered Ti6Al4V with $\rho = 4.43$ g/cm^3 and $E = 115$ GPa, and Poisson's ratio 0.3 is entered for all cases. The hip joint loading (shown in **Fig. 18C**) is considered evenly distributed over the abutment of the implant stem that attaches to the femoral head. Normal body weight, 70 kg (686.47 N), is considered according to the loading conditions reported in (337). The natural femur is also analysed using the same loading conditions for comparison. In our study, the hip joint force is assigned to all the nodes at the geometric centre of the femoral head.

3.1.3 Varying bone conditions to check the bone quality

The average bone densities were shown to deviate around 20% from the mean value, as obtained from the 100 cases of Chatterjee et al. (332). The resultant E deviated around 30% from the mean value, similar to Anderson et al. (338). The average bone density value, closest to the mean value of the 100 cases, was considered normal. The subject in our study was a female patient of 52 years from India. Similar to the study of Chatterjee et al.(332), two other bone conditions were modelled individually, considering 20% lower and 20% higher than normal, designated as low and high, respectively. Variation in bone density was implemented by using $0.8\rho_b$ and $1.2\rho_b$ instead of the normal bone density (ρ_b), on the right-hand side of empirical equation 4, correlating ρ and Hu values. The natural femur, solid implant design, centrally hollow design (4mm roof cavity and 15% of the anterior-posterior dimension of the proximal-lateral side of the implant), (**Fig. 18A**) were modelled separately with different bone conditions, keeping constant the subject weight.

3.1.4 Consideration of different body weights

Along with normal body weight, a lower subject weight (50 kg) and higher subject weight (90 kg) have been considered in my FEA analysis. The change in body weight was implemented by proportionally scaling the joint load vectors, as shown in **Table 4** below.

Table 4. Joint loading forces are considered in the finite element analysis for different subject weights. The subject weight of 70 kg has been taken as normal (337).

	Subject Weight = 50Kg			Subject Weight = 70Kg			Subject Weight = 90Kg		
	F_x	F_y	F_z	F_x	F_y	F_z	F_x	F_y	F_z
Hip Joint	-199.6	94.5	-1525.1	-279.6	132.3	-2135.72	-359.4	170	-2745.9

3.1.5 Stress/strain at the proximal-medial region

von Mises stress on the implant and maximum principal strain I (ε_1) and maximum principal strain III (ε_3) within the natural bone and peri-prosthetic bone have been studied in our model. von Mises is a scalar variable which represents the state of stress distribution within an implant (339).
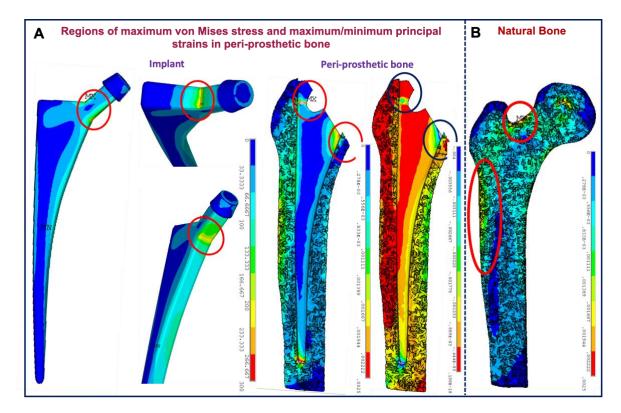
Fig. 19. Areas of von Mises stress and maximum principal strain concentrations (encircled) within the centrally hollow implant and natural/periprosthetic bone, respectively, corresponding to the region of proximal-medial cancellous bone, from where the values are obtained in our study. A. Distribution of von Mises stress on a centrally hollow implant for a 52 year (normal subject weight) female. The lateral side of the implant has the maximum stress concentration. The maximum principal strains (ε_1 and ε_3) on the peri-prosthetic bone for a centrally hollow implant shows that they are primarily located on the anterior side and around the greater trochanter. B. The natural femur is subjected to ε_1 and develops the maximum strain around the greater trochanter and medial side, comparable with the contour of a centrally hollow implant. The values of von Mises stress, ε_1 and ε_3, were obtained by taking the highest value of 25 elements near the encircled region, showing the highest stress/strain concentration (161).

The maximum principal strains and von Mises stress mainly occur in the proximal-medial region in an implant and behind the medial aspect of a natural femur. The variation of the

von Mises stress, ε_1 and ε_3 was studied for different implant designs, concerning different body weights and bone conditions.

The values of stress, ε_1 and ε_3, were obtained by selecting the highest value of the 25 elements from the maximum stress/strain concentration for the peri-prosthetic bone (**Fig. 19A).** For the case of the natural bone, the values of von Mises stress was located behind the medial aspect. The implanted femur was divided into two Gruen zones, anterior and posterior, for FEA evaluation. The nodal solution was generated in each zone. The regions containing the maximum principal strain regions were comparable with the corresponding regions in the natural femur.

3.2 Metallographic sample preparation

The Ti6Al4V powders for SLM (spherical, 15-45 µm) were supplied by Tekna Plasma Systems Inc. (Canada). The SLM-built Ti6Al4V coupons for microstructural and property characterisation were manufactured using an Aconity mini L-PBF machine from Aconity GmbH (Herzogenrath, Germany), which is equipped with a redPower QUBE single-mode fibre laser from SPI Lasers Ltd. (Southampton, United Kingdom) with a maximum beam power of 1 kW and a processing wavelength of 1070 nm. The minimum laser beam diameter on the build platform is 70 μm. Since titanium has a strong oxygen affinity and interstitial oxygen acts as α-stabilizer in titanium, the oxygen content in the processing gas (Argon) was kept below 100 ppm for the whole duration of the build job. The printing parameters for the samples included a laser power of 190W, a laser scan speed of 316.67 mm/s, hatch spacing of 0.12 mm, a layer thickness of 0.03 mm and a laser beam diameter of 0.13 mm.

The as-built Ti6Al4V coupons manufactured by SLM were cut into 7mm×5mm specimens using a cutting machine (Struers, Discotom-6, Ballerup, Denmark). The cut samples for metallographic examination were mounted in bakelite (30 mm diameter) using 20 kN force for 7 minutes at 180°C using a mounting press (Struers Labopress-3, Ballerup, Denmark). Grinding and polishing of the mounted specimens using standard procedures employing silicon carbide abrasive papers from 180, 320, 600, 800, 1200, 2500, and 4000 grit sizes using Struers TegraPol-31 polisher-grinder machine. The final polish having a mirror-like finish, was given with 0.25 µm colloidal silica suspension (OPS) and 5% w/v hydrogen peroxide (H_2O_2) solution. The polished sample was then carefully cut off from the bakelite mould using a workshop vice.

Scanning electron microscope (SEM) imaging was conducted on an FEI Quanta 250 FEG-SEM + Gatan 3view using an accelerating voltage of 10 kV and a working distance of 10

mm. Back-scattered (BSE) SEM images were captured for microstructure evolution as a function of build directions in three different regions of the specimen, i.e., bottom region (near the substrate), middle region and top region.
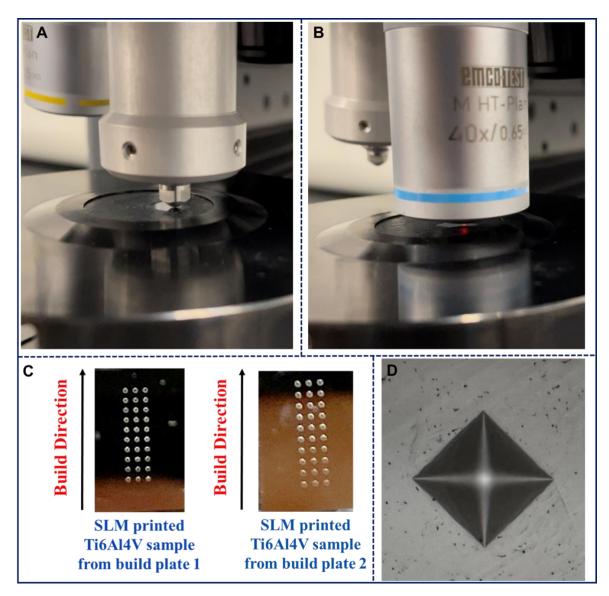
Fig. 20. Vickers microhardness test of SLM-built Ti6Al4V samples. A. Auto hardness tester (Struers Durascan 80) showing the indent on the sample, B. 40x objective lens to analyse the indent, C. Images displaying the indentation for the samples along the build direction for two different build plates, D. Image captured by objective lens showing the indentation.

Vickers microhardness test was performed for grinded and polished SLM-built Ti6Al4V along the build direction using Auto Hardness Tester (Struers Durascan 80) using a load of 1 kgf and dwell time of 15 seconds, as shown in **Fig. 20A**. Vickers hardness test involves pressing a diamond having a square base pyramid making an angle of 136° between the opposite faces at the apex. Indentations were in both radial and axial directions with 1mm spacing between indentations. The first indentation at the bottom region (closest to the substrate) was 3mm from the substrate to avoid indentations hitting outside the sample. The

material's hardness was tested at 10 points along the build direction, having three rows, as shown in **Fig. 20C**. The indents were analysed using a 40x objective lens (as shown in **Fig. 20B**) to produce a micro-hardness map.
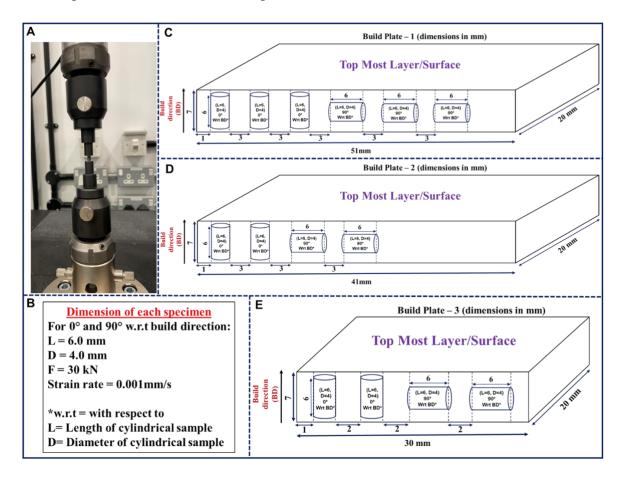
Fig. 21. Compression testing of SLM built Ti6Al4V. A. Universal testing machine (UTM) Instron, USA with Ti6Al4V cylindrical sample, B. Dimensions, maximum force and strain rate for compression testing of 0° and 90° specimens, C. Sketch of EDM cut for Ti6Al4V build plate 1, D. Build plate 2, E. Build plate 3.

The anisotropic mechanical properties of SLM-built Ti6Al4V were determined using Universal Testing Machine (UTM) Instron (USA), as shown in **Fig. 21A**. The samples for compression testing were cut from the build plates by EDM Precision Technologies, Towcester according to the dimensions stated in **Fig. 21B**. Cylindrical disks measuring 6mm in length and 4 mm in diameter from three different SLM-built Ti6Al4V coupons (having same printing parameters, i.e., n=3) in parallel and perpendicular to the build direction were used for the test, as shown in **Fig. 21C, Fig. 21D and Fig. 21E**. Uniaxial compression tests were conducted with a maximum cell load of 30kN and a constant strain rate of 0.001 mm/s at room temperature. The tests were stopped when the maximum force available was reached. Machine compliance was dealt with using machine software called Bluehill before the start of the compression tests as per standard machine protocol.

Electron backscattered diffraction (EBSD) analysis was performed for grinded and polished SLM-built Ti6Al4V along the build direction on a scanning electron microscope (SEM) Thermofisher Apreo with OI symmetry EBSD detector. The EBSD parameters included a working distance of 20mm for scanning a 6×7 mm^2 area of Ti6Al4V. The operating conditions were as follows: accelerating voltage of 20kV and current of 26nA. A step size of 5 µm was used for data collection and the texture was processed using MTEX.

4   RESULTS AND DISCUSSION

4.1   Biomechanical response of solid and centrally hollow femoral stem design

In this sub-section, the biomechanical response of the two implant designs will be described. The virtual implantation caused noticeable changes in the strain distribution profile in the peri-prosthetic bone. Considerable strain depletion of the bone in the anterior region was observed near the proximal anterior-lateral, proximal anterior-medial side and greater trochanter in the case of a natural femur. However, the maximum strain was observed in an implanted bone's anterior side of the lateral and medial regions (**Fig. 22A**). Since the implant is stiffer than the bone, it presses the bone at a distal point, post which it does not participate in the load-bearing of the bone. This phenomenon produces various stress/strain distributions over the peri-prosthetic bone at the implant interface.

Fig. 22A and Fig. 22B show von Mises stress's effect on a solid and centrally hollow implant by varying subject weight and bone density. It is seen that a hollow implant design has more von Mises stress compared to a solid design, and the implant material does not undergo plastic yield. It is also seen that the von Mises stress on both the implant designs increases with an increase in the subject weight (as the applied joint forces increase, **Fig. 22A**) and remains constant with an increase in qualitative bone density (as the applied joint forces are the same for all bone densities), as seen in **Fig. 22B**.

Fig. 22C, Fig. 22D, Fig. 22E, and Fig. 22F compare the effect of ε_1 and ε_3 on peri-prosthetic bone by varying subject weight and bone density in the anterior and posterior regions for a solid implant, centrally hollow implant and natural femoral bone. The maximum principal strain values increase in the peri-prosthetic bone for a centrally hollow implant (reduced stiffness) as compared to a solid implant. Moreover, the bone strain values in a centrally hollow implant design are closer to the natural femoral bone. It is also seen that the bone strain values are higher for a low bone density (**Fig. 22D and Fig. 22F**). However, the implant's von Mises stress is higher for a higher bone density, as anticipated, and the same is comparable with the stress environment of the natural bone (**Fig. 22A and Fig. 22B**).
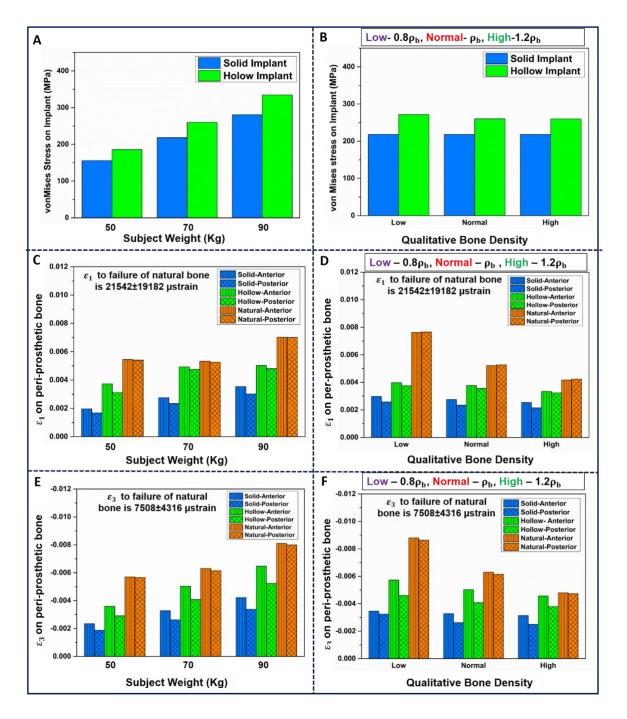
Fig. 22. Variation of von Mises stress on the implant, maximum principal strains on the peri-prosthetic bone concerning solid and hollow implant, considering different subject weights (50, 70, and 90 Kg), bone conditions and Gruen zones. A. Effect of von Mises stress on implant design by varying subject weight and keeping bone density (ρ_b) constant. B. Effect of von Mises stress on implant design by varying bone density and keeping subject weight constant. Comparison of the effect of ε_1 and ε_3 on peri-prosthetic bone, by varying subject weight and qualitative bone density in the anterior and posterior regions for a solid implant, centrally hollow implant and the natural femoral bone (C, D, E, F).

Higher values of maximum principal strains (ε_1 and ε_3) for peri-prosthetic bone are observed with a centrally hollow implant design than a solid implant design, thus, mimicking the strain environment within a natural femoral bone. A low bone density shows a more significant decrease in maximum principal strains (ε_1 and ε_3) on the peri-prosthetic bone for a centrally hollow implant than a solid implant. By now, we know that a hollow design shows a higher bone strain. Thus, our choice of implant design is a centrally hollow design. For a normal subject weight (70 kg), a centrally hollow stem design is a better choice of implant for all bone conditions. For higher bone density, the difference between the peri-prosthetic bone strains of centrally hollow design and natural femur are nearly similar, resulting in lower deviation of bone strain due to implantation. The implant's stress is more applicable for high bone density, and peri-prosthetic bone strain is more appropriate for low bone density.

The biomechanical significance of the optimizing parameters to customise implant design and femoral stem stiffness has been studied. Introducing central hollowness in the femoral stem reduces the implant stiffness, thereby simulating the mechanical environment in the peri-prosthetic bone compared to natural bone. This phenomenon reduces bone loss due to stress shielding. Central hollowness was incorporated through an internal hollow cavity in the stem, according to Chatterjee et al. (336). A solid implant was considered for comparison of the biomechanical response. The optimizing parameters included three subject weights, i.e., 50 Kg, 70 Kg, and 90 Kg and three bone conditions, i.e., low ($0.8\rho_b$, ρ_b, $1.2\ \rho_b$). The natural situation has also been modelled for understanding the differences in the biomechanical environment.

Low bone densities have more bone strain than higher bone densities due to their compressive nature. The values of peri-prosthetic bone strain are higher in the centrally hollow implant than in natural bone due to implant stiffness. The bone strain reduces as the bone density increases; thus, centrally hollow implants and higher bone densities show minimal deviation from natural bone conditions.

The proximal part of the stem is held within the cancellous bone, and the distal part is extended within the bone cavity. The peri-prosthetic cancellous bone is compressible, and the cortical outer is stiffer, especially for higher bone densities. The cortical bone bears more load from the implant through the cortical contact areas, leaving the distal implant with minimal load. Thus, the incorporation of central hollowness in implant design showed a reduction in the stiffness of implant material in the proximal region, allowing the implant to flex more, and have a higher final fracture strength. In consequence, the proximal portion of the implant is subjected to higher stress.

Some of the limitations of the study are:

a) Instead of considering different patients (subjects) with such attributes, different body weights and bone conditions for the same patient are taken.

b) The model has not reproduced the exact complex physiological loading from the muscles and the boundary conditions.

c) Stress/strain developed because of implantation has been ignored.

d) Frictional contact is not considered.

e) The femoral implant should be divided into more Gruen zones to give better nodal solutions and prosthetic prediction.

The presurgical bone condition has been considered in this model while using an implant design customised to the patient's anatomy. The effectiveness of incorporating internal hollowness in the implant design on biomechanical stability is demonstrated in the ability to vary implant stiffness (Young's modulus) while keeping the external shape intact. This shows flexibility and convenience during surgical procedures.

4.2 Laser Additively Manufactured Ti6Al4V Characterisation

4.2.1 As-built microstructure of Ti6Al4V by SLM

The directional solidification and rapid cooling after melting result in the non-equilibrium hierarchical microstructure of SLM-built Ti6Al4V. Samples show visible defects such as porosity and lack of fusion defects. The as-built microstructure consists of columnar β grains with a few fine acicular α' martensite variants. SEM BSE detector struggled to detect atomic contrast in the microstructure, which suggests the material transformed from the beta with little/no diffusion i.e., as a martensitic transformation. The width of prior β grains in the middle region is smaller than at the bottom and top regions. Epitaxial growth of prior β-grains is along the build direction and opposite to the cooling direction.
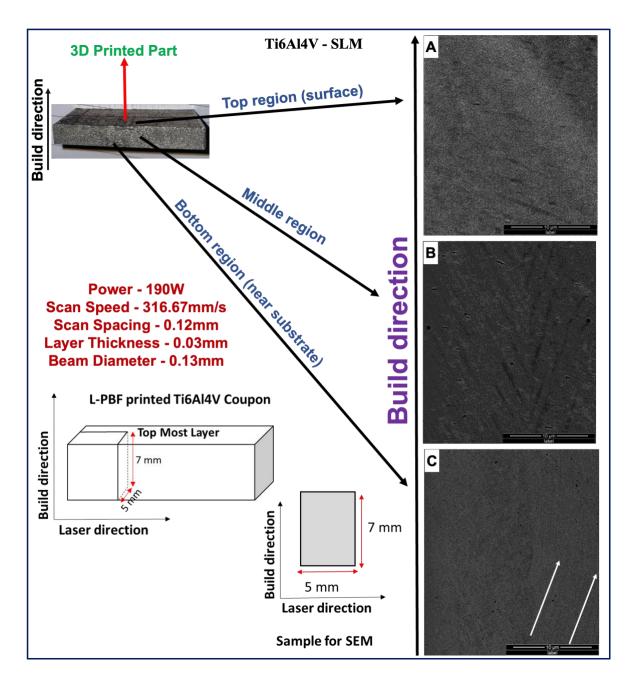
Fig. 23. BSE SEM images of SLM built Ti6Al4V as a function of build direction. A. The top region, B. Middle region, and C. Bottom region of the sample.

The SLM process has high cooling rates which result in the transformation of β to martensite α'. Porosity development in L-PBF-built Ti6Al4V samples was dependent on the sample's location in the build direction. The porosity of samples in the middle was twice as high as those on the edge of the 3d printed part. Moreover, non-spherical pores were dominant along the laser scan direction compared to the build direction.

4.2.2 Microhardness

The Vickers microhardness map of SLM-built Ti6Al4V as a function of the build direction is shown in **Fig. 24.**
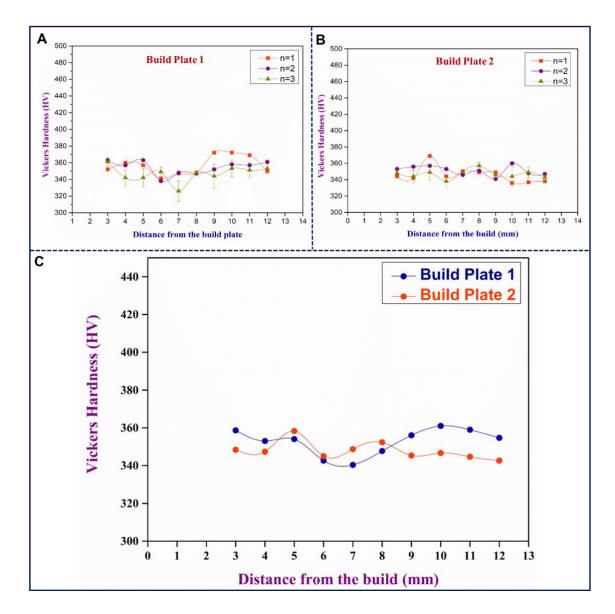
Fig. 24. Vickers microhardness map for SLM built Ti6Al4V sample as a function of its build direction. A. Vickers microhardness map for Ti6Al4V build plate 1, B. Vickers microhardness map for Ti6Al4V build plate 2, C. Average Vickers microhardness map for Ti6Al4V build plate 1 and 2.

The microhardness for build plate 1 and build plate 2 is fairly consistent, with a standard deviation of ±(5-10) HV. The Vickers microhardness for both the build plates is in the range of 320-380 HV, similar to the expected results reported in the literature. However, there is a dip in microhardness values in SLM-built Ti6Al4V at 6-7 mm from the substrate in the middle region, and this could be due to the smaller width of prior β-grains in the middle region. Therefore, finer α' can lead to superior microhardness.

4.2.3 Mechanical Properties

The uniaxial compression of SLM-printed Ti6Al4V for samples 0° and 90° to the build direction from three different build plates (refer to **Fig. 21**) having the same processing parameters are plotted in **Fig. 25**.
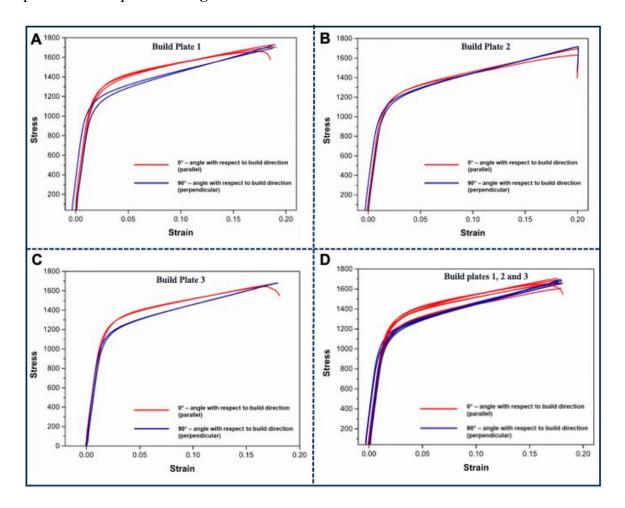
Fig. 25. Uniaxial compressive stress-strain curve for SLM-built Ti6Al4V at 0° and 90° to the build direction from three different build plates (n=3) with the same printing parameters (as depicted in figure 21), i.e., build plate 1 (A), build plate 2 (B), build plate 3 (C), and all build plates in a single plot (D). All values of stress are in MPa and strain in %.

The uniaxial compressive stress-strain curves for build plates 1, 2 and 3 have large differences (>1000 MPa) in their yield strength values for 0° and 90° orientation correspondingly, as plotted in **Fig. 25A, Fig. 25B and Fig. 25C**, suggesting a low level of accuracy in repeatability of 3d printed Ti6Al4V parts. The 0° samples from all the build plates had higher yield strength compared to their corresponding 90° samples (**Fig. 25D**), in accordance with other studies in the literature, indicating the anisotropic behaviour of SLM-built Ti6Al4V (340–342). However, elastic modulus does not vary with the build orientation. In other words, the orientation of prior β-grains does not significantly affect elastic modulus.

4.2.4 Texture analysis

The EBSD colour maps are depicted along different directions, i.e., laser scan direction and build direction as shown in **Fig. 26A and Fig. 26B** respectively.
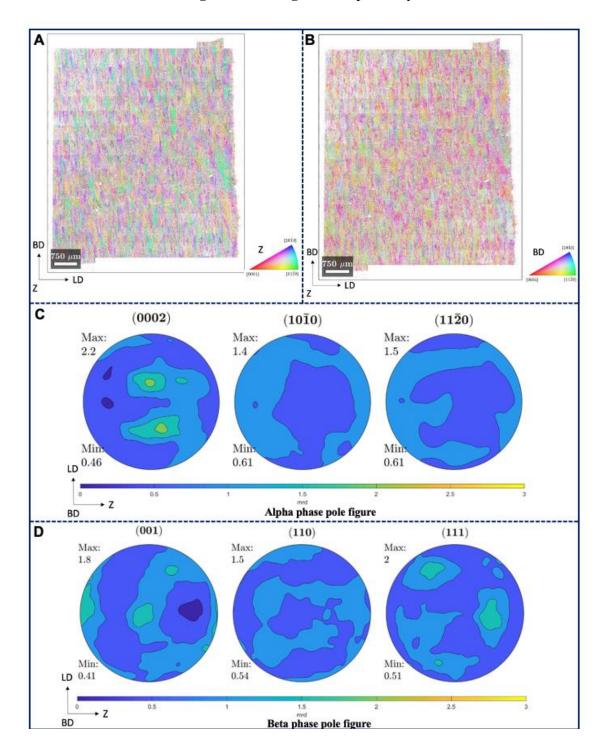
Fig. 26. EBSD maps and pole figures for alpha and beta phase coloured in different directions for Ti6Al4V. A. EBSD map coloured in the laser scan direction and B. build direction, C. Pole figures depicting reconstructed α textures and, (D) β for Ti6Al4V by L-PBF.

They indicate which crystal direction is parallel to the reference direction for each point in the map. The pole figures (**Fig. 26C and Fig. 26D**) show the overall distribution of crystal directions for the whole map. The centre of the pole figure is the build direction (BD), and the top being the laser scan direction (LD) and transverse direction (Z).

The crystallographic orientations of various martensite (α′) structures in L-PBF manufactured Ti6Al4V indicate the weak texture of α′ due to the large volume of variants within columnar β grains, in accordance with a published study (343) The deviation in the texture strength can be attributed to a lower temperature gradient, affecting the cooling rate in L-PBF. The β texture reconstructed from the alpha using the burgers relationship shows the epitaxial growth of β grains along several deposited layers. Course columnar grain structure is observed along the build direction, depicted in **Fig. 26B**. Corresponding contour pole figure (**Fig. 26D**) indicates dominant {1 0 0} texture along the direction of grain growth that develops due to preferential growth direction {1 0 0} during solidification. However, measuring such fine beta in a microstructure with EBSD isn't particularly reliable.

5   DISCUSSION

The as-built microstructure of SLM-printed Ti6Al4V is columnar β grains with a few fine acicular α' martensite variants. A large number of α' plates formed in the inner part of the coarse prior β grains. Due to rapid cooling, the typical grain morphology in SLM-printed parts is directional columnar dendrite, leading to anisotropy in the mechanical properties. Anisotropy can be reduced with an equiaxed grain structure or a mix of equiaxed and columnar grains. Fine equiaxed grains can enhance ductility and fracture toughness. The 3d printing parameters have a significant effect on the microstructure of Ti6Al4V. As the laser power increases, the grain size proportionately grows due to the high energy-induced coarsening effect. The grain size was reduced with increased scan speed due to short exposure time and rapid solidification (344). The mechanical properties of Ti6Al4V are sensitive to cooling rates (226). The martensite gives poor ductility and tensile properties and depends on parameters such as energy density, layer thickness and defocus of the laser beam (345). Post-processing treatments usually transform α' to α phase, providing better mechanical properties

The formation of pores in SLM is inevitable and is attributed to liquid-solid phase transformation. AM defects, mainly porosity has a direct impact on mechanical properties. Galarraga et al (346) reported that internal porosity was dependent on the sample's location in the build plate. The porosity in the middle of the build plate was twice as much as those in the edges. This is in synchronisation with results reported under **section 4.2.1.** Rapid laser

scan speed minimises the melt pool size, thereby increasing the susceptibility of lack of fusion porosity (347). Contrarily, raising laser power increases melt pool size, thereby reducing porosity (348). For load-bearing orthopaedic applications, the implant requires smaller pores for proliferation and differentiation to form tissue around the prosthesis. Therefore, tissue vascularization requires large pores for mass transport. These paradoxes suggest that irregular porous structures having changeable porosities and pore size may always meet bone healing requirements (349).

The microhardness of two build plates with the same printing parameters was tested. The microhardness of the SLM printed samples exhibited excellent values ranging from 320-380 Hv, mainly attributed to fine acicular martensites that strengthen Ti6Al4V. The uniaxial compression of SLM-printed Ti6Al4V for samples 0° and 90° to the build direction from three different build plates processed under the same printing parameters was studied. The anisotropy can be seen from the stress-strain curves. Titanium is harder along the (0002) direction, so when loading the samples along the direction where the (0002) poles are aligned, the texture is stronger. It is further inferred that the difference in compressive strength can be due to the dimensional change of acicular martensite (350).

Several studies have published that anisotropy is attributed to internal defects and crystallographic texture due to different thermal histories (351–354). Anisotropy in compression is attributed to large, closed pores in samples loaded parallel and perpendicular to the build direction. This is consistent with results published in the literature. Ti6Al4V crystallographic texture has a dominant $< 0\ 0\ 1 >_\beta$ along the build direction, and this strong texture affects anisotropic properties (355). The martensite phase formed during cooling exhibits random texture, indicating a weak texture in SLM-fabricated Ti6Al4V (356,357). Texture can be controlled through scanning speed and layer thickness, as these parameters decide the extent of remelting of previously deposited tracks. High laser power, smaller spot size and layer thickness would give strong texture and morphology (358–360).

Experimental studies for Ti6Al4V using Aconity Mini were carried out to compare its feasibility with other printers (in literature) for 3d printing patient-specific implants for orthopaedics. The Aconity Mini (3D printer used in my experimental characterization) is very new in the market and is particularly designed for the production of relatively small components. A lot of the work with the Aconity systems is focused on aerospace applications. Biomaterials in metal powder additive manufacturing is a relatively new emerging form of manufacturing for musculoskeletal applications in Aconity Mini.

The build chamber is designed so that there is as little wastage of powder as possible, as most of it can be reclaimed by sweeping it into the overflow canister. It is also much smaller (in terms of build volume) and designed to be dismantled very quickly and easily with only hex keys and socket tools. This is also different to a system that is designed for industrial settings, such as EOS or Renishaw 3d printing machines. Industrial machines are much larger and are designed to be run for weeks if not months between cleaning sessions as material changes are rare in order to ensure maximum efficiency of batch/mass production of components. Parts printed with EOS and Renishaw showed stable performance and microstructure over Aconity Mini, owing to their large build volume (361). Critical observation in parts printed with EOS and Aconity Mini indicated that there is a clear variation in part density despite similar microstructure (361). Reduced porosity and improved elongation were reported in the former.

The small build chamber size and the arrangement of the inert gas supply and circulation have a significant impact on the cooling rate. The small height of the build chamber and the gas flow velocity affect the cooling rate and solidification time in Aconity mini. Thus, the thermal residual stresses and mechanical properties are affected, giving rise to defects such as porosity, a site for crack initiation. Owing to the small build chamber size, the removal of rising fumes and metal vapour from the melt pool area is quite challenging and therefore leads to fluctuation in measured values and microstructure.

Furthermore, the Aconity Mini is capable of doing builds with extremely small amounts of powder, with an option to reduce the size of the build chamber by up to 80%, making it one of the smallest L-PBF printers (by build volume) on the market. This flexibility makes it ideal for the rapid prototyping of novel materials, as samples can be produced with far less feedstock than would be required for other machines.

6 CONCLUSION

Hip osteoporosis and osteoarthritis are major public healthcare problems among elderly patients across different demography. With the advent of MRI/CT scan data, the patient's osseous structure can be reconstructed to perform patient-specific orthopaedic surgeries. The recent innovation in additive manufacturing technologies has made improvements to address the growing demands of patient-specificity. Altered gait kinetics and kinematics in patients with hip OA are of clinical relevance, as it gives insights into the effect of hip OA on pathomechanics and joint loading. Information on hip kinematics and kinetics are essential

in designing a femoral stem implant and the advancement of enhanced rehabilitation strategies.

Designing implants while mimicking the topology and modulus of the natural osseous system is necessary for bridging the gap between scientific and translational research. It has become evident that different implant designs are adequate for appropriate hip OA patient groups. Although, short stem designs are appealing; stem subsidence, malalignment, intraoperative fractures and lack of long-term data are concerning. Therefore, clinical outcomes of novel implant design are not always suitable for existing implants. Sometimes, innovation leads to unforeseen clinical challenges such as early implant failure (such as the DePuy ASR hip implant).

Metal AM processes are energy-intensive compared to CM unless material utilisation, topological optimisation, powder feedstock recycling, build orientation, and reduced manufacturing scraps are implemented. In general, AM is a sustainable option that involves complex geometries and low-part quantities (e.g., patient-specific applications), such as hip implants.

Contrary to conventional implant manufacturing, AM increases implant performance, offers higher accuracy at a lower cost, manufactures implants in less time with better specifications, and produces parts with improved dimensional stability and near-net shapes. Inherent defects such as gas porosity, lack of fusion voids, distortion, and residual stresses affect AM part and quality. It is recommended that controlling mechanical properties by varying process parameters and understanding microstructure evolution will help tailor the properties and performance of 3D-printed parts. Sustained research and development of 3D printing processes and understanding the process-structure-property (PSP) linkages are essential for wider clinical adaptation of metal AM techniques.

Carrying out clinical studies with material, design and manufacturing along with surgical-patient parameters makes the cost and time for developing implants unrealistic. To address those challenges and research gaps, long-term clinical outcomes can be predicted by more efficient and less expensive numerical approaches, such as biomechanical modelling and finite element analysis.

One of the critical outcomes of the simulation study in my thesis is that the central hollowness in the femoral stem design can be changed according to the bone condition and subject weight to prevent implant loosening. Introducing central hollowness within the

femoral stem design compared to solid design achieves reduced implant stiffness and a closer maximum principal strain profile to natural bone.

Experimental characterization of Ti6Al4V was carried out using a cost-effective and environmentally-friendly 3d printer to compare its feasibility with industrial 3d printers and understand anisotropic mechanical properties. The effect of anisotropy on microstructure, microhardness, compressive strength and texture has been understood. The results are compared to previous literature and the ways to control anisotropy through various printing parameters have been explained. Aconity Mini ensures maximum efficiency yet reduced part density and porosity developments are concerning. Process parameter optimisation according to the printing machine as well as inert gas circulation makes Aconity Mini an ideal, environmentally conscious machine for the rapid prototyping of novel materials, as samples can be produced with far less feedstock than would be required for other machines. The growing knowledge base is essential for designing a process protocol to produce defect-free, metallic alloys for musculoskeletal applications. Research gaps and challenges imposed by AM in load-bearing implants can be bridged only with well-coordinated research programs among different disciplines, including manufacturing, materials, and biological and medical science.

7 FUTURE WORK

The most commonly used material for orthopaedic implants is Ti6Al4V, manufactured using SLM. However, stress shielding and stress concentration concerns remain, leading to bone degradation and implant loosening. Moreover, the release of Al and V ions during dissolution of the alloy is toxic, limiting the long term applications of Ti6Al4V. For short term applications, Ti6Al4V can be printed with different printing parameters to control porosity and to randamise the texture even further. The addition of non-toxic Ta to Ti enhances the strength and lowers the modulus of the Ti-Ta alloy. In contrast, the high density of Ta (4 times > Ti) and high melting point (3016K) make it difficult to fabricate this alloy (362). To overcome manufacturing challenges, functional grading of Ti-Ta alloy through in-situ alloying by varying the Ta content in the alloy to obtain favourable mechanical properties and cytocompatibility (maximum Ta content in the alloy at the outer surface and minimum Ta content in the alloy at the core) can be adopted. Functionally graded compositions can result in the lowest achievable elastic modulus, thereby showing potential as a promising metal alloy for musculoskeletal applications.

BIBLIOGRAPHY

1. Basu S, Johl R, Pacelli S, Gehrke S, Paul A. Fabricating tough interpenetrating network cryogels with DNA as the primary network for biomedical applications. ACS Macro Lett. 2020 Sep 15;9(9):1230–6.

2. Dubey, Ashutosh K, Amartya Mukhopadhyay BB. Interdisciplinary Engineering Sciences: Concepts and Applications to Materials Science. CRC Press; 2020.

3. Ni J, Ling H, Zhang S, Wang Z, Peng Z, Benyshek C, et al. Three-dimensional printing of metals for biomedical applications. Mater Today Bio. 2019;3(May).

4. Basu B. Biomaterials Science and Tissue Engineering: Principles and Methods [Internet]. Cambridge University Press; 2017. 716 p. Available from: https://www.cambridge.org/in/academic/subjects/engineering/biomedical-engineering/biomaterials-science-and-tissue-engineering-principles-and-methods?format=HB

5. Lowther M, Louth S, Davey A, Hussain A, Ginestra P, Carter L, et al. Clinical , industrial , and research perspectives on powder bed fusion additively manufactured metal implants. Addit Manuf. 2019;28(June):565–84.

6. Shah FA, Thomsen P, Palmquist A. Osseointegration and current interpretations of the bone-implant interface. Acta Biomater. 2019;84:1–15.

7. Palmquist A, Snis A, Emanuelsson L, Browne M, Thomsen P. Long-term biocompatibility and osseointegration of electron beam melted , free-form – fabricated solid and porous titanium alloy : Experimental studies in sheep. 2011;27(8):1003–16.

8. Nagakura R, Yamamoto M, Jeong J, Hinata N, Katori Y, Chang WJ, et al. Switching of Sox9 expression during musculoskeletal system development. Sci Rep. 2020;10(1):1–12.

9. Zaghloul A. Hip Joint: Embryology, Anatomy and Biomechanics. Biomed J Sci Tech Res. 2018;12(3):9304–18.

10. Juneja P, Munjal A, Hubbard JB. Anatomy, Joints. StatPearls Publishing, Treasure Island (FL); 2020.

11. Byrne DP, Mulhall KJ, Baker JF. Anatomy & Biomechanics of the Hip. 2010;51–7.

12. Sato T, Sato N. Clinical relevance of the hip joint: Part I– Review of the anatomy of the hip joint. Int Musculoskelet Med. 2015;37(4):141–5.

13. Crowninshield RD. Use of Optimization Techniques to Predict Muscle Forces. J Biomech Eng. 1978;100(2):88–92.

14. Bergmann G, Deuretzbacher G, Heller M, Graichen F, Rohlmann A. Hip contact forces and gait patterns from routine activities. 2001;34:859–71.

15. Sato T, Sato N. Clinical relevance of the hip joint: Part II–Importance of joint distraction. Int Musculoskelet Med. 2016;38(1):11–6.

16. Rho JY, Zioupos P, Currey JD, Pharr GM. Microstructural elasticity and regional heterogeneity in human femoral bone of various ages examined by nano-indentation. J Biomech. 2002;35(2):189–98.

17. Keaveny TM, Morgan EF, Niebur GL, Yeh OC. Biomechanics of trabecular bone. Annu Rev Biomed Eng. 2001;3:307–33.

18. Wehrli FW, Song HK, Saha PK, Wright AC. Quantitative MRI for the assessment of bone structure and function. NMR Biomed. 2006;19(7):731–64.

19. Cole JH, van der Meulen MCH. Whole Bone Mechanics and Bone Quality. Clin Orthop Relat Res. 2011;469(8).

20. Wegst UGK, Bai H, Saiz E, Tomsia AP, Ritchie RO. Bioinspired structural materials. 2015;14(October 2014):23–36.

21. Choi K, Kuhn JL, Ciarelli MJ, Goldstein SA. The elastic moduli of human subchondral, trabecular, and cortical bone tissue and the size-dependency of cortical bone modulus. J Biomech. 1990;23(11):1103–13.

22. Wang D, Wang Y, Wu S, Lin H, Yang Y, Fan S, et al. Customized a Ti6Al4V Bone Plate for Complex Pelvic Fracture by Selective Laser Melting. Materials (Basel). 2017 Jan 4;10(1):35.

23. Petersilge CA. MR arthrography for evaluation of the acetabular labrum. 2001;423–30.

24. Keene GS, Villar RN. Arthroscopic anatomy of the hip: An in vivo study. Arthroscopy: The Journal of Arthroscopic & Related Surgery. 1994;10(4):392–9.

25. Czerny C, Hofmann S, Urban M, Tschauner C, Neuhold A, Pretterklieber M, et al. MR arthrography of the adult acetabular capsular-labral complex: correlation with surgery and anatomy. American Journal of Roentgenology. 1999 Aug 1;173(2):345–9.

26. Cotten A, Boutry N, Demondion X, Paret C, Dewatre F, Liesse A, et al. Acetabular Labrum: MRI in Asymptomatic Volunteers. J Comput Assist Tomogr. 1998;22(1).

27. Lage LA, Patel J V, Villar RN. The acetabular labral tear: An arthroscopic classification. Arthroscopy. 1996 Jun 1;12(3):269–72.

28. Blankenbaker DG, Tuite MJ. The painful hip : new concepts. 2006;352–70.

29. Ranawat AS, Kelly BT. Anatomy of the hip: Open and arthroscopic structure and function. Oper Tech Orthop. 2005;15(3):160–74.

30. Dinauer PA, Murphy KP, Carroll JF. Sublabral Sulcus at the Posteroinferior Acetabulum: A Potential Pitfall in MR Arthrography Diagnosis of Acetabular Labral Tears. American Journal of Roentgenology. 2004 Dec 1;183(6):1745–53.

31. Pfirrmann CWA, Metzdorf A, Zanetti M, Hodler J, Boos N. Magnetic Resonance Classification of Lumbar Intervertebral Disc Degeneration. Spine (Phila Pa 1976). 2001;26(17).

32. Malhotra N, Mithal A. Osteo.

33. Press D. Epidemiology and treatment of osteoporosis in women : an Indian perspective. 2015;841–50.

34. Bhadada SK, Chadha M, Sriram U, Pal R, Paul T V, Khadgawat R. The Indian Society for Bone and Mineral Research (ISBMR) position statement for the diagnosis and treatment of osteoporosis in adults. 2021;1–13.

35. Singh S V, Tripathi A. An overview of osteoporosis for the practising prosthodontist. Gerodontology. 2010 Dec;27(4):308–14.

36. Kanis JA. Assessment of fracture risk and its application to screening for postmenopausal osteoporosis: synopsis of a WHO report. WHO Study Group. Osteoporos Int. 1994 Nov;4(6):368–81.

37. Zou Z, Liu W, Cao L, Liu Y, He T, Peng S, et al. Advances in the occurrence and biotherapy of osteoporosis. Biochem Soc Trans. 2020 Jul 6;48(4):1623–36.

38. Liu L, Webster TJ. In Situ Sensor Advancements for Osteoporosis Prevention, Diagnosis, and Treatment. Curr Osteoporos Rep. 2016 Dec;14(6):386–95.

39. Vina ER, Kwoh CK. Epidemiology of osteoarthritis: Literature update. Curr Opin Rheumatol. 2018;30(2):160–7.

40. Lv F, Cai X, Yang W, Gao L, Chen L, Wu J, et al. Denosumab or romosozumab therapy and risk of cardiovascular events in patients with primary osteoporosis: Systematic review and meta-analysis. Bone [Internet]. 2020;130:115121. Available from: https://www.sciencedirect.com/science/article/pii/S8756328219304144

41. Jiang Y, Zhang P, Zhang X, Lv L. Advances in mesenchymal stem cell transplantation for the treatment of osteoporosis. 2021;(October 2020):1–19.

42. Suzuki T, Nakamura Y, Kato H. Vitamin D and Calcium Addition during Denosumab Therapy over a Period of Four Years Significantly Improves Lumbar Bone Mineral Density in Japanese Osteoporosis Patients. Vol. 10, Nutrients . 2018.

43. Boer CG, Hatzikotoulas K, Southam L, Meurs JBJ van. Resource Deciphering osteoarthritis genetics across 826 , 690 individuals from 9 populations ll ll Deciphering osteoarthritis genetics across 826 , 690 individuals from 9 populations. 2021;4784–818.

44. Chen A, Gupte C, Akhtar K, Smith P, Cobb J. The Global Economic Cost of Osteoarthritis: How the UK Compares. Arthritis. 2012;2012:1–6.

45. Tanna S, Mph PD, Wittenauer BR, Smith L, Aden K. Priority Medicines for Europe and the World " A Public Health Approach to Innovation " Update on 2004 Background Paper Background Paper 6 . 12 Osteoarthritis. 2013;

46. Nelson AE, Hu D, Arbeeva L, Alvarez C, Cleveland RJ, Schwartz TA, et al. The Prevalence of Knee Symptoms, Radiographic, and Symptomatic Osteoarthritis at Four Time Points: The Johnston County Osteoarthritis Project, 1999-2018. ACR Open Rheumatol. 2021 Aug 1;3(8):558–65.

47. Jordan JM, Helmick CG, Renner JB, Luta G, Dragomir AD, Woodard J, et al. Prevalence of hip symptoms and radiographic and symptomatic hip osteoarthritis in African Americans and Caucasians: The Johnston County osteoarthritis project. Journal of Rheumatology. 2009 Apr;36(4):809–15.

48. Hall M, van der Esch M, Hinman RS, Peat G, de Zwart A, Quicke JG, et al. How does hip osteoarthritis differ from knee osteoarthritis? Vol. 30, Osteoarthritis and Cartilage. W.B. Saunders Ltd; 2022. p. 32–41.

49. Bannuru RR, Osani MC, Vaysbrot EE, Arden NK, Bennell K, Bierma-Zeinstra SMA, et al. OARSI guidelines for the non-surgical management of knee, hip, and polyarticular osteoarthritis. Osteoarthritis Cartilage. 2019 Nov 1;27(11):1578–89.

50. Kolasinski SL, Neogi T, Hochberg MC, Oatis C, Guyatt G, Block J, et al. Foundation Guideline for the Management of Osteoarthritis of the Hand, Hip, and Knee. Arthritis Care Res (Hoboken) [Internet]. 2020;72(2):149–62. Available from: https://onlinelibrary.wiley.com/doi/10.1002/acr.24131

51. Haq I, Murphy E, Dacre J. Osteoarthritis. Postgrad Med J. 2003 Jul;79(933):377–83.

52. Jamil Z. EFFECTIVENESS OF GROUP COGNITIVE BEHAVIORAL THERAPY ON PAIN , FUNCTIONAL DISABILITY AND PSYCHOLOGICAL OUTCOMES AMONG KNEE OSTEOARTHRITIS PATIENTS SEEN AT MALAYSIAN GOVERNMENTHOSPITAL. (June 2015).

53. Felson DT. Epidemiology of hip and knee osteoartrritis. Epidemiol Rev. 1988;10(1):1–28.

54. March L, Cross M, Arden N HG. Osteoarthritis: A Serious Disease, Submitted to the U. S. Food and Drug Administration. Oarsi. 2016;1–103.

55. Joshi VL, Chopra A. Is there an urban-rural divide? Population surveys of rheumatic musculoskeletal disorders in the Pune Region of India using the COPCORD Bhigwan model. Journal of Rheumatology. 2009;36(3):614–22.

56. Office CS, Implementation P. Situation Analysis Of The Elderly in India. 2011;(June).

57. Swärdh E, Jethliya G, Khatri S, Kindblom K, Swärdh E, Jethliya G, et al. Approaches to osteoarthritis - A qualitative study among patients in a rural setting in Central Western India Approaches to osteoarthritis - A qualitative study among patients in a rural. Physiother Theory Pract. 2021;00(00):1–10.

58. Kloppenburg M, Berenbaum F. Osteoarthritis year in review 2019: epidemiology and therapy. Osteoarthritis Cartilage. 2020;28(3):242–8.

59. Mobasheri A, Saarakkala S, Finnilä M, Karsdal MA, Bay-Jensen AC, van Spil WE. Recent advances in understanding the phenotypes of osteoarthritis. Vol. 8, F1000Research. F1000 Research Ltd; 2019.

60. Johnson VL, Hunter DJ. The epidemiology of osteoarthritis. Best practice & research Clinical rheumatology. 2014 Feb;28(1):5—15.

61. Allen KD, Golightly YM. State of the evidence. Curr Opin Rheumatol. 2015 May;27(3):276–83.

62. Dai Z, Niu J, Zhang Y, Jacques P, Felson DT. Dietary intake of fibre and risk of knee osteoarthritis in two US prospective cohorts. Ann Rheum Dis. 2017 Aug;76(8):1411–9.

63. Dai Z, Lu N, Niu J, Felson DT, Zhang Y. Dietary Fiber Intake in Relation to Knee Pain Trajectory. Arthritis Care Res (Hoboken). 2017 Sep;69(9):1331–9.

64. Li H, Zeng C, Wei J, Yang T, Gao SG, Li YS, et al. Relationship between soy milk intake and radiographic knee joint space narrowing and osteophytes. Rheumatol Int. 2016 Sep;36(9):1215–22.

65. Veronese N, Stubbs B, Noale M, Solmi M, Luchini C, Smith TO, et al. Adherence to a Mediterranean diet is associated with lower prevalence of osteoarthritis: Data from the osteoarthritis initiative. Clin Nutr. 2017 Dec;36(6):1609–14.

66. Castaño-Betancourt MC, Evans DS, Ramos YFM, Boer CG, Metrustry S, Liu Y, et al. Novel Genetic Variants for Cartilage Thickness and Hip Osteoarthritis. PLoS Genet. 2016 Oct 1;12(10).

67. Rim YA, Ju JH. The role of fibrosis in osteoarthritis progression. Vol. 11, Life. MDPI AG; 2021. p. 1–13.

68. Swärdh E, Jethliya G, Khatri S, Kindblom K, Opava CH. Approaches to osteoarthritis - A qualitative study among patients in a rural setting in Central Western India. Physiother Theory Pract. 2021;

69. Paxton EW, Mohaddes M, Laaksonen I, Lorimer M, Graves SE, Malchau H, et al. Meta-analysis of individual registry results enhances international registry collaboration. Acta Orthop. 2018 Jul 4;89(4):369–73.

70. Ulrich SD, Seyler TM, Bennett D, Delanois RE, Saleh KJ, Thongtrangan I, et al. Total hip arthroplasties: What are the reasons for revision? Int Orthop. 2008;32(5):597–604.

71. Pachore JA, Vaidya S V, Thakkar CJ, Bhalodia HKP, Wakankar HM. ISHKS joint registry: A preliminary report. Indian J Orthop. 2013 Sep;47(5):505–9.

72. Sebastian S, Malhotra R, Dhawan B. Prosthetic Joint Infection : A Major Threat to Successful Total Joint Arthroplasty. Indian J Med Microbiol. 2019;36(4):475–87.

73. Kuiper JH. Numerical optimization of artificial hip joint designs.

74. Healy WL, Valle CJ Della, Iorio R, Berend KR, Cushner FD, Dalury DF, et al. Complications of Total Knee Arthroplasty Standardized List and Definitions of The Knee Society. 2013;215–20.

75. Pagnano MW, McLamb LA, Trousdale RT. Primary and Revision Total Hip Arthroplasty for Patients 90 Years of Age and Older. Mayo Clin Proc [Internet]. 2003;78(3):285–8. Available from: https://www.sciencedirect.com/science/article/pii/S0025619611620466

76. Huiskes R, Weinans H, Van Rietbergen B. The Relationship Between Stress Shielding and Bone Resorption Around Total Hip Stems and the Effects of Flexible Materials [Internet]. Available from: http://journals.lww.com/clinorthop

77. Cortis G, Mileti I, Nalli F, Palermo E, Cortese L. Additive manufacturing structural redesign of hip prostheses for stress-shielding reduction and improved functionality and safety. Mechanics of Materials. 2022 Feb 1;165.

78. Yu G, Li Z, Li S, Zhang Q, Hua Y, Liu H, et al. The select of internal architecture for porous Ti alloy scaffold: A compromise between mechanical properties and permeability. Mater Des. 2020 Jul 1;192.

79. Anderson Engh C, Ellis TJ, Koralewicz LM, McAuley JP, Engh CA. Extensively Porous-Coated Femoral Revision for Severe Femoral Bone Loss Minimum 10-Year Follow-Up. J Arthroplasty. 2002;17(8).

80. Sodhi N, Mont MA. Comment Survival of total hip replacements. The Lancet. 2017;393(10172):613.

81. Kurtz SM, Ong KL, Lau E, Bozic KJ, Berry D, Parvizi J. Prosthetic joint infection risk after TKA in the Medicare population. Clin Orthop Relat Res. 2010 Jan;468(1):52–6.

82. Rajaee SS, Campbell JC, Mirocha J, Paiement GD. Increasing Burden of Total Hip Arthroplasty Revisions in Patients Between 45 and 64 Years of Age. JBJS. 2018;100(6).

83. Siwach R, Dahiya S. Anthropometric study of proximal femur geometry and its clinical application. Indian J Orthop. 2003;37:247.

84. El-Najjar M, McWilliams KR. Forensic Anthropology: The Structure, Morphology, and Variation of Human Bone and Dentition. In 1977.

85. Ericksen MF. Aging changes in the medullary cavity of the proximal femur in American Blacks and Whites. Am J Phys Anthropol. 1979 Nov;51(4):563–9.

86. Moisio KC, Sumner DR, Shott S, Hurwitz DE. Normalization of joint moments during gait: A comparison of two techniques. J Biomech. 2003 Apr 1;36(4):599–603.

87. Foucher KC. Sex-specific hip osteoarthritis-associated gait abnormalities: Alterations in dynamic hip abductor function differ in men and women. Clinical Biomechanics. 2017 Oct 1;48:24–9.

88. Galmiche R, Migaud H, Beaulé PE. Hip Anatomy and Biomechanics Relevant to Hip Replacement. In: Rivière C, Vendittoli PA, editors. Cham (CH); 2020. p. 9–21.

89. Cadossi M, Tedesco G, Sambri A, Mazzotti A, Giannini S. Hip Resurfacing Implants. Orthopedics. 2015 Aug;38(8):504–9.

90. Girard J, Lavigne M, Vendittoli PA, Migaud H. [Hip resurfacing: current state of knowledge]. Rev Chir Orthop Reparatrice Appar Mot. 2008 Dec;94(8):715–30.

91. dONaLd a. NEUmaNN. Sagittal Plane (From the Side) Superior-Inferior (cm). Journal of orthopaedic & sports physical therapy [Internet]. 2010; Available from: www.jospt.org

92. Correa TA, Crossley KM, Kim HJ, Pandy MG. Contributions of individual muscles to hip joint contact force in normal walking. J Biomech. 2010 May;43(8):1618–22.

93. Lenaerts G, Mulier M, Spaepen A, van der Perre G, Jonkers I. Aberrant pelvis and hip kinematics impair hip loading before and after total hip replacement. Gait Posture. 2009 Oct;30(3):296–302.

94. Christophe AGM, Wesseling M, Corten K, Nieuwenhuys A, Monari D, Simon JP, et al. Hip movement pathomechanics of patients with hip osteoarthritis aim at reducing hip joint loading on the osteoarthritic side. Gait Posture. 2018 Jan 1;59:11–7.

95. Bertocci GE, Munin MC, Frost KL, Burdett R, Wassinger CA, Fitzgerald SG. Isokinetic Performance after Total Hip Replacement. Am J Phys Med Rehabil. 2004 Jan;83(1):1–9.

96. Watelain E, Dujardin F, Babier F, Dubois D, Allard P. Pelvic and lower limb compensatory actions of subjects in an early stage of hip osteoarthritis. Arch Phys Med Rehabil. 2001;82(12):1705–11.

97. Judd DL, Dennis DA, Thomas AC, Wolfe P, Dayton MR, Stevens-Lapsley JE. Muscle strength and functional recovery during the first year after THA. In: Clinical Orthopaedics and Related Research. Springer New York LLC; 2014. p. 654–64.

98. Eitzen I, Fernandes L, Nordsletten L, Risberg MA. Sagittal plane gait characteristics in hip osteoarthritis patients with mild to moderate symptoms compared to healthy controls: A cross-sectional study. BMC Musculoskelet Disord. 2012;13.

99. Rasch A, Dalén N, Berg HE. Muscle strength, gait, and balance in 20 patients with hip osteoarthritis followed for 2 years after THA. Acta Orthop. 2010 Apr;81(2):183–8.

100. Noguchi Y, Miura H, Takasugi S ichiro, Iwamoto Y. Cartilage and Labrum Degeneration in the Dysplastic Hip Generally Originates in the Anterosuperior Weight-Bearing Area: An Arthroscopic Observation. Arthroscopy: The Journal of Arthroscopic & Related Surgery [Internet]. 1999;15(5):496–506. Available from: https://www.sciencedirect.com/science/article/pii/S0749806399001115

101. Hefti F. Pediatric orthopedics in practice: Second edition. 2015. 1–905 p.

102. Bergmann G, Graichen F, Rohlmann A. Is staircase walking a risk for the fixation of hip implants? J Biomech. 1995 May;28(5):535–53.

103. Bergmann G, Graichen F, Rohlmann A. Hip joint loading during walking and running, measured in two patients. J Biomech. 1993 Aug;26(8):969–90.

104. Rydell NW. Forces Acting on the Femoral Head-Prosthesis: A Study on Strain Gauge Supplied Prostheses in Living Persons. Acta Orthop Scand. 1966 May 1;37(sup88):1–132.

105. Foucher KC, Hurwitz DE, Wimmer MA. Relative importance of gait vs. joint positioning on hip contact forces after total hip replacement. Journal of Orthopaedic Research. 2009 Dec;27(12):1576–82.

106. Yoon~ YS, Mansours JM. THE PASSIVE ELASTIC MOMENT AT THE HIP*. Vol. 15. 1982.

107. GENDER_DIFFERENCES_IN_JOINT_BIOMECHANICS_DURING.2.

108. Cho SH, Park JM, Kwon OY. Gender differences in three dimensional gait analysis data from 98 healthy Korean adults. Clinical Biomechanics. 2004;19(2):145–52.

109. Boyer KA, Beaupre GS, Andriacchi TP. Gender differences exist in the hip joint moments of healthy older walkers. J Biomech. 2008 Dec 5;41(16):3360–5.

110. Anderson JY, Trinkaus E. Patterns of sexual, bilateral and interpopulational variation in human femoral neck-shaft angles. J Anat. 1998 Feb;192 (Pt 2(Pt 2):279–85.

111. Gilligan I, Chandraphak S, Mahakkanukrauh P. Femoral neck-shaft angle in humans: variation relating to climate, clothing, lifestyle, sex, age and side. J Anat. 2013 Aug;223(2):133–51.

112. Milligan DJ, O'Brien S, Bennett D, Hill JC, Beverland DE. The effects of age and gender on the diameter of the femoral canal in patients who undergo total hip replacement. Bone Joint J. 2013 Mar;95-B(3):339–42.

113. Tannenbaum E, Kopydlowski N, Smith M, Bedi A, Sekiya JK. Gender and racial differences in focal and global acetabular version. J Arthroplasty. 2013/06/18. 2014 Feb;29(2):373–6.

114. Wang SC, Brede C, Lange D, Poster CS, Lange AW, Kohoyda-Inglis C, et al. Gender differences in hip anatomy: possible implications for injury tolerance in frontal collisions. Annu Proc Assoc Adv Automot Med. 2004;48:287–301.

115. Egan PF, Gonella VC, Engensperger M, Ferguson SJ, Shea K. Computationally designed lattices with tuned properties for tissue engineering using 3D printing. PLoS One. 2017 Aug 10;12(8):e0182902.

116. Woo SH, Sung MJ, Park KS, Yoon TR. Three-dimensional-printing Technology in Hip and Pelvic Surgery: Current Landscape. Hip Pelvis. 2020;32(1):1.

117. Thiesen DM, Ntalos D, Korthaus A, Petersik A, Frosch KH, Hartel MJ. A comparison between Asians and Caucasians in the dimensions of the femoral isthmus based on a 3D-CT analysis of 1189 adult femurs. European Journal of Trauma and Emergency Surgery. 2021;

118. Sylvester AD, Lautzenheiser SG, Kramer PA. A review of musculoskeletal modelling of human locomotion. Interface Focus. 2021 Aug 26;11(5):20200060.

119. Madhusoodanan BJ. A troubled calculus. 2021;

120. Rubin PJ, Leyvraz PF, Aubaniac JM, Argenson JN, Estève P, de Roguin B. The morphology of the proximal femur. A three-dimensional radiographic analysis. J Bone Joint Surg Br. 1992 Jan;74(1):28–32.

121. Noble PC, Alexander JW, Lindahl LJ, Yew DT, Granberry WM, Tullos HS. The anatomic basis of femoral component design. Clin Orthop Relat Res. 1988 Oct;(235):148–65.

122. Doraiswamy R, Mithrason AT. A STUDY ON THE PROXIMAL FEMORAL GEOMETRY FOR STANDARDIZING THE FEMORAL COMPONENT DESIGN TO SUIT INDIAN NEEDS IN TOTAL HIP REPLACEMENT. 2016;4(2):2416–22.

123. Anderson AE, Ellis BJ, Maas SA, Weiss JA. Effects of idealized joint geometry on finite element predictions of cartilage contact stresses in the hip. J Biomech. 2010 May;43(7):1351–7.

124. Wong KC. 3D-printed patient-specific applications in orthopedics. Orthop Res Rev. 2016 Oct 14;8:57–66.

125. Lombardi A v., Berend KR, Mallory TH, Skeels MD, Adams JB. Survivorship of 2000 tapered titanium porous plasma-sprayed femoral components. In: Clinical Orthopaedics and Related Research. Springer New York; 2009. p. 146–54.

126. Khanuja HS, Banerjee S, Jain D, Pivec R, Mont MA. Short bone-conserving stems in cementless hip arthroplasty. Journal of Bone and Joint Surgery - American Volume. 2014 Oct 15;96(20):1742–52.

127. Khanuja HS, Vakil JJ, Goddard MS, Mont MA. Cementless femoral fixation in total hip arthroplasty. Vol. 93, Journal of Bone and Joint Surgery. Journal of Bone and Joint Surgery Inc.; 2011. p. 500–9.

128. Ma HH, Chou TFA, Tsai SW, Chen CF, Wu PK, Chen WM. Uncemented femoral stem design might have an impact on postoperative periprosthetic femur fracture pattern. A Comparison

between flat-wedge and dual-wedge stems. Injury [Internet]. 2021;52(11):3461–70. Available from: https://doi.org/10.1016/j.injury.2021.02.039

129.   Zhang Y, Zhang Y, Sun JN, Hua ZJ, Chen XY, Feng S. Comparison of cylindrical and tapered stem designs for femoral revision hip arthroplasty. BMC Musculoskelet Disord. 2020 Jun 29;21(1).

130.   Richards CJ, Duncan CP, Masri BA, Garbuz DS. Femoral revision hip arthroplasty: A comparison of two stem designs. In: Clinical Orthopaedics and Related Research. Springer New York; 2010. p. 491–6.

131.   McInnes J, Allen J, Garceau SP, Warschawski Y, Rajgopal R, Safir OA, et al. Revision Hip Arthroplasty Using a Porous-coated or Taper ZMR Implant: Minimum 10-year Follow-up of Implant Survivorship. J Am Acad Orthop Surg. 2021;29(1):e41–50.

132.   Mukherjee S, Dhara S, Saha P. Enhancing the biocompatibility of Ti6Al4V implants by laser surface microtexturing: an in vitro study. International Journal of Advanced Manufacturing Technology. 2015 Jan 1;76(1–4):5–15.

133.   WJO-12-534-2.

134.   Richards CJ, Duncan CP, Masri BA, Garbuz DS. Femoral revision hip arthroplasty: A comparison of two stem designs. In: Clinical Orthopaedics and Related Research. Springer New York; 2010. p. 491–6.

135.   12877_2019_Article_1123.

136.   Khanuja HS, Banerjee S, Jain D, Pivec R, Mont MA. Short bone-conserving stems in cementless hip arthroplasty. Journal of Bone and Joint Surgery - American Volume. 2014 Oct 15;96(20):1742–52.

137.   Krishnan SP, Dawood A, Richards R, Henckel J, Hart AJ. A review of rapid prototyped surgical guides for patient-specific total knee replacement. Vol. 94 B, Journal of Bone and Joint Surgery - Series B. 2012. p. 1457–61.

138.   Giardina F, Castagnini F, Stea S, Bordini B, Montalti M, Toni A. Short Stems Versus Conventional Stems in Cementless Total Hip Arthroplasty: A Long-Term Registry Study. Journal of Arthroplasty. 2018 Jun 1;33(6):1794–9.

139.   Wriggers P, Eberhard P. Lecture Notes in Applied and Computational Mechanics Volume 84 Series editors [Internet]. Available from: http://www.springer.com/series/4623

140. Kutzner KP, Hechtner M, Pfeil D, Rehbein P, Kovacevic MP, Schneider M, et al. Incidence of heterotopic ossification in minimally invasive short-stem tha using the modified anterolateral approach. HIP International. 2017 Mar 1;27(2):162–8.

141. Molli RG, Lombardi A v., Berend KR, Adams JB, Sneller MA. A short tapered stem reduces intraoperative complications in primary total hip arthroplasty. In: Clinical Orthopaedics and Related Research. Springer New York LLC; 2012. p. 450–61.

142. Hochreiter J, Hejkrlik W, Emmanuel K, Hitzl W, Ortmaier R. Blood loss and transfusion rate in short stem hip arthroplasty. A comparative study. Int Orthop. 2017 Jul 1;41(7):1347–53.

143. Kutzner KP, Pfeil J. Individualized Stem-positioning in Calcar-guided Short-stem Total Hip Arthroplasty. JoVE [Internet]. 2018;(132):e56905. Available from: https://www.jove.com/56905

144. Innmann MM, Spier K, Streit MR, Aldinger PR, Bruckner T, Gotterbarm T, et al. Comparative Analysis of the Reconstruction of Individual Hip Anatomy Using 3 Different Cementless Stem Designs in Patients With Primary Hip Osteoarthritis. Journal of Arthroplasty. 2018 Apr 1;33(4):1126–32.

145. Amenabar T, Marimuthu K, Hawdon G, Gildone A, Mcmahon S. Total hip arthroplasty using a short-stem prosthesis: restoration of hip anatomy. Vol. 23, Journal of Orthopaedic Surgery. 2015.

146. Kutzner KP, Kovacevic MP, Roeder C, Rehbein P, Pfeil J. Reconstruction of femoro-acetabular offsets using a short-stem. Int Orthop. 2015 Dec 20;39(7):1269–75.

147. Yan SG, Weber P, Steinbrück A, Hua X, Jansson V, Schmidutz F. Periprosthetic bone remodelling of short-stem total hip arthroplasty: a systematic review. Vol. 42, International Orthopaedics. Springer Verlag; 2018. p. 2077–86.

148. Hochreiter J, Mattiassich G, Ortmaier R, Steinmair M, Anderl C. Femoral bone remodeling after short-stem total hip arthroplasty: a prospective densitometric study. Int Orthop. 2020 Apr 1;44(4):753–9.

149. Grimberg A, Jansson V, Lützner J, Melsheimer O, Morlock M, Steinbrück A, et al. German Arthroplasty Registry (EPRD): Annual Report 2020. 2020.

150. Swiss National Joint Registry. Hip and knee replacement results Annual Report of the Swiss National Joint Registry, Hip and Knee SIRIS-Foundation for Quality Assurance in Implant Surgery swiss orthopaedics-Swiss Society of Orthopaedics and Traumatology ANQ-National Association for the Development of Quality in Swiss Hospitals and Clinics. 2012.

151. Australian Orthopaedic Association National Joint Replacement Registry. Australian Orthopaedic Association National Joint Replacement Registry [Internet]. 2020. Available from: https://aoanjrr.sahmri.com/annual-reports-

152. Gkagkalis G, Goetti P, Mai S, Meinecke I, Helmy N, Bosson D, et al. Cementless short-stem total hip arthroplasty in the elderly patient - Is it a safe option?: A prospective multicentre observational study. BMC Geriatr. 2019 Apr 17;19(1).

153. Kutzner KP, Donner S, Loweg L, Rehbein P, Dargel J, Drees P, et al. Mid-term results of a new-generation calcar-guided short stem in THA: clinical and radiological 5-year follow-up of 216 cases. Journal of Orthopaedics and Traumatology. 2019 Dec 1;20(1).

154. Ettinger M, Ettinger P, Lerch M, Radtke K, Budde S, Ezechieli M, et al. The NANOS short stem in total hip arthroplasty: A mid term follow-up. HIP International. 2011 Sep;21(5):583–6.

155. Gabriela von L, Thilo F. 10-Year Experience With Short Stem Total Hip Arthroplasty. Orthopedics [Internet]. 2015 Mar 1;38(3):S51–6. Available from: https://doi.org/10.3928/01477447-20150215-57

156. Tatani I, Megas P, Panagopoulos A, Diamantakos I, Nanopoulos P, Pantelakis S. Comparative analysis of the biomechanical behavior of two different design metaphyseal-fitting short stems using digital image correlation. Biomed Eng Online. 2020 Aug 19;19(1).

157. Chakraborty A, Datta P, Majumder S, Mondal SC, Roychowdhury A. Finite element and experimental analysis to select patient's bone condition specific porous dental implant, fabricated using additive manufacturing. Comput Biol Med. 2020 Sep 1;124.

158. Chatterjee S, Kobylinski S, Basu B. Finite Element Analysis to Probe the Influence of Acetabular Shell Design, Liner Material, and Subject Parameters on Biomechanical Response in Periprosthetic Bone. J Biomech Eng. 2018 Oct 1;140(10).

159. Chatterjee S, Kobylinski S, Basu B. Finite Element Analysis to Probe the Influence of Acetabular Shell Design, Liner Material, and Subject Parameters on Biomechanical Response in Periprosthetic Bone. J Biomech Eng. 2018 Oct 1;140(10).

160. Chakraborty A, Datta P, Kumar CS, Majumder S, Roychowdhury A. Probing combinational influence of design variables on bone biomechanical response around dental implant-supported fixed prosthesis. J Biomed Mater Res B Appl Biomater. 2022 Oct 1;110(10):2338–52.

161. Chatterjee S, Roy S, Majumder S, Roychowdhury A. Biomechanical Analysis to Probe Role of Bone Condition and Subject Weight in Stiffness Customization of Femoral Stem for Improved Periprosthetic Biomechanical Response. J Biomech Eng. 2020;142(10).

162. Li M, Venäläinen MS, Chandra SS, Patel R, Fripp J, Engstrom C, et al. Discrete element and finite element methods provide similar estimations for hip joint contact mechanics during walking gait. J Biomech. 2021 Jan 22;115.

163. Todd JN, Maak TG, Anderson AE, Ateshian GA, Weiss JA. How Does Chondrolabral Damage and Labral Repair Influence the Mechanics of the Hip in the Setting of Cam Morphology? A Finite-Element Modeling Study. Clin Orthop Relat Res. 2022 Mar 1;480(3):602–15.

164. Anderson AE, Ellis BJ, Maas SA, Weiss JA. Effects of idealized joint geometry on finite element predictions of cartilage contact stresses in the hip. J Biomech. 2010 May;43(7):1351–7.

165. Decking R, Puhl W, Simon U, Claes LE. Changes in strain distribution of loaded proximal femora caused by different types of cementless femoral stems. Clinical Biomechanics [Internet]. 2006 Jun 1;21(5):495–501. Available from: https://doi.org/10.1016/j.clinbiomech.2005.12.011

166. Østbyhaug PO, Klaksvik J, Romundstad P, Aamodt A, Østbyhaug P, Surgeon O. human femora with anatomical and customised femoral stems. 2009;91–676.

167. Maistrelli L, Fornasier V, Binnington A, McKENZIE K, Sessa V, Harrington I. EFFECT OF STEM MODULUS IN A TOTAL HIP ARTHROPLASTY MODEL. Vol. 73. 1991.

168. Kuiper JH, Huiskes R. Mathematical Optimization of Elastic Properties: Application to Cementless Hip Stem Design. J Biomech Eng [Internet]. 1997 May 1;119(2):166–74. Available from: https://doi.org/10.1115/1.2796076

169. van Rietbergen B, Huiskes R. Load transfer and stress shielding of the hydroxyapatite-ABG hip: A study of stem length and proximal fixation. J Arthroplasty [Internet]. 2001 Dec 1;16(8):55–63. Available from: https://doi.org/10.1054/arth.2001.28369

170. Tayton E, Evans S, O RD. Mapping the strain distribution on the proximal femur with titanium and flexible-stemmed implants using digital image correlation. Br]. 2010;92–1176.

171. Jetté B, Brailovski V, Simoneau C, Dumas M, Terriault P. Development and in vitro validation of a simplified numerical model for the design of a biomimetic femoral stem. J Mech Behav Biomed Mater. 2018 Jan 1;77:539–50.

172. Boyle C, Kim IY. Comparison of different hip prosthesis shapes considering micro-level bone remodeling and stress-shielding criteria using three-dimensional design space topology optimization. J Biomech. 2011 Jun 3;44(9):1722–8.

173. Cementless_Fixation_of__Isoelastic__Hip.10.

174. Cilla M, Checa S, Duda GN. Strain shielding inspired re-design of proximal femoral stems for total hip arthroplasty. Journal of Orthopaedic Research. 2017 Nov 1;35(11):2534–44.

175. Gross S, Abel EW. A finite element analysis of hollow stemmed hip prostheses as a means of reducing stress shielding of the femur. Vol. 34, Journal of Biomechanics. 2001.

176. Santare MH, Joshi MG, Advani SG, Miller F, Santare MH. Analysis of a femoral hip prosthesis designed to reduce stress shielding. Vol. 33, Journal of Biomechanics. 2000.

177. Schmidt J, Hackenbroch • M H. The Cenos hollow stem in total hip arthroplasty: first experiences in a prospective study. Vol. 113, Arch Orthop Trauma Surg. 1994.

178. Mattheck C, Vorberg U, Kranz C. Die Auswirkungen der Hohlschaftendoprothese auf die Spannungsverteilung in der Kortikalis - The Effect of the Hollow-Stem-Prosthesis on the Distribution of Stresses in the Cortical Bone. 1990;35(12):316–9. Available from: https://doi.org/10.1515/bmte.1990.35.12.316

179. Gross S, Abel EW. A finite element analysis of hollow stemmed hip prostheses as a means of reducing stress shielding of the femur. Vol. 34, Journal of Biomechanics. 2001.

180. Kumar M, Rappo S, Facchini L, Tomaselli M. Translation of three-dimensional printing for orthopedic devices. Vol. 47, MRS Bulletin. Springer Nature; 2022. p. 49–58.

181. Werner A, Lechniak Z, Skalski K, Ke K. Design and manufacture of anatomical hip joint endoprostheses using CAD / CAM systems. 2000;107:181–6.

182. Frank MC, Joshi A, Anderson DD, Thomas TP, Rudert MJ, Tochigi Y, et al. Patient-Specific Bone Implants using Subtractive Rapid Prototyping. :854–63.

183. Xu Y, Wu X, Guo X, Kong B, Zhang M, Qian X, et al. The Boom in 3D-Printed Sensor Technology. Vol. 17, Sensors . 2017.

184. Hann BA. Powder reuse and its effects on laser based powder fusion additive manufactured Alloy 718. SAE International Journal of Aerospace. 2016 Aug 4;9:209+.

185. Leuders S, Thöne M, Riemer A, Niendorf T, Tröster T, Richard HA, et al. On the mechanical behaviour of titanium alloy TiAl6V4 manufactured by selective laser melting : Fatigue resistance and crack growth performance. Int J Fatigue. 2013;48:300–7.

186. Shipley H, Mcdonnell D, Culleton M, Coull R, Lupoi R, Donnell GO, et al. International Journal of Machine Tools and Manufacture Optimisation of process parameters to address fundamental challenges during selective laser melting of Ti-6Al-4V : A review. Int J Mach Tools Manuf. 2018;128(January):1–20.

187. Panwisawas C, Tang YT, Reed RC. Metal 3D printing as a disruptive technology for superalloys. Nat Commun. 2020;1–4.

188. Chen Q, Guillemot G, Gandin C andré, Bellet M. Three-dimensional finite element thermomechanical modeling of additive manufacturing by selective laser melting for ceramic materials. Addit Manuf [Internet]. 2017;16:124–37. Available from: http://dx.doi.org/10.1016/j.addma.2017.02.005

189. Shipley H, Mcdonnell D, Culleton M, Coull R, Lupoi R, Donnell GO, et al. International Journal of Machine Tools and Manufacture Optimisation of process parameters to address fundamental challenges during selective laser melting of Ti-6Al-4V : A review. Int J Mach Tools Manuf. 2018;128(September 2017):1–20.

190. Panwisawas C, Perumal B, Ward RM, Turner N, Turner RP, Brooks JW, et al. Acta Materialia Keyhole formation and thermal fl uid fl ow-induced porosity during laser fusion welding in titanium alloys : Experimental and modelling. Acta Mater. 2017;126:251–63.

191. Sames WJ, List FA, Pannala S, Dehoff RR, Babu SS. The metallurgy and processing science of metal additive manufacturing. International Materials Reviews. 2016 Jul 3;61(5):315–60.

192. Nikolay K, Yurii V, Sergei E, Michail B, Rapid VI, Journal P, et al. Absorptance of powder materials suitable for laser sintering. 2000;6:155–60.

193. Gusarov A V. Modelling of radiation transfer in metallic powders at laser treatment. 2005;48:3423–34.

194. Osmanlic TSF, Körner RFSC. Melt pool dynamics during selective electron beam melting. 2014;(August 2013):1303–7.

195. Louvis E, Fox P, Sutcliffe CJ. Journal of Materials Processing Technology Selective laser melting of aluminium components. Journal of Materials Processing Tech [Internet]. 2011;211(2):275–84. Available from: http://dx.doi.org/10.1016/j.jmatprotec.2010.09.019

196. Kruth J, Levy G, Klocke F, Childs THC. Consolidation phenomena in laser and powder-bed based layered manufacturing. 2007;56(1):730–59.

197. Otto A. A 3D transient model of keyhole and melt pool dynamics in laser beam welding applied to the joining of zinc coated sheets A 3D transient model of keyhole and melt pool

dynamics in laser beam welding applied to the joining of zinc coated sheets. 2018;(June 2009).

198. Mercelis P, Kruth J pierre. Residual stresses in selective laser sintering and selective laser melting. 2006;5(March):254–65.

199. Gu DD, Meiners W, Wissenbach K, Poprawe R. Laser additive manufacturing of metallic components: materials, processes and mechanisms. International Materials Reviews. 2012 May 1;57(3):133–64.

200. Murr LE, Quinones SA, Gaytan SM, Lopez MI, Rodela A, Martinez EY, et al. Microstructure and mechanical behavior of Ti-6Al-4V produced by rapid-layer manufacturing, for biomedical applications. J Mech Behav Biomed Mater. 2009;2(1):20–32.

201. Lane T, Lizak S, Seidel C, Stief P, Dantan J yves, Etienne A, et al. ScienceDirect ScienceDirect Spatter formation during laser beam melting AlSi10Mg France and effects on powder quality A new methodology to analyze the functional and physical architecture of existing products for *, an assembly product family identificati. Procedia CIRP [Internet]. 2018;74:33–8. Available from: https://doi.org/10.1016/j.procir.2018.08.008

202. Denti L, Sola A, Defanti S, Sciancalepore C, Bondioli F. Effect of Powder Recycling in Laser-based Powder Bed Fusion of Ti-6Al-4V. Manufacturing Technology [Internet]. 2019;19(2):190–6. Available from: https://doi.org/10.21062/ujep/268.2019/a/1213-2489/MT/19/2/190

203. Markl M, Carolin K. Multiscale Modeling of Powder Bed-Based Additive Manufacturing Multi-Scale Modeling of Powder-Bed-Based Additive Manufacturing. 2016;(May).

204. Mukherjee T, Manvatkar V, De A, DebRoy T. Dimensionless numbers in additive manufacturing. J Appl Phys. 2017 Feb 13;121(6):64904.

205. Heiple CR, Rope JR, Stagner RT, Aden RJ. Surface Active Element Effects on the Shape of Gta, Laser, and Electron Beam Welds. Welding Journal (Miami, Fla). 1983;62(3):72–7.

206. Hondros ED, McLean M, Mills KC, Mills KC, Keene BJ, Brooks RF, et al. Marangoni effects in welding. Philosophical Transactions of the Royal Society of London Series A: Mathematical, Physical and Engineering Sciences. 1998 Apr 15;356(1739):911–25.

207. van Elsen M, Al-Bender F, Kruth J. Application of dimensional analysis to selective laser melting. Rapid Prototyp J. 2008 Jan 1;14(1):15–22.

208. Mukherjee T, Manvatkar V, De A, DebRoy T. Mitigation of thermal distortion during additive manufacturing. Scr Mater. 2017;127:79–83.

209. Mukherjee T, Manvatkar V, De A, DebRoy T. Dimensionless numbers in additive manufacturing. J Appl Phys. 2017 Feb 14;121(6).

210. Olakanmi EO, Cochrane RF, Dalgarno KW. A review on selective laser sintering/melting (SLS/SLM) of aluminium alloy powders: Processing, microstructure, and properties. Vol. 74, Progress in Materials Science. Elsevier Ltd; 2015. p. 401–77.

211. Morgan R, Sutcliffe CJ, O'Neill W. Density analysis of direct metal laser re-melted 316L stainless steel cubic primitives. J Mater Sci. 2004;39(4):1195–205.

212. Olakanmi EO, Cochrane RF, Dalgarno KW. Densification mechanism and microstructural evolution in selective laser sintering of Al–12Si powders. J Mater Process Technol. 2011;211(1):113–21.

213. Jia Q, Gu D. Selective laser melting additive manufacturing of Inconel 718 superalloy parts: Densification, microstructure and properties. J Alloys Compd. 2014;585:713–21.

214. Carlton HD, Haboub A, Gallegos GF, Parkinson DY, MacDowell AA. Damage evolution and failure mechanisms in additively manufactured stainless steel. Materials Science and Engineering: A. 2016;651:406–14.

215. King WE, Barth HD, Castillo VM, Gallegos GF, Gibbs JW, Hahn DE, et al. Observation of keyhole-mode laser melting in laser powder-bed fusion additive manufacturing. J Mater Process Technol. 2014;214(12):2915–25.

216. Cunningham R, Nicolas A, Madsen J, Fodran E, Anagnostou E, Sangid MD, et al. Analyzing the effects of powder and post-processing on porosity and properties of electron beam melted Ti-6Al-4V. Mater Res Lett. 2017 Nov 3;5(7):516–25.

217. Mukherjee T, Zuback JS, De A, DebRoy T. Printability of alloys for additive manufacturing. Sci Rep. 2016;6(1):19717.

218. Darvish K, Chen ZW, Pasang T. Reducing lack of fusion during selective laser melting of CoCrMo alloy: Effect of laser power on geometrical features of tracks. Mater Des. 2016;112:357–66.

219. Kistler NA, Corbin DJ, Nassar AR, Reutzel EW, Beese AM. Effect of processing conditions on the microstructure, porosity, and mechanical properties of Ti-6Al-4V repair fabricated by directed energy deposition. J Mater Process Technol. 2019;264:172–81.

220. Wolff SJ, Lin S, Faierson EJ, Liu WK, Wagner GJ, Cao J. A framework to link localized cooling and properties of directed energy deposition (DED)-processed Ti-6Al-4V. Acta Mater. 2017;132:106–17.

221. Ahsan MN, Bradley R, Pinkerton AJ. Microcomputed tomography analysis of intralayer porosity generation in laser direct metal deposition and its causes. J Laser Appl. 2011 May 1;23(2):22009.

222. Bauereiß A, Scharowsky T, Körner C. Defect generation and propagation mechanism during additive manufacturing by selective beam melting. J Mater Process Technol. 2014;214(11):2522–8.

223. Wang Z, Denlinger E, Michaleris P, Stoica AD, Ma D, Beese AM. Residual stress mapping in Inconel 625 fabricated through additive manufacturing: Method for neutron diffraction measurements to validate thermomechanical model predictions. Mater Des. 2017;113:169–77.

224. Rafi HK, Pal D, Patil N, Starr TL, Stucker BE. Microstructure and Mechanical Behavior of 17-4 Precipitation Hardenable Steel Processed by Selective Laser Melting. J Mater Eng Perform. 2014;23(12):4421–8.

225. DebRoy T, Wei HL, Zuback JS, Mukherjee T, Elmer JW, Milewski JO, et al. Additive manufacturing of metallic components – Process, structure and properties. Prog Mater Sci. 2018;92:112–224.

226. DebRoy T, Wei HL, Zuback JS, Mukherjee T, Elmer JW, Milewski JO, et al. Additive manufacturing of metallic components – Process, structure and properties. Prog Mater Sci [Internet]. 2018;92:112–224. Available from: https://www.sciencedirect.com/science/article/pii/S0079642517301172

227. Library. MRS Bull. 2003;28(9):674–5.

228. Carter LN, Attallah MM, Reed RC. Laser Powder Bed Fabrication of Nickel-Base Superalloys : Influence of Parameters ; Characterisation , Quantification and Mitigation of Cracking. 2012;577–86.

229. Zhao X, Lin X, Chen J, Xue L, Huang W. The effect of hot isostatic pressing on crack healing, microstructure, mechanical properties of Rene88DT superalloy prepared by laser solid forming. Materials Science and Engineering: A. 2009;504(1):129–34.

230. Mukherjee T, Zhang W, DebRoy T. An improved prediction of residual stresses and distortion in additive manufacturing. Comput Mater Sci. 2017;126:360–72.

231. Outlook WE. World Energy Outlook 2018. 2018;

232. Sandhu K, Singh S. Sustainability for 3D Printing.

233. Khosravani MR, Reinicke T. On the environmental impacts of 3D printing technology. Appl Mater Today. 2020;20:100689.

234. Gao C, Wolff S, Wang S. Eco-friendly additive manufacturing of metals : Energy efficiency and life cycle analysis. J Manuf Syst. 2021;60(June):459–72.

235. Atzeni E, Catalano AR, Priarone PC. The technology , economy , and environmental sustainability of isotropic superfinishing applied to electron-beam melted Ti-6Al-4V components. 2021;437–53.

236. Gisario A, Kazarian M, Martina F, Mehrpouya M. Metal additive manufacturing in the commercial aviation industry : A review. J Manuf Syst [Internet]. 2019;53(June):124–49. Available from: https://doi.org/10.1016/j.jmsy.2019.08.005

237. Baumers M, Tuck CJ, Wildman R, Ashcroft I. Energy inputs to additive manufacturing : Does capacity utilization matter ? 2011;(January).

238. Azevedo JMC, Serrenho AC, Allwood JM. Energy and material efficiency of steel powder metallurgy. 2018;328:329–36.

239. Manufacturing L, Company FM. Powder Metallurgy — Intrinsically Sustainable.

240. Kruzhanov V, Arnhold V, Kruzhanov V, Arnhold V. Energy consumption in powder metallurgical manufacturing Energy consumption in powder metallurgical manufacturing. 2013;5899.

241. Gebler M, Uiterkamp AJMS, Visser C. A global sustainability perspective on 3D printing technologies. Energy Policy. 2014;74:158–67.

242. Huang R, Riddle M, Graziano D, Warren J, Das S, Nimbalkar S, et al. Energy and emissions saving potential of additive manufacturing : the case of lightweight aircraft components. J Clean Prod [Internet]. 2016;135:1559–70. Available from: http://dx.doi.org/10.1016/j.jclepro.2015.04.109

243. Priarone PC, Ingarao G, Lorenzo R, Settineri L. Influence of Material-Related Aspects of Additive and Subtractive Ti-6Al-4V Manufacturing on Energy Demand and Carbon Dioxide Emissions. 2016;21:191–202.

244. Tokita M. Spark Plasma Sintering (SPS) Method , Systems , and Applications. Second Edition. Handbook of Advanced Ceramics: Materials, Applications, Processing, and Properties. Elsevier; 2013. 1149–1177 p.

245. Choonara YE, Toit L Du, Kondiah PPD, Pillay V. Expert Review of Pharmacoeconomics & Outcomes 3D-printing and the effect on medical costs : a new era ? 2016;(January):21–32.

246. Banks J. Adding Value in Additive Manufacturing : Researchers in the United Kingdom and Europe Look to 3D Printing for Customization. (November 2013):22–6.

247. Ventola CL. Medical Applications for 3D Printing : Current and Projected Uses. 2014;39(10):704–11.

248. Lindemann C, Jahnke U, Habdank M, Koch R. Analyzing Product Lifecycle Costs for a Better Understanding of Cost Drivers in Additive Manufacturing. 23rd Annual International Solid Freeform Fabrication Symposium - An Additive Manufacturing Conference, SFF 2012. 2012.

249. Reiher T, Lindemann C, Jahnke U, Deppe G, Koch R. Holistic approach for industrializing AM technology : from part selection to test and verification. Progress in Additive Manufacturing. 2017;2(1):43–55.

250. Wall M. Thinking ahead the Future of Additive Manufacturing – Innovation Roadmapping of Required Advancements.

251. Mulugetta Y. Coordinating Lead Authors: :739–810.

252. Ashby MF. Chapter 2 - Resource consumption and its drivers. In: Ashby MF, editor. Materials and the Environment (Second Edition). Second Edition. Boston: Butterworth-Heinemann; 2013. p. 15–48.

253. Serpa D, Ev A. CO2 EMISSIONS FROM FUEL COMBUSTION.

254. Huckstep A. Economics of metal additive manufacturing. Digital alloys' guide to metal additive manufacturing. 2019;

255. Ibn-mohammed T, Randall CA, Mustapha KB, Guo J, Walker J, Berbano S. This is a repository copy of Decarbonising ceramic manufacturing : a techno-economic analysis of energy efficient sintering technologies in the functional materials sector . White Rose Research Online URL for this paper : Version : Published Version Artic. 2019;

256. Museau M, Paris H, Mokhtarian H, Coatane E, Ituarte IF. CIRP Annals - Manufacturing Technology Comparative environmental impacts of additive and subtractive manufacturing technologies. 2016;65:29–32.

257. Le VT. A life cycle assessment-based approach for evaluating the influence of total build height and batch size on the environmental performance of electron beam melting. 2018;275–88.

258. Faludi J, Bayley C, Bhogal S, Iribarne M. Comparing environmental impacts of additive manufacturing vs traditional machining via life-cycle assessment. 2015;1(October 2013):14–33.

259. Serres N, Tidu D, Sankare S, Hlawka F. Environmental comparison of MESO-CLAD Ò process and conventional machining implementing life cycle assessment. J Clean Prod [Internet]. 2011;19(9–10):1117–24. Available from: http://dx.doi.org/10.1016/j.jclepro.2010.12.010

260. Kreiger M, Pearce JM. Environmental Life Cycle Analysis of Distributed Three-Dimensional Printing and Conventional Manufacturing of Polymer Products. 2013;

261. Ingarao G, Priarone PC, Deng Y, Paraskevas D. Environmental modelling of aluminium based components manufacturing routes : Additive manufacturing versus machining versus forming. J Clean Prod [Internet]. 2018;176:261–75. Available from: https://doi.org/10.1016/j.jclepro.2017.12.115

262. Campatelli G, Montevecchi F, Venturini G, Ingarao G, Priarone PC. Integrated WAAM - Subtractive Versus Pure Subtractive Manufacturing Approaches : An Energy Efficiency Comparison. International Journal of Precision Engineering and Manufacturing-Green Technology [Internet]. 2020;7(1):1–11. Available from: https://doi.org/10.1007/s40684-019-00071-y

263. Ingarao G, Priarone PC. A comparative assessment of energy demand and life cycle costs for additive- and subtractive-based manufacturing approaches. J Manuf Process [Internet]. 2020;56(June):1219–29. Available from: https://doi.org/10.1016/j.jmapro.2020.06.009

264. Lyons R, Newell A, Ghadimi P, Papakostas N. Environmental impacts of conventional and additive manufacturing for the production of Ti-6Al-4V knee implant : a life cycle approach. 2021;787–801.

265. Gao F, Nie Z, Yang D, Sun B, Liu Y, Gong X, et al. Environmental impacts analysis of titanium sponge production using Kroll process in China. J Clean Prod [Internet]. 2018;174:771–9. Available from: https://doi.org/10.1016/j.jclepro.2017.09.240

266. Liu S, Shin YC. Additive manufacturing of Ti6Al4V alloy: A review. Mater Des. 2019 Feb 15;164.

267. Banerjee D, Williams JC. Perspectives on titanium science and technology. Acta Mater [Internet]. 2013;61(3):844–79. Available from: http://dx.doi.org/10.1016/j.actamat.2012.10.043

268. Burgers WG. CUBIC-BODY-CENTERED MODIFICATION INTO THE HEXAGONAL-CLOSE-PACKED MODIFICATION OF ZIRCONIUM mechanical point of view . 1933;

269. Chen Y, Kou H, Cheng L, Zhang Y, Yu Y, Lu Y, et al. Experimental Evidence of Precipitation of All 12 Variants in a Single β Grain in Titanium Alloys. 2018;2018.

270. Stanford N, Bate PS. Crystallographic variant selection in Ti-6Al-4V. Acta Mater. 2004;52(17):5215–24.

271. Shi R, Dixit V, Fraser HL, Wang Y. ScienceDirect Variant selection of grain boundary a by special prior b grain boundaries in titanium alloys. Acta Mater [Internet]. 2014;75:156–66. Available from: http://dx.doi.org/10.1016/j.actamat.2014.05.003

272. Gey N, Humbert M. Characterization of the variant selection occurring during the α → β → α phase transformations of a cold rolled titanium sheet. 2002;50:277–87.

273. Qiu D, Shi R, Zhang D, Lu W, Wang Y. ScienceDirect Variant selection by dislocations during a precipitation in a / b titanium alloys. 2015;88:218–31.

274. Wang SC, Aindow M, Starink MJ. Effect of self-accommodation on a / a boundary populations in pure titanium. 2003;c:2485–503.

275. Farabi E, Tari V, Hodgson PD, Rohrer GS, Beladi H. & C corrosion On the grain boundary network characteristics in a martensitic Ti – 6Al – 4V alloy. J Mater Sci [Internet]. 2020;55(31):15299–321. Available from: https://doi.org/10.1007/s10853-020-05075-7

276. Majumdar T, Bazin T, Ribeiro EMC, Frith JE, Birbilis N. Understanding the effects of PBF process parameter interplay on Ti-6Al-4V surface properties. Vol. 14, PLoS ONE. 2019.

277. Saxena VK, Radhakrishnan VM. Effect of phase morphology on fatigue crack growth behavior of α-β titanium alloy - A crack closure rationale. Metall Mater Trans A Phys Metall Mater Sci. 1998;29(1):245–61.

278. Sibisi PN, Popoola API, Arthur NKK, Pityana SL. Review on direct metal laser deposition manufacturing technology for the Ti-6Al-4V alloy. Vol. 107, International Journal of Advanced Manufacturing Technology. 2020. p. 1163–78.

279. Vrancken B, Thijs L, Kruth J pierre, Humbeeck J van. Heat treatment of Ti6Al4V produced by Selective Laser Melting : Microstructure and mechanical properties. J Alloys Compd [Internet]. 2012;541:177–85. Available from: http://dx.doi.org/10.1016/j.jallcom.2012.07.022

280. Squillace A, Prisco U, Ciliberto S, Astarita A. Effect of welding parameters on morphology and mechanical properties of Ti-6Al-4V laser beam welded butt joints. J Mater Process Technol. 2012;212(2):427–36.

281. Zhu YZ, Wang SZ, Li BL, Yin ZM, Wan Q, Liu P. Grain growth and microstructure evolution based mechanical property predicted by a modified Hall-Petch equation in hot worked Ni76Cr19AlTiCo alloy. Mater Des. 2014;55:456–62.

282. Rafi HK, Karthik N V., Gong H, Starr TL, Stucker BE. Microstructures and mechanical properties of Ti6Al4V parts fabricated by selective laser melting and electron beam melting. J Mater Eng Perform. 2013;22(12):3872–83.

283. Wang T, Zhu YY, Zhang SQ, Tang HB, Wang HM. Grain morphology evolution behavior of titanium alloy components during laser melting deposition additive manufacturing. J Alloys Compd [Internet]. 2015;632:505–13. Available from: http://dx.doi.org/10.1016/j.jallcom.2015.01.256

284. Carroll BE, Palmer TA, Beese AM. Anisotropic tensile behavior of Ti–6Al–4V components fabricated with directed energy deposition additive manufacturing. Acta Mater. 2015;87:309–20.

285. Blackmore ML, Zhang W, Todd I. The Origin of Microstructural Diversity , Texture , and Mechanical Properties in Electron Beam Melted Ti-6Al-4V. 2010;

286. Xu W, Brandt M, Sun S, Elambasseril J, Liu Q, Latham K, et al. ScienceDirect Additive manufacturing of strong and ductile Ti – 6Al – 4V by selective laser melting via in situ martensite decomposition. 2015;85:74–84.

287. Baufeld B, Brandl E, Van Der Biest O. Wire based additive layer manufacturing: Comparison of microstructure and mechanical properties of Ti-6Al-4V components fabricated by laser-beam deposition and shaped metal deposition. J Mater Process Technol. 2011;211(6):1146–58.

288. Formanoir C de, Michotte S, Rigo O, Germain L. Materials Science & Engineering A Electron beam melted Ti – 6Al – 4V : Microstructure , texture and mechanical behavior of the as-built and heat-treated material. Materials Science & Engineering A [Internet]. 2016;652:105–19. Available from: http://dx.doi.org/10.1016/j.msea.2015.11.052

289. Strantza M, Vafadari R, Baere D de, Vrancken B, Paepegem W van. Fatigue of Ti6Al4V Structural Health Monitoring. :1–15.

290. Costa L. Laser powder deposition. 2009;4(November 2008):264–79.

291. Chen J, Xue L. Experimental studies on process-induced morphological characteristics of macro- and microstructures in laser consolidated alloys. 2011;5859–75.

292. Salikhyanov D, Veselova V, Volkov V. Flow behavior and microstructure evolution of Ti-6Al-4V titanium alloy produced by selective laser melting compared to wrought. International Journal of Advanced Manufacturing Technology. 2022;119(1–2):953–67.

293. Bourell D, Wohlers T. Introduction to Additive Manufacturing. In: Additive Manufacturing Processes. ASM International; 2020. p. 1–8.

294. Facchini L, Magalini E, Robotti P, Molinari A, Höges S, Wissenbach K. Ductility of a Ti-6Al-4V alloy produced by selective laser melting of prealloyed powders. Rapid Prototyp J. 2010;16(6):450–9.

295. Liu S, Shin YC. Additive manufacturing of Ti6Al4V alloy: A review. Mater Des. 2019;164:107552.

296. Thijs L, Verhaeghe F, Craeghs T, Humbeeck J van, Kruth J pierre. A study of the microstructural evolution during selective laser melting of Ti − 6Al − 4V. Acta Mater [Internet]. 2010;58(9):3303–12. Available from: http://dx.doi.org/10.1016/j.actamat.2010.02.004

297. Baufeld B, Biest O van der, Gault R. Additive manufacturing of Ti − 6Al − 4V components by shaped metal deposition : Microstructure and mechanical properties. Mater Des [Internet]. 2010;31:S106–11. Available from: http://dx.doi.org/10.1016/j.matdes.2009.11.032

298. Kelly SM, Kampe SL. Microstructural Evolution in Laser-Deposited Multilayer Ti-6Al-4V Builds : Part I . Microstructural Characterization. 2004;35(June):1861–7.

299. Zhou Y, Qin G, Li L, Lu X, Jing R, Xing X. Materials Science & Engineering A Formability , microstructure and mechanical properties of Ti-6Al-4V deposited by wire and arc additive manufacturing with different deposition paths. Materials Science & Engineering A [Internet]. 2020;772(July 2019):138654. Available from: https://doi.org/10.1016/j.msea.2019.138654

300. Antonysamy AA, Meyer J, Prangnell PB. ScienceDirect Effect of build geometry on the β - grain structure and texture in additive manufacture of Ti \ 6Al \ 4V by selective electron beam melting. Mater Charact [Internet]. 2013;84:153–68. Available from: http://dx.doi.org/10.1016/j.matchar.2013.07.012

301. Reda R, Nofal A. Effect of Single and Duplex Stage Heat Treatment on the Microstructure and Mechanical Properties of Cast Ti − 6Al − 4V Alloy. 2013;388–93.

302. Fotovvati B, Namdari N, Dehghanghadikolaei A, Yang K, Ren Y, Finish DS, et al. Tensile properties and microstructural characterization of additive manufactured , investment cast and wrought Ti6Al4V alloy Tensile properties and microstructural characterization of additive manufactured , investment cast and wrought Ti6Al4V alloy. 2019;

303. Weston NS, Jackson M. FAST-forge – A new cost-effective hybrid processing route for consolidating titanium powder into near net shape forged components. J Mater Process Technol. 2017;243:335–46.

304. A KZŁ, Prahl U. Hot Processing of Powder Metallurgy and Wrought Ti-6Al-4V Alloy with Large Total Deformation : Physical Modeling and Verification by Rolling.

305. Kladovasilakis N, Charalampous P, Kostavelis I, Tzetzis D, Tzovaras D. Impact of metal additive manufacturing parameters on the powder bed fusion and direct energy deposition processes: a comprehensive review. Progress in Additive Manufacturing. 2021;

306. Liu P, Wang Z, Xiao Y, Horstemeyer MF, Cui X, Chen L. Insight into the mechanisms of columnar to equiaxed grain transition during metallic additive manufacturing. Addit Manuf. 2019;26:22–9.

307. Beese AM, Carroll BE. Review of Mechanical Properties of Ti-6Al-4V Made by Laser- Based Additive Manufacturing Using Powder Feedstock. 2016;68(3):724–34.

308. Shamsaei N, Yadollahi A, Bian L, Thompson SM. An overview of Direct Laser Deposition for additive manufacturing; Part II: Mechanical behavior, process parameter optimization and control. Addit Manuf. 2015;8:12–35.

309. Zuback JS, DebRoy T. The Hardness of Additively Manufactured Alloys. Vol. 11, Materials . 2018.

310. Nalla RK, Boyce BL, Campbell JP, Peters JO, Ritchie RO. Influence of Microstructure on High- Cycle Fatigue of Ti-6Al-4V : Bimodal vs . Lamellar Structures. 2002;33(March).

311. Arcella FG, Froes FH. Producing titanium aerospace components from powder using laser forming. JOM. 2000;52(5):28–30.

312. Mechanical Properties of Laser-Deposited Ti-6Al-4V P.A. Kobryn and S.L. Semiatin Air Force Research Laboratory, AFRL/MLLMP, Wright-Patterson Air Force Base, OH 45433-7817. :179–86.

313. Zhai Y, Galarraga H, Lados DA. Microstructure Evolution, Tensile Properties, and Fatigue Damage Mechanisms in Ti-6Al-4V Alloys Fabricated by Two Additive Manufacturing Techniques. Procedia Eng. 2015;114:658–66.

314. Bian L, Thompson SM, Shamsaei N. Mechanical Properties and Microstructural Features of Direct Laser-Deposited Ti-6Al-4V. JOM. 2015;67(3):629–38.

315. Prabhu AW, Vincent T, Chaudhary A, Zhang W, Babu SS. Effect of microstructure and defects on fatigue behaviour of directed energy deposited Ti–6Al–4V. Science and Technology of Welding and Joining. 2015 Nov 1;20(8):659–69.

316. Sandgren HR, Zhai Y, Lados DA, Shade PA, Schuren JC, Groeber MA, et al. Characterization of fatigue crack growth behavior in LENS fabricated Ti-6Al-4V using high-energy synchrotron x-ray microtomography. Addit Manuf. 2016;12:132–41.

317. Diegel O, Nordin A, Motte D. Additive Manufacturing Technologies. 2019;19–39.

318. Li C, Liu ZY, Fang XY, Guo YB. Residual Stress in Metal Additive Manufacturing. Procedia CIRP. 2018;71:348–53.

319. Almeida HA, Bártolo PJ. Topological Optimisation of Scaffolds for Tissue Engineering. Procedia Eng. 2013;59:298–306.

320. Adachi T, Osako Y, Tanaka M, Hojo M, Hollister SJ. Framework for optimal design of porous scaffold microstructure by computational simulation of bone regeneration. Biomaterials. 2006;27(21):3964–72.

321. Bauer S, Schmuki P, von der Mark K, Park J. Engineering biocompatible implant surfaces. Part I: Materials and surfaces. Prog Mater Sci. 2013;58(3).

322. Choy WJ, Mobbs RJ, Wilcox B, Phan S, Phan K, Sutterlin CE. Reconstruction of Thoracic Spine Using a Personalized 3D-Printed Vertebral Body in Adolescent with T9 Primary Bone Tumor. World Neurosurg. 2017;105:1032.e13-1032.e17.

323. Xu N, Wei F, Liu X, Jiang L, Cai H, Li Z, et al. Reconstruction of the Upper Cervical Spine Using a Personalized 3D-Printed Vertebral Body in an Adolescent With Ewing Sarcoma. Spine (Phila Pa 1976). 2016;41(1).

324. Wong KC, Kumta SM, Geel N V, Demol J. One-step reconstruction with a 3D-printed, biomechanically evaluated custom implant after complex pelvic tumor resection. Computer Aided Surgery. 2015 Jan 2;20(1):14–23.

325. Li H, Qu X, Mao Y, Dai K, Zhu Z. Custom Acetabular Cages Offer Stable Fixation and Improved Hip Scores for Revision THA With Severe Bone Defects. Clin Orthop Relat Res. 2016;474(3).

326. Yin Q, Liu W, Wang S. Application of customized augments fabricated by rapid prototyping for severe bone defects of the knee. Chin Med J (Engl). 2014;127(15):2870–1.

327.   Luo W, Huang L, Liu H, Qu W, Zhao X, Wang C, et al. Customized Knee Prosthesis in Treatment of Giant Cell Tumors of the Proximal Tibia: Application of 3-Dimensional Printing Technology in Surgical Design. Medical Science Monitor. 2017;23:1691–700.

328.   Kumar A, Mandal S, Barui S, Vasireddi R, Gbureck U, Gelinsky M, et al. Low temperature additive manufacturing of three dimensional scaffolds for bone-tissue engineering applications: Processing related challenges and property assessment. Materials Science and Engineering: R: Reports. 2016;103:1–39.

329.   DebRoy T, Mukherjee T, Milewski JO, Elmer JW, Ribic B, Blecher JJ, et al. Scientific, technological and economic issues in metal printing and their solutions. Nat Mater. 2019;18(10):1026–32.

330.   Schmidt J, Hackenbroch • M H. The Cenos hollow stem in total hip arthroplasty: first experiences in a prospective study. Vol. 113, Arch Orthop Trauma Surg. 1994.

331.   Gross S, Abel EW. A finite element analysis of hollow stemmed hip prostheses as a means of reducing stress shielding of the femur. Vol. 34, Journal of Biomechanics. 2001.

332.   Chatterjee S, Dey S, Majumder S, RoyChowdhury A, Datta S. Computational intelligence based design of implant for varying bone conditions. Int J Numer Method Biomed Eng. 2019;35(6):1–17.

333.   Yamako G, Chosa E, Zhao X, Totoribe K, Watanabe S, Sakamoto T, et al. Load-transfer analysis after insertion of cementless anatomical femoral stem using pre- and post-operative CT images based patient-specific finite element analysis. Med Eng Phys. 2014;36(6):694–700.

334.   Jonkers I, Sauwen N, Lenaerts G, Mulier M, Van der Perre G, Jaecques S. Relation between subject-specific hip joint loading, stress distribution in the proximal femur and bone mineral density changes after total hip replacement. J Biomech. 2008;41(16):3405–13.

335.   Ruben RB, Fernandes PR, Folgado J. On the optimal shape of hip implants. J Biomech. 2012;45(2):239–46.

336.   Chatterjee S, Dey S, Majumder S, RoyChowdhury A, Datta S. Computational intelligence based design of implant for varying bone conditions. Int J Numer Method Biomed Eng. 2019 Jun 1;35(6):e3191.

337.   Bitsakos C, Kerner J, Fisher I, Amis AA. The effect of muscle loading on the simulation of bone remodelling in the proximal femur. J Biomech. 2005;38(1):133–9.

338.	Anderson DE, Madigan ML. Effects of Age-Related Differences in Femoral Loading and Bone Mineral Density on Strains in the Proximal Femur During Controlled Walking. J Appl Biomech. 2013;29(5):505–16.

339.	Merdji A, Bachir Bouiadjra B, Achour T, Serier B, Ould Chikh B, Feng ZO. Stress analysis in dental prosthesis. Comput Mater Sci. 2010 Jun;49(1):126–33.

340.	Simonelli M, Tse YY, Tuck C. Effect of the build orientation on the mechanical properties and fracture modes of SLM Ti-6Al-4V. Materials Science and Engineering A. 2014 Oct 20;616:1–11.

341.	Yang J, Yu H, Wang Z, Zeng X. Effect of crystallographic orientation on mechanical anisotropy of selective laser melted Ti-6Al-4V alloy. Mater Charact. 2017 May 1;127:137–45.

342.	Zhao X, Li S, Zhang M, Liu Y, Sercombe TB, Wang S, et al. Comparison of the microstructures and mechanical properties of Ti-6Al-4V fabricated by selective laser melting and electron beam melting. Mater Des. 2016 Apr 5;95:21–31.

343.	Simonelli M, Tse YY, Tuck C. On the texture formation of selective laser melted Ti-6Al-4V. Metall Mater Trans A Phys Metall Mater Sci. 2014;45(6):2863–72.

344.	Monroy KP, Delgado J, Sereno L, Ciurana J, Hendrichs NJ. Effects of the Selective Laser Melting manufacturing process on the properties of CoCrMo single tracks. Metals and Materials International. 2014 Sep 1;20(5):873–84.

345.	Xu W, Brandt M, Sun S, Elambasseril J, Liu Q, Latham K, et al. Additive manufacturing of strong and ductile Ti-6Al-4V by selective laser melting via in situ martensite decomposition. Acta Mater. 2015 Feb 15;85:74–84.

346.	Galarraga H, Lados DA, Dehoff RR, Kirka MM, Nandwana P. Effects of the microstructure and porosity on properties of Ti-6Al-4V ELI alloy fabricated by electron beam melting (EBM). Addit Manuf. 2016 Apr 1;10:47–57.

347.	Aboulkhair NT, Everitt NM, Ashcroft I, Tuck C. Reducing porosity in AlSi10Mg parts processed by selective laser melting. Addit Manuf. 2014 Oct 1;1:77–86.

348.	Bauereiß A, Scharowsky T, Körner C. Defect generation and propagation mechanism during additive manufacturing by selective beam melting. J Mater Process Technol. 2014;214(11):2522–8.

349.	Pei X, Wang L, Zhou C, Wu L, Lei H, Fan S, et al. Ti6Al4V orthopedic implant with biomimetic heterogeneous structure via 3D printing for improving osteogenesis. Mater Des. 2022 Sep 1;221.

350.	Qiao B, Dong C, Tong S, Kong D, Ni X, Zhang H, et al. Anisotropy in α′ martensite and compression behavior of Ti6Al4V prepared by selective laser melting. Mater Res Express. 2019 Nov 22;6(12).

351.	Kok Y, Tan XP, Wang P, Nai MLS, Loh NH, Liu E, et al. Anisotropy and heterogeneity of microstructure and mechanical properties in metal additive manufacturing: A critical review. Mater Des. 2018 Feb 5;139:565–86.

352.	Qiu C, Ravi GA, Dance C, Ranson A, Dilworth S, Attallah MM. Fabrication of large Ti-6Al-4V structures by direct laser deposition. J Alloys Compd. 2015 Apr 25;629:351–61.

353.	Vilaro T, Colin C, Bartout JD. As-fabricated and heat-treated microstructures of the Ti-6Al-4V alloy processed by selective laser melting. Metall Mater Trans A Phys Metall Mater Sci. 2011 Oct;42(10):3190–9.

354.	Tseng JC, Huang WC, Chang W, Jeromin A, Keller TF, Shen J, et al. Deformations of Ti-6Al-4V additive-manufacturing-induced isotropic and anisotropic columnar structures: Insitu measurements and underlying mechanisms. Addit Manuf. 2020 Oct 1;35.

355.	Antonysamy AA, Meyer J, Prangnell PB. Effect of build geometry on the β-grain structure and texture in additive manufacture of Ti6Al4V by selective electron beam melting. Mater Charact. 2013;84:153–68.

356.	Simonelli M, Tse YY, Tuck C. On the texture formation of selective laser melted Ti-6Al-4V. Metall Mater Trans A Phys Metall Mater Sci. 2014;45(6):2863–72.

357.	Sridharan N, Chaudhary A, Nandwana P, Babu SS. Texture Evolution During Laser Direct Metal Deposition of Ti-6Al-4V. JOM. 2016 Mar 1;68(3):772–7.

358.	Antonysamy AA, Meyer J, Prangnell PB. Effect of build geometry on the β-grain structure and texture in additive manufacture of Ti6Al4V by selective electron beam melting. Mater Charact. 2013;84:153–68.

359.	Thijs L, Kempen K, Kruth JP, Van Humbeeck J. Fine-structured aluminium products with controllable texture by selective laser melting of pre-alloyed AlSi10Mg powder. Acta Mater. 2013 Mar;61(5):1809–19.

360.	Garibaldi M, Ashcroft I, Simonelli M, Hague R. Metallurgy of high-silicon steel parts produced using Selective Laser Melting. Acta Mater. 2016 May 15;110:207–16.

361.	Ahmed Obeidi M, Uí Mhurchadha SM, Raghavendra R, Conway A, Souto C, Tormey D, et al. Comparison of the porosity and mechanical performance of 316L stainless steel

manufactured on different laser powder bed fusion metal additive manufacturing machines. Journal of Materials Research and Technology. 2021 Jul 1;13:2361–74.

362. Brodie EG, Robinson KJ, Sigston E, Molotnikov A, Frith JE. Osteogenic Potential of Additively Manufactured TiTa Alloys. ACS Appl Bio Mater. 2021;4(1):1003–14.